

A Mobile Atom Interferometer for High-Precision Measurements of Local Gravity

D i s s e r t a t i o n

zur Erlangung des akademischen Grades

doctor rerum naturalium

(Dr. rer. nat.)

im Fach Physik

eingereicht an der

Mathematisch-Naturwissenschaftlichen Fakultät I

der Humboldt-Universität zu Berlin

von

Dipl.-Phys. Alexander Senger

Präsident der der Humboldt-Universität zu Berlin:

Prof. Dr. Jan-Hendrik Olbertz

Dekan der Mathematisch-Naturwissenschaftlichen Fakultät I:

Prof. Dr. Andreas Herrmann

Gutachter:

1. Prof. Achim Peters, Ph.D.

2. Prof. Dr. Oliver Benson

3. Prof. Dr. Markus Arndt

Tag der mündlichen Prüfung: 22.11.2011

für Sara, Ferdinand und Felix

Abstract

Precise measurements of Earth’s gravitational acceleration g are important for a range of fundamental problems—e. g. the Watt balance as an approach for a new definition of the kilogram—and a great tool to investigate geophysical phenomena reaching from the topmost layers of soil to the very core of our planet. Recently, research efforts have been made to develop dedicated quantum sensors capable of such measurements with very high precision and accuracy.

This thesis describes the design and implementation of such a sensor, aiming at a superior accuracy of 0.5 ppb, resolvable in measurements of 24 h. A feature distinguishing this device from previous work is its mobility, allowing for comparison with other state-of-the-art instruments, and for applications in field use in various locations.

Rubidium atoms are laser-cooled and launched on a free-fall trajectory. Exploiting the wave nature of quantum particles, coherent manipulation with light pulses is used to split, reflect and recombine the atoms’ wave-packets. The resulting matter-wave interferometer is highly susceptible to inertial forces and allows for sensitive measurements of accelerations.

Inertial sensing with a precision of $160 \text{ nm s}^{-2}/\sqrt{\text{Hz}}$ was demonstrated, resulting in a measurement of g with a statistical uncertainty of 0.8 nm s^{-2} in 15 h, surpassing a conventional state-of-the-art absolute gravimeter by a factor of eight. Comparison with the German gravity reference net revealed a discrepancy of 260 nm s^{-2} , well covered by the combined systematic uncertainties of 520 nm s^{-2} . Likely causes for this deviation are identified and suitable countermeasures are proposed.

Zusammenfassung

Eine Reihe fundamentaler Problemstellungen setzt die genaue Kenntnis der Erdbeschleunigung g voraus, z. B. die Neudefinition des Kilogramms im laufenden Watt-Waage-Projekt. Des Weiteren sind Gravitationsmessungen ein herausragendes Werkzeug der geophysikalischen Forschung, machen sie doch Phänomene vom oberen Erdreich bis hinab in den Erdkern zugänglich. Für Absolutmessungen geeignete Quanten-Sensoren mit höchster Präzision sind deshalb Gegenstand aktueller Entwicklungen.

Diese Arbeit beschreibt die Planung und Implementierung eines solchen Sensors, der für eine überlegene absolute Genauigkeit von fünf Teilen in 10^{10} , zu erreichen in Messungen von 24 h, ausgelegt ist. Ein Merkmal, das dieses Instrument vor früheren Entwicklungen auszeichnet, ist seine Mobilität, die Anwendungen im Feld sowie Vergleichsmessungen mit anderen Gravimetern ermöglicht.

Die quantenmechanische Wellennatur von (Rubidium-) Atomen wird genutzt, um durch kohärente Teilung, Reflexion und Wiedervereinigung der sie konstituierenden Wellenpakete mit Hilfe von Lichtpulsen ein Materiewelleninterferometer darzustellen. Auf ein Ensemble lasergekühlter Atome im freien Fall angewandt, kann deren Empfindlichkeit auf Inertialkräfte genutzt werden, um hochsensible Messungen der auftretenden Beschleunigungen zu erreichen.

Eine Messpräzision von $160 \text{ nm s}^{-2}/\sqrt{\text{Hz}}$ wird demonstriert, die ausreicht, um g in 15 h mit einer statistischen Ungewissheit von 0.8 nm s^{-2} zu bestimmen; dies ist um einen Faktor acht besser, als mit den besten klassischen Absolutgravimetern üblich. Ein Vergleich mit dem Deutschen Schweregrundnetz ergibt eine Abweichung von 260 nm s^{-2} bei einer Ungewissheit von 520 nm s^{-2} in den systematischen Einflüssen. Deren wahrscheinliche Ursachen sowie geeignete Gegenmaßnahmen werden identifiziert.

Contents

1. Introduction	1
1.1. Gravimetry	8
2. Theory	13
2.1. Atom Interferometer in Gravity	13
2.2. Gravity Variations	29
3. Experiment	33
3.1. Preparing the Atoms	33
3.2. Interferometer Sequence	42
3.3. Detection	56
3.4. Vibration Isolation	57
3.5. Fountain Set-up and Mobility	66
3.6. Gravity of Fountain Set-up	70
3.7. Laser	78
3.8. Frequency Reference, Timing and Control	82
4. Results	91
4.1. Noise	91
4.2. Gravity measurement	98
5. Conclusion and Outlook	107
A. Details of Long-Term Gravity Measurement	111
B. Aluminium Knife-Edge Seal	115

1. Introduction

Most measurements get better with a growing number of samples as statistics improve. The common way to reap this benefit is simply to repeat the same measurement over and over again, paying with measurement time for increased precision. Principal limits arise here from time varying quantities and from systematic drifts in the sensor. Often, the simple fact that the (life-)time of the observer is limited prohibits further development along this line.

Another way would be to use a large set of identical sensors working in parallel. However, this approach has rarely been used in metrology, as it is prohibitively expensive for most kinds of precision tools, and yields only questionable results in case of cheap working material, which often suffers from uncontrollable drift and bias. Also, with a growing set of technical equipment, entropy becomes a major concern, as it gets increasingly difficult to keep everything in good working order and to obtain reliable results.

With the rapid development of matter wave optics in the past two decades, there is a new aspect to the situation. A "new" class of extremely inexpensive, ultra-stable, highly reliable and controllable sensing devices becomes accessible, which are available essentially without limit: cold neutral atoms. For most practical purposes they pose well understood quantum systems with their properties given by the very nature of our universe. In principle this enables measurements which are inherently bound to physical constants, thus defying the need for regular calibrations¹.

In addition, there exist a large number of different elements with a wide range of properties—and thus sensitivities to various external fields—to choose from; the electric polarizability spanning two orders of magnitude might serve as an example. As it has become possible to address and interrogate atoms with high selectivity, the full potential of quantum sensors is beginning to unfold. And one of the many benefits is the possibility to

¹It will be seen later for the instrument described here, that the measured gravity values are given in terms of an atomic property—a wave-vector which is related to energy differences in electronic states—and a time span. As a frequency standard could also be derived from the atoms, a fully self-contained measurement is possible.

1. Introduction

prepare large samples and to query them simultaneously with negligible cross talk, which often allows to scale sensitivity with at least the square root of the number of atoms involved.

While atoms themselves have been at hand for quite some time, it is the pronounced progress in the methods necessary to prepare well defined samples and to read out the effects of tiny disturbances which fuelled the rapid development of quantum sensing applications. Namely the manipulation of neutral atoms with light and the principle of matter wave interference are the basis for a wide range of instruments—including the one described here.

Large scattering cross sections and the possibility to control the electronic state makes light an ideal tool to handle atoms. Moreover, light fields can be altered rapidly and shaped with micrometer accuracy (e.g. in the form of light gratings), allowing for precise control in time and in space. Therefore it was largely the progress in laser control² which enabled recent developments in the field of atom optics.

With the advent of spectroscopically stabilised lasers it became feasible to very specifically address atomic resonances, while at the same time being able to provide enough intensity to induce sizeable effects. This led to a proposal by Hänsch and Schalow [1] to cool a low-density gas by illuminating it with intense, quasi-monochromatic light tuned to the red side of a closed cycling transition between two electronic states. Photons scattered by a moving atom Doppler-shifted into resonance will carry away a fraction of its kinetic energy and thus reduce its motion. Residual velocities in the range of millimetres per second are easily achievable in a few milliseconds, equivalent to temperatures of only some micro-kelvin. With this scheme—an *optical molasses*—first samples of laser cooled atoms were demonstrated in 1985 [2]. A substantial improvement was achieved by adding a 3D magnetic flux gradient with vanishing flux at the point in space where the cooling beams intersect. The spatial variations in Zeeman shifts, together with appropriate polarization of the laser beams, lead to net light forces directed to the point of zero flux. This way the atoms are confined in space in a so called *magneto-optical trap* (MOT) [3].

Typically 10^9 neutral atoms are accumulated in the volume of a pea and can then be put on chosen trajectories, e.g. in a fountain geometry. Accelerated upwards to a few m/s, interaction times of up to a second are

²An important class of matterwave interferometer is based on mechanical gratings with typical spacings in the range of micro- to nano-meter. The ability to prepare them in suitable qualities was developed in the same decades as for the light gratings. Often both techniques are employed in parallel.

well in reach while keeping the dimensions of the experimental apparatus within reasonable limits. This is easy enough to apply either well defined light pulses to drive intra-atomic resonances or off-resonant light patterns acting as phase gratings. Both techniques allow for coherent manipulation of the wave-like nature of the atom.

This leads to the extraordinary notion of matter waves laid down by Louis-Victor de Broglie in his dissertation in 1924 [4]. De Broglie proposed that there is no such thing as particles, well localized pieces of matter, but that all matter also needs to be regarded as waves, reaching into surrounding space, with characteristics dependent on the properties of mass and velocity. This perception was the inspiration for Schrödinger’s work and thus builds one of the corner stones of quantum mechanics. It also brings up naturally the idea of diffraction and interference and leads to the concept of matter wave optics, where the propagation and (self-) interaction of particles, e. g. atoms, can be described similarly to that of light beams.

While this started as a purely theoretical construct, soon after experimental evidence of matter waves was found. First by Davisson and Germer [5] and G. P. Thomson—who saw Bragg scattering of electrons in crystals—and later by Rupp [6]—who observed diffraction of electrons with man-made gratings. These experiments proved the validity of de Broglie’s ideas and contributed to his Nobel prize in 1929. Ever since the objects subjected to diffraction have grown heavier and more complex: neutrons [7], atoms [8], simple [9, 10] and complex [11, 12] molecules with no principal obstacles hit so far.

Apart from fundamental aspects, coherent manipulation of matter waves has also proven to be a versatile tool in precision measurements. Neutron diffraction has evolved to a widely used technique in material and biochemical science, and diffraction patterns in transmission electron microscopy are used to study ordering of structures on molecular and atomic scales.

The concept of interference was soon explored, too. First demonstrated with electrons [13] and neutrons [14], wide adoption of this technique was hindered by the involved set-ups necessary. The field of matter wave optics lacked a readily available constituent to form the analogue of light beams, and the appropriate tools to control them. It was in the rapidly developing fields of cooling and manipulating neutral atoms—often with light, as mentioned above—where these shortcomings could be lifted. With adequate techniques appearing in the 1980s, the first atom interferometers were presented 1991 [15–18]. Since then atom interferometers have spawned

1. Introduction

a broad range of scientific activity, a detailed overview of which can be found in [19].

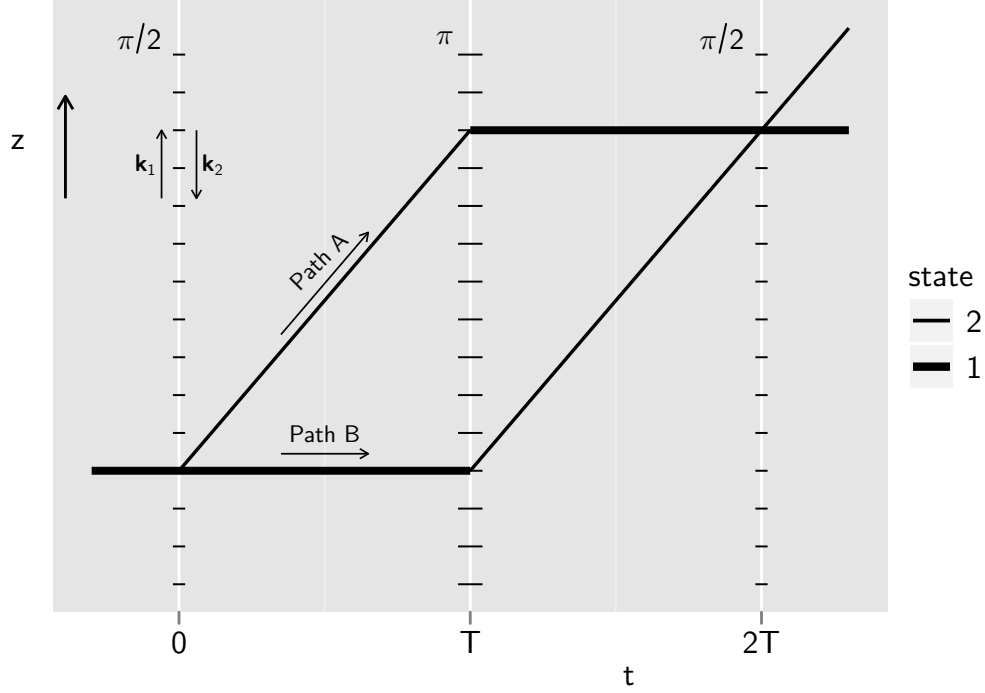


Figure 1.1.: Mach-Zehnder type interferometer with three light pulses. The matter wave is split, reflected and recombined using counterpropagating pairs of lasers with wave vectors \mathbf{k}_1 and \mathbf{k}_2 at times $0, T$ and $2T$. The atom's internal state is switched between $|1\rangle$ and $|2\rangle$ accordingly.

Consequently a complete interferometer can be realised with only light to control the matter wave. An intuitive example is the Mach-Zehnder-like geometry used in this experiment, realised by three light pulses. After preparation in a MOT, the cold cloud of atoms is launched on a parabolic trajectory using light forces. A first resonant light pulse chosen to switch the electronic state of an atom with a probability of $1/2$ will lead to a *splitting* of the corresponding wave packet: after the pulse, the atom will be in a coherent superposition of two internal states which differ in phase and frequency of the complementing matter wave. As the excited state carries additional momentum from the photons, this is associated with a bifurcation of the trajectory, leading to a possibly substantial spatial separation³

³In the experiment here up to 3 mm compared to the typical dimensions of atoms of < 1 nm.

of the two parts of the wave packet. From there on evolution of the distinct parts will lead to a growing phase shift between them, potentially further enhanced by the effect of additional fields due to the different susceptibility of the atoms states.

To reject the effect of time propagation and to merge the trajectories, a second light pulse is applied at time T , shaped to switch the states with unit probability and to swap the momentum associated with the paths. This way, after $2T$ temporal effects in the now overlapping wave packets will cancel, leaving only those contributions caused by external fields and the interaction with light pulses.

At this point in time a third light pulse—again with a switching probability of $1/2$ —splits each part of the wave packet into the two distinct outputs of the pulse sequence. The atomic state is then the same in each individual output, but differs between the two. The resulting interference translates the unobservable accumulated phase shift into an amplitude modulation measurable as the ratio of the atoms in the two outputs/states. Consequently the sequence allows measurement of the difference in effects of fields acting on the atoms, dependent on their electronic state and trajectory. This makes atom interferometry a highly versatile measuring tool sensitive to a range of phenomena not equally tractable by light interferometers.

Albeit instruments with suitable geometries to implement multi-path interference were used to perform optical Ramsey spectroscopy on ultrasonic jets of metastable Helium in the late 1980s, it was realised only later by Bordé, that the same set-up could be regarded as an atom interferometer and could be used to measure inertial forces [20]. The first dedicated experiments demonstrating matter wave interference with light gratings were presented two years after this discovery and already measured acceleration [15] and rotation [16] respectively.

Since then, atom interferometry has proven to be valuable in various fields like fundamental physics, metrology, applied physics or geophysics. It has been widely used for principal studies e.g. investigating decoherence [21, 22], Aharonov-Bohm and Aharonov-Casher effects [23] or Berry phase [24]. With every atom acting as an independent probe, these instruments are also versatile tools capable of high precision measurements—especially at microscopic scales. This enabled measurements of atomic properties like polarizability [25], Stark shift [26, 27] and van-der-Waals and Casimir-Polder interaction [28, 29] to unprecedented resolution. Another remarkable result is the determination of the fine structure constant with a fractional uncertainty of 7×10^{-9} by measuring \hbar/m_{atom} [30, 31]—

1. Introduction

almost the precision offered by the best alternative method based on measuring the electron g-factor. A comparison of these vastly different methods allows for checks of the underlying physics across distinct subfields with extraordinary accuracy; and substantial improvements are foreseen for the near future.

Another area where atom interferometry is expected to play an important role is in tests of relativity. A first demonstrator to verify the weak equivalence principle was presented in 2004 [32], measuring the differential acceleration of two isotopes of Rubidium. In the same experiment a hypothetical dependence on the electronic state of the atoms was also probed, which is hardly possible when relying on macroscopic test bodies. This line can be extended even further as sufficient quantities of antimatter are becoming available⁴, enabling gravitational tests on matter with very distinct quantum properties. Other proposals for equivalence tests with ordinary atoms [35] suggest highly competitive sensitivities in the order of 10^{-15} and better. Future satellite based interferometers could also measure the gravitomagnetic and the Lense-Thirring-effect [36] or even detect gravitational waves [37].

Recently, it was claimed that atom interferometers of the type presented here could also serve as a highly sensitive test for the gravitational redshift. Re-evaluating the results of [38] former bounds of absolute measurements could be improved by four orders of magnitude reaching a level below 10^{-8} [39]. These results put experiments with atom interferometers among the most stringent laboratory tests of general relativity to date.

As massive particles are much more sensitive to inertial forces than photons, applications to measure rotation, acceleration and gravitational effects were amongst the first developed in the emerging field of matter wave interferometry. As demonstrated with neutrons [42], they have been refined with the aid of neutral atoms to a level where they compare favourably to any other technique.

Today, gyroscopes based on atom interferometry feature a precision of 6×10^{-10} (rad/s)/ $\sqrt{\text{Hz}}$ [43] and gravity gradiometers utilizing two interferometers 1.4 m apart can reach 4×10^{-9} s⁻²/ $\sqrt{\text{Hz}}$ [44]. With both techniques available in transportable packages, interesting applications like unaided inertial navigation become available [45]. Furthermore, gradiome-

⁴A classical Moiré deflectometer with a limited precision of 1 % is proposed as a first experiment [33]. As interferometry with Hydrogen has already been demonstrated [34], according steps towards a similar experiment with antihydrogen seem natural.

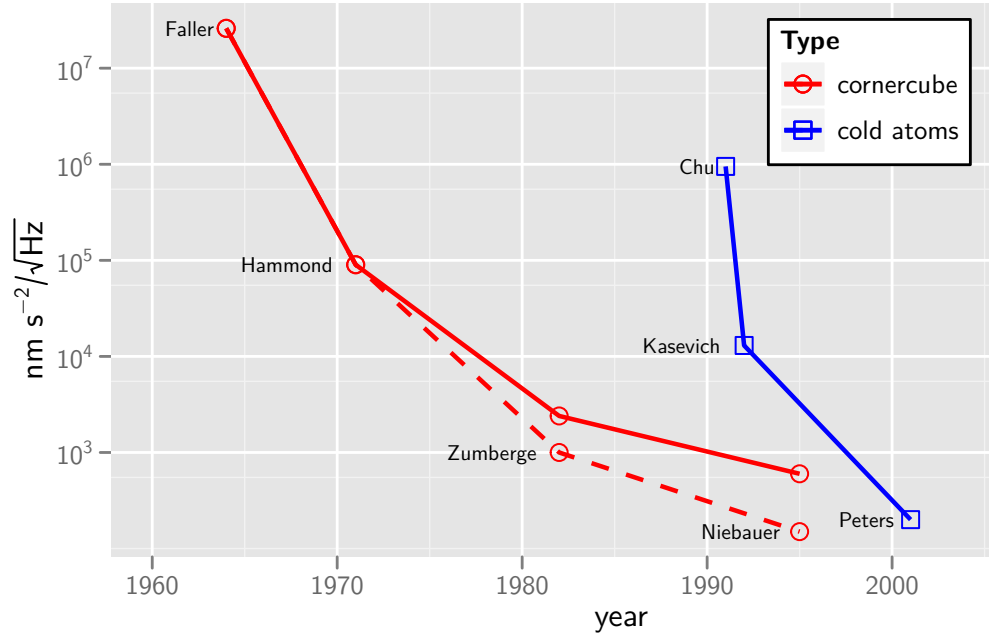


Figure 1.2.: Development of precision obtainable in one second for two types of absolute gravimeters. For state-of-the-art corner-cube instruments the dashed line represents claimed precision under ideal circumstances (quiet site, maximum drop rate), while the solid line shows performance under more conditions, similar to those the cold atoms instruments were subject of.

ters together with well characterized test masses can be used to determine G , the gravitational constant. Recent experiments yield fractional uncertainties of 10^{-3} [46, 47] with the perspective to push these limits below the level of 10^{-4} . Atom interferometer will then contribute to a better knowledge of this least precisely known fundamental constant, where up-to-date measurements disagree by several standard deviations and to which a comparison with alternative methods would therefore be highly favourable.

Absolute gravimeters utilizing cold atoms might be the closest to commercial application. They have been amongst the earliest experiments with atom interferometers and have been refined in a decade to a level where they show competitive performance compared to state-of-the-art instruments based on classical methods [48]. It is in this field that neutral atoms as highly sensitive probes might first prove their advantages over more traditional approaches, even in field measurements, where reliability and ruggedness are equally important to precision and accuracy.

1.1. Gravimetry

The precise knowledge of local acceleration due to gravity—commonly referred to as g —has many virtues. It is a prerequisite for a range of metrological applications where some quantity is related to a force, as e.g. in the definition of the unit of pressure or electrical current, because the force standard is mostly realized as gravitational pull of Earth on a known mass [49]. The Watt balance as an approach to a new definition of the kilogram—a long standing goal in the field of metrology—is a prominent example which relies heavily on an accurate measurement of local gravity [50].

Other applications arise naturally in the fields of geology and geophysics. Spatial mapping of gravitational variations is besides reflection seismology the only practical means of gathering large-volume density maps (and often much less costly) and thus a standard technique of geological survey. Typical scales vary from hundreds of square kilometres e.g. in resource exploration, up to global coverage from geostationary orbit⁵ in Earth observation [52]. Other applications monitor long-term variations in g as in investigations of the still ongoing post-glacial rebound [53] of tectonic plates or volcano surveillance where fluctuations in the subsurface magma systems cause alteration of local gravity [54].

These measurements are often done with relative gravimeters, which offer a lot of virtues. The most compact and affordable—and also the easiest to use—are instruments of the LaCoste-Romberg-type, which measure the elastic response of a spring due to variations in the acceleration of a suspended test-mass [55]. Their main purpose is comparison of gravity over short distances and time-scales (tens of kilometres and hours), where with modern devices the task of measuring is literally reduced to pushing a button. For longer periods or travels over greater distances their limited resolution and high drifts are forbidding, as well as their susceptibility to harsh conditions, which will introduce random shifts and variations in the scale factor. Thus frequent calibration against known gravity differences is necessary to obtain useful results.

The imperfections of mechanical springs are sought to be overcome by use of a "perfect" spring system based on currents running in a nearly-Helmholtz pair of superconducting coils. The generated magnetic flux is

⁵Here it is the uni-axial gravity gradient or possibly the full tensor, which is to be measured. Proposed atom interferometers for this purpose share nonetheless many of the design principals with the instrument described in this thesis.

theoretically perfectly stable⁶ and can be used to levitate a superconducting sphere in a field with a small gradient. By adjusting the current ratio in the coils to lower the gradient, the tendency of the sphere to return to an equilibrium position can be made arbitrarily small—equivalent to an ever-longer spring—and thus highly sensitive to small accelerations [51]. These systems have proven to feature superior noise characteristics over a wide range of frequencies and are able to take data continuously, thus avoiding aliasing found in pulsed measurements. However, due to a range of effects which are only partly understood, observed drifts are in the range of 100 nm s^{-2} per year, with little consistency between different instruments. Another problem are sudden jumps in measured g of up to 100 nm s^{-2} . These occur at random times and are far too fast to be connected to mass fluctuations.

Despite these problems superconducting gravimeters are state-of-the-art for precision surveys of gravity changes and are often the tool of choice in fundamental geophysical research. As such instruments suffer from substantial drift and ageing and lose all accuracy when transported or shocked, absolute gravimeters are mandatory for comparison over large distances or long time-scales. In this sense the unrivalled precision of relative instruments is complementary to the accuracy only offered by absolute instruments. Both types are essential for modern gravimetric metrology.

The de-facto standard for the purpose of absolute measurements are instruments which rely on massive bodies falling freely in an evacuated chamber, first developed in the 1960s [56]. The test masses are mostly hollow corner cube retroreflectors terminating one arm of a Michelson interferometer, where the acceleration of the retroreflector with respect to a resting counterpart can be deduced from the swept fringe signal. This principle has been refined over some 30 years, and state-of-the-art instruments [57] are commercially available, namely the FG5 from Micro-g Lacoste. This type of gravimeter has a specified precision⁷ of $150 \text{ nm s}^{-2}/\sqrt{\text{Hz}}$ and accuracy of 20 nm s^{-2} , while results of a recent international comparison of absolute gravimeters indicate a slightly higher spread among such instruments in field use [58].

In figure 1.2 it can be seen that the progress towards better precision slowed down considerably during the past 30 years for this type of gravime-

⁶as long as temperature and magnetic flux are kept within certain limits

⁷Said company specifies the precision as $15 \mu\text{Gal}/\sqrt{\text{Hz}}$, using the traditional unit of gravimetry ($1\text{Gal} := 1\text{cm/s}^2$). Throughout this thesis SI units are preferred.

1. Introduction

ter. A major cause is the macroscopic dimensions of the drop mass, which turn out to be cumbersome at very high levels of accuracy. When the retroreflector is released, the supporting floor and instrument show elastic recoil. This leads to tilt and parasitic accelerations, which as a matter of principle can not be distinguished from gravity. Furthermore, due to small torques imparted by the release process, the retroreflector will inevitably rotate slowly when falling, which produces phase shifts of the reflected beam if the optical centre is not identical to its centre of mass [57]. The latter can be shifted to the former with high precision, but unavoidable wear on the drop mass will degrade the performance over time, making regular maintenance necessary. This is why it is good practice with the FG5 to cut down the rate and number of drops to prolong maintenance intervals, while limiting the achievable precision.

The measurement principle with instruments such as the one described here is slightly different. The idea is to very precisely pinpoint the difference in falling distance, not of one, but of many test bodies between three points on a ballistic trajectory. The neutral atoms employed as drop masses offer a special benefit in this scheme. Their position at certain points in time—encoded as the phase of a standing laser wave—can be written into the phase of their quantum wave function during the optical transitions necessary to form the matter wave interferometer. With the outcome of the interferometer dependent on the phase difference between its two paths, each atom acts thus as a separate gravity probe unencumbered by drifts, ageing or wear. Together with the negligible effect of releasing only a cloud of neutral atoms⁸ this avoids all of the problems noted above. The low noise characteristics surpassing those of corner cube instruments by almost an order of magnitude (compare figure 1.3) allow for a far better visibility of the remaining systematics, facilitating their characterisation and ultimately their control.

The rapid evolution of atom gravimeters depicted in figure 1.2 gives reason to expect that this technique will contribute substantially to improvements in the field of geodetic metrology in the near future. It is hoped that all major systematic effects encountered so far can be understood, and eventually controlled, which will enable inertial measurements with superior accuracy backed by the fundamental nature of the quantum sensors exploited in these systems. This is underlined by the fact that the gravimeter developed for the Watt balance project at the Bureau National de Metrologie (BNM), Paris, is based on cold atom interferome-

⁸approximately 10^{-13} g

try [59].

As can be seen in figure 1.3, g is subject to a range of influences hardly controllable in all but some very quiet places—e.g. caves in dry, remote areas—making it impossible to fully characterize a dedicated sensor without comparing it against other state-of-the-art instruments. It is therefore highly desirable to have a set of moveable atom interferometers which would allow to participate in the international comparisons of absolute gravimeters organised by the Bureau International des Poids et Mesures on a regular basis⁹.

The aim of the ongoing development is therefore to design and implement an atom interferometer capable of absolute gravimetry with a competitive accuracy of 5 nm s^{-2} . As gravimetric measurements are typically performed overnight to limit the influence of environmental noise due to traffic and other human activities, it is desirable to achieve an even better precision on similar time scales. Furthermore, the set-up needs to be fully mobile and capable of rapid deployment in various locations in order to allow for direct comparison with other gravimeters and to demonstrate the outstanding potential of quantum sensing in field applications.

1.1.1. Organization of This Thesis

In chapter two the theory to describe an atom- gravimeter with suitable precision is summarized, and a short overview of gravitational variations modelling is given. A following chapter presents the experimental apparatus and gives some details of the measurement process. The observed noise is discussed in chapter four along with a first long-term measurement, which is compared to a determination of local gravity by a FG5 at the same site. Finally a quick outlook on future developments follows a summary of the obtained results.

⁹Another reason is of course, that laboratories for atom physics are rarely amongst the places where accurate knowledge of g is most valuable.

1. Introduction

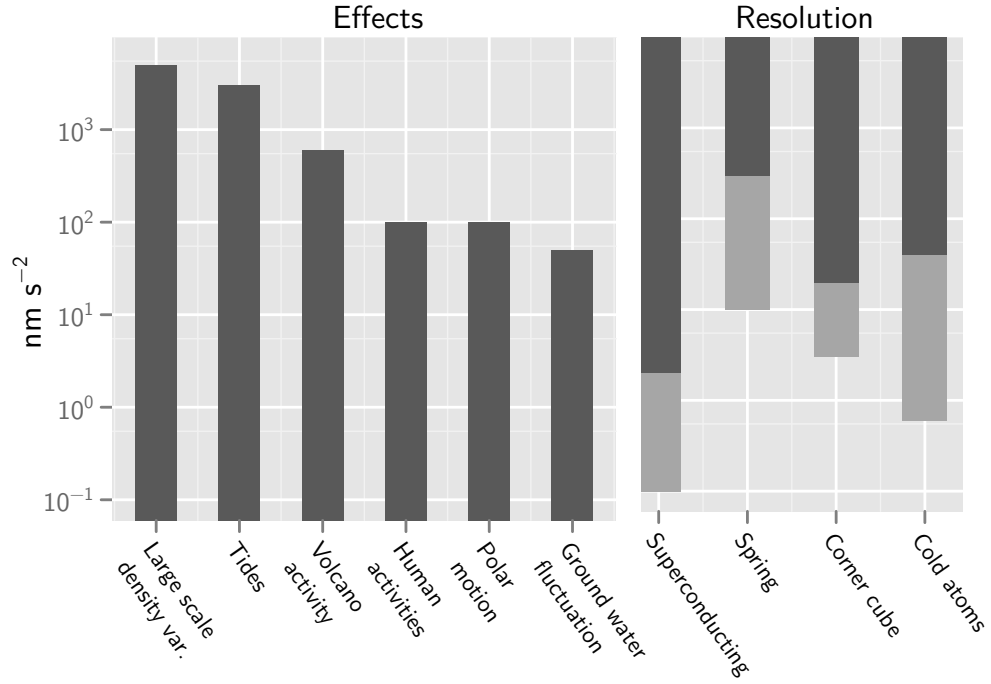


Figure 1.3.: (left) Typical magnitude of some gravitational effects. Large scale density variations are what is searched for in natural resource exploration, e.g. caused by oil fields. Human activities relate to mass changes in the near surrounding, like parking cars. Ground water fluctuations are a severe problem of accurate gravimetry, as the resulting changes are almost impossible to model. (right) Resolution obtainable with modern instruments: for relative gravimeters based on superconductivity and mechanical springs, the resolution obtainable in one minute (light grey) is given, where random fluctuations in one day (dark grey) have a highly adverse effect (For superconducting devices, this number was drawn from a comparison of two instruments at the same site found in [51]). Please note, that noise characteristics as shown for superconducting gravimeters need settling times ranging from days to weeks after initial set-up. The performance of absolute gravimeters (falling corner cube and cold atoms) is stated for the attainable resolution after 24 h at noisy sites (light grey), as well as the accuracy achieved so far (dark grey). For atom interferometer the accuracy is taken from [48], where the resolution is from this work.

2. Theory

The theoretical description of atom interferometers has been the subject of intense studies over the past 20 years, and can be considered mature in many aspects. Particularly the light-driven beamsplitter process used here [60–63] as well as appropriate interferometer geometries [64–67] are discussed in great detail elsewhere. Therefore this chapter confines to summarize the most important aspects, starting from very basic principles and adding refinements where necessary to reach the desired precision. A second part will bring a phenomenological overview of the prediction of gravitational fluctuations—most importantly tidal effects—as these have to be corrected for in the evaluation of experimental results.

2.1. Atom Interferometer in Gravity

To model the phase difference is common to split the interferometer phase into a part originating from free evolution and another due to interaction with the laser beams

$$\Delta\phi = \Delta\phi_{\text{free}} + \Delta\phi_{\text{light}}. \quad (2.1)$$

This approach is valid if the beamsplitters formed by the laser pulses can be considered thin, that is, their influence on the atoms is limited to an imprinted phase-factor and a change in the atom’s momentum at a specific point in time. The interferometer sequence is then cut into slices of wave-packet propagation only affected by background fields where in between the laser pulses are applied. The initial conditions for each piece of the path are given by the evolution along the preceding piece adjusted by the momentum transferred by the light pulse.

For a Mach-Zehnder geometry in a uniform gravitational field, the interferometer takes the form depicted in figure 2.1. The formerly straight paths are curved due to the constant acceleration in correspondence to classical trajectories of point-like masses¹. When no other external fields

¹It is not a priori clear why the notion of a trajectory is appropriate for a system

2. Theory

are present, the situation between light pulses is not distinguishable from the one depicted in figure 1.1 for an observer falling freely with the atom². According to the equivalence principle the phase difference from free evolution of atoms falling in a uniform gravitational field is thus the same as for zero gravity, where $\Delta\phi_{\text{free}}$ vanishes due to the inherent symmetry of the situation. Obviously the same holds for $\Delta\phi_{\text{light}}$ if the optics for the laser beams would be too in free fall. It is therefore the effect of lasers fixed in a frame not influenced by the acceleration to be assessed, which enables inertial measurements.

This can be achieved by reflecting the pair of laser beams driving the atomic transition from a mirror in rest to e. g. the centre of mass of Earth³. The phase of the light wave at any point is then given by

$$\phi_{\text{laser}}(z, t) = \mathbf{k}_{\text{eff}} \cdot \mathbf{z} - \omega_{\text{eff}} t \quad (2.2)$$

where z is the height above the mirror, \mathbf{k}_{eff} an assigned effective wave-vector and ω_{eff} an effective frequency. In the simplified picture the light phase dependent on the position of the interaction is added to the wave-packets phase when the atomic state is switched during optical transitions. With the sign given by the initial state, a summation over the contributions along the paths curved by the constant acceleration \mathbf{g} anti-parallel to \mathbf{z} yields

$$\begin{aligned} \Delta\phi &= (\phi_1^{\text{A}} - \phi_2^{\text{A}}) - (\phi_1^{\text{B}} - \phi_2^{\text{B}}) \\ &= (k_{\text{eff}}(v_{\text{rec}} T - \tfrac{1}{2} g T^2) + \omega_{\text{eff}} T) - (k_{\text{eff}}(v_{\text{rec}} T - \tfrac{3}{2} g T^2) + \omega_{\text{eff}} T) \\ &= k_{\text{eff}} g T^2 \end{aligned} \quad (2.3)$$

with the ϕ_i^α chosen as in figure 2.1 and v_{rec} the velocity due to photon recoil. From this equation it is evident that long T are favourable, which are extended to 230 ms in this experiment by choosing a fountain geometry. With $k_{\text{eff}} \approx 1.6 \times 10^7$ this gives rise to phase shifts of about 8.6×10^6 rad. Given the ability to read out the phase with a precision of a few hundred millirad a fractional single-shot precision of 10^{-8} in g becomes feasible.

which draws heavily from the quantum mechanical properties of its constituents. A justification arises from a path integral treatment, which will be discussed later.

²This is only true if the effect of the laser on any observable—e. g. the amount of transferred momentum—does not depend on the gravitational acceleration. For interferometer as the one discussed here, this condition is fulfilled. However, it is not in the case of neutron interferometers where the atoms are reflected from crystal surfaces [42], compare [68, p. 325].

³A technically feasible approximation for this scheme is presented in section 3.4.

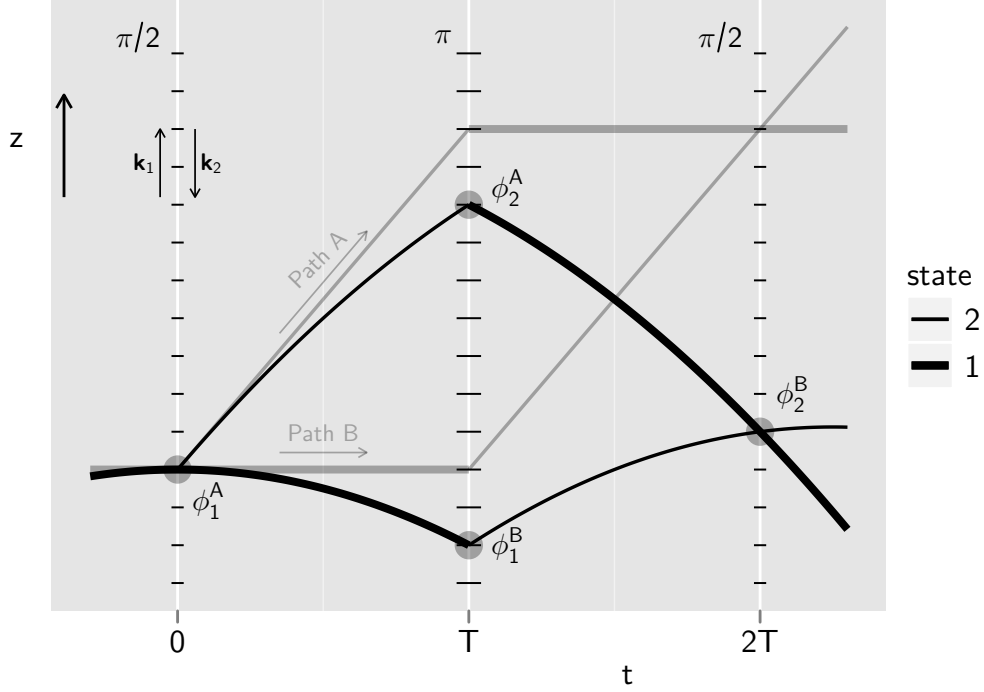


Figure 2.1.: Under influence of a constant acceleration anti-parallel to z , the paths along which the wave-packets of the atom develop are curved. This leads to changes in the position of the atoms at times of the laser pulses and thus to altered light phases imprinted into the wavepackets.

While this simple picture describes an atom gravimeter astonishingly well, it is not sufficient for the accuracy needed. Some refinements have to be made regarding the subtleties of light-matter interaction and non-uniform inertial fields.

2.1.1. Beamsplitter

The very different nature of the free propagation of wave-packets between light pulses and the interaction with the beamsplitters makes it difficult to calculate an atom interferometer within a single framework. It is therefore common to treat them separately, as noted above.

Beamsplitters and mirrors used here consist of two-photon Raman transitions stimulated by short pulses of counter-propagating lasers, a method developed by Chu and Kasevich for one of the first atom interferome-

2. Theory

ters [15]. While it is possible to incorporate further light pulses into the sequence [69] or to switch to many-photon transitions (e.g. Bragg diffraction) to increase the momentum transferred to the atoms and thus the response factor of the gravimeter, the inherent symmetry of this simple scheme facilitates control of systematic effects.

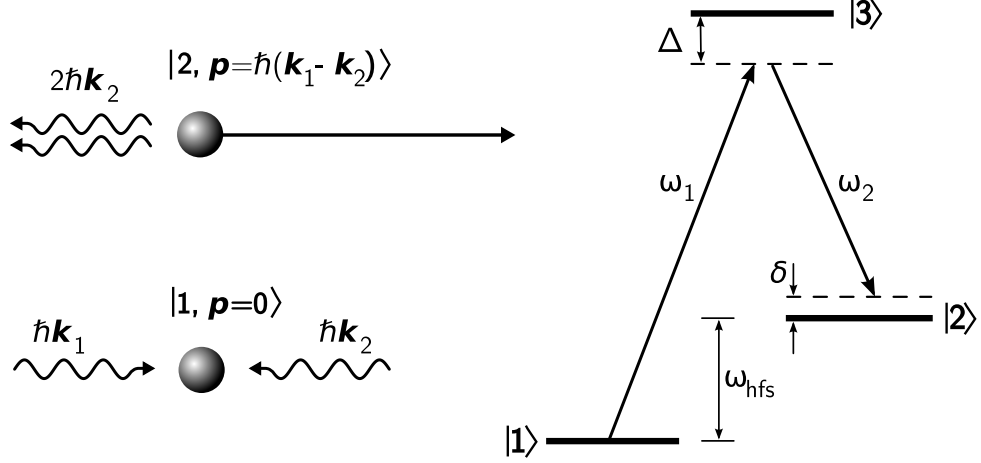


Figure 2.2.: Momentum and energy diagram for a stimulated Raman transition. In a two-photon process both internal and external state of an atom are simultaneously altered, which establishes a one-to-one correspondence between them.

The two laser beams are tuned close to optical transitions from two hyperfine levels $|1\rangle$ and $|2\rangle$ to an upper level $|3\rangle$ as depicted in figure 2.2. A detuning Δ —small compared to the hyperfine-splitting but large with respect to the Rabi frequencies of the optical transitions involved—ensures that spontaneous decay from $|3\rangle$ can be neglected. When interacting with the laser beams, the atom oscillates between $|1, p\rangle$ and $|2, p + \hbar\mathbf{k}_{\text{eff}}\rangle$ by absorbing a photon from one beam and emitting another into the second beam in a coherent process. This reduces the 3-level-system to an effective 2-level-system.

By setting the duration of the laser pulse to a fraction of $\pi/2$ of the cycle, the atom's wave-packet can be put into an equally distributed superposition of these states with its parts carrying different momenta and thus their centres of mass developing along distinct paths in close resemblance to an optical beamsplitter. Accordingly a π -pulse acts like a mirror and swaps both internal state and momentum. The net momentum transferred to the atom is $\hbar(\mathbf{k}_1 - \mathbf{k}_2) =: \hbar\mathbf{k}_{\text{eff}}$ which equals the sum of the photon momenta

2.1. Atom Interferometer in Gravity

in the case of counter-propagating beams. Energy and momentum conservation require that the difference in frequency of the two beams satisfies

$$\omega_{12} = \omega_{\text{hfs}} - \frac{\hbar}{2m} \mathbf{k}_{\text{eff}}^2 \quad (2.4)$$

where m is the mass of the atom.

This scheme combines the advantage of metastability of the microwave transition—enabling interferometer sequences over extended periods only limited by the geometry of the apparatus—with the large momentum transfer offered by optical photons. It is furthermore possible to very selectively address the atoms in momentum space through Doppler selection due to the exceptionally narrow linewidth of the hyperfine splitting [68]. This comes without the need of ultra-stable lasers as only the difference in laser frequencies needs to be controlled with high precision, which is comparatively easy.

A detailed analysis of the three-level system including coupling to the wave-packet's momentum can be found in [60, 61]. For further discussion it is necessary to recall some of the results.

As only certain impulses are allowed, it is convenient to describe the atom in a basis of states of the form

$$a_{j,p'} \exp \left[-i \left(\omega_j^A + \frac{p'^2}{2m\hbar} \right) t \right] |j, p'\rangle \quad (2.5)$$

where ω_j^A is the energy of the j th level and the width of the wave-packet in momentum space is negligible. The atom is subjected to a light field comprising two beams

$$\mathbf{E} = \frac{1}{2} \mathbf{E}_1 e^{i(k_1 z - \omega_1 t)} + \frac{1}{2} \mathbf{E}_2 e^{i(k_2 z - \omega_2 t)} + \text{c.c.} \quad (2.6)$$

which couples to the states $|1, p\rangle$, $|2, p + \hbar k_{\text{eff}}\rangle$ and $|3, p + \hbar k_1\rangle$ by dipole interaction.⁴

Neglecting spontaneous decay from the strongly detuned upper level and applying the Rotating Wave Approximation to the Schrödinger equation, a set of equations is obtained which govern the time evolution of the atom

⁴This approach neglects weak cross-coupling of e. g. $|3, p + \hbar k_2\rangle$ and $|1, p\rangle$ through ω_2 . Indeed as can be seen in figure. 3.26 some other close-by hyperfine levels of ^{87}Rb would need to be considered, too. However, this does not add anything profoundly new to the situation, as all intermediate states can be eliminated adiabatically. The influence of close-by transitions only needs to be taken into account, when the AC Stark shift is evaluated.

2. Theory

during laser pulses

$$\dot{a}_{1,p} = \frac{i}{2}\Omega_1 e^{i\Delta t} a_{3,p+\hbar k_1} \quad (2.7a)$$

$$\dot{a}_{2,p+\hbar k_{\text{eff}}} = \frac{i}{2}\Omega_2 e^{i\Delta t} a_{3,p+\hbar k_1} \quad (2.7b)$$

$$\dot{a}_{3,p+\hbar k_1} = \frac{i}{2} \left(\Omega_1 e^{-i\Delta t} a_{1,p} + \Omega_2 e^{-i\Delta t} a_{2,p+\hbar k_{\text{eff}}} \right) \quad (2.7c)$$

where

$$\Omega_j := -\frac{e \langle j | \mathbf{E}_j \cdot \mathbf{r} | 3 \rangle}{2\hbar} \quad (2.8)$$

is the usual Rabi frequency.

Observing that the hyperfine ground-states fluctuate much slower than Δ , the upper level can be eliminated adiabatically. After further dropping terms oscillating with ω_{12} , a system of equations very similar to that of a two-level-system is recovered

$$\dot{a}_{1,p} \approx i\Omega_1^{\text{AC}} a_{1,p} + ie^{i\delta t} \Omega_{\text{eff}} a_{2,p+\hbar k_{\text{eff}}} \quad (2.9a)$$

$$\dot{a}_{2,p+\hbar k_{\text{eff}}} \approx i\Omega_2^{\text{AC}} a_{2,p+\hbar k_{\text{eff}}} + ie^{-i\delta t} \Omega_{\text{eff}}^* a_{1,p} \quad (2.9b)$$

with

$$\begin{aligned} \Omega_j^{\text{AC}} &:= \frac{|\Omega_j|^2}{\Delta}, \quad \Omega_{\text{eff}} := \frac{\Omega_1 \Omega_2^*}{\Delta} \\ \delta &:= (\omega_1 - \omega_2) - \omega_{12} - \frac{\mathbf{p} \cdot \mathbf{k}_{\text{eff}}}{m} \end{aligned} \quad (2.10)$$

Ω_{eff} is an effective two-photon Rabi-frequency. The detuning δ is defined with respect to a Doppler-shifted resonance without AC Stark shifts, and it is the sensitivity to this detuning which enables phase measurements in the interferometer, as will be seen later. An influence of some importance in highly precise measurements is the weak coupling of the ground levels to the intermediate level denoted as Ω_j^{AC} here.

It is useful to state the solution of (2.9) for a slightly detuned Raman pulse as to identify possible systematic effects. For $\omega\tau = \pi/2 + 2\epsilon$ —where ω is the effective cycling frequency of the slightly detuned transition and ϵ is a small deviation from a perfect $\pi/2$ -pulse—these equations take the form [61]

$$\begin{aligned} a_{1,p}(t_0 + \tau) &= \exp[i(\delta\tau/2 - \varphi_{\text{AC}})] \frac{1}{\sqrt{2}} \left((1 - \epsilon) \exp[-i\varphi_{\text{off}}] a_{1,p}(t_0) \right. \\ &\quad \left. + (1 + \epsilon) \exp\left[i\left(\delta t_0 + \frac{\pi}{2}\right)\right] a_{2,p+\hbar k_{\text{eff}}}(t_0) \right) \end{aligned} \quad (2.11a)$$

2.1. Atom Interferometer in Gravity

$$a_{2,p+\hbar k_{\text{eff}}}(t_0 + \tau) = \exp[i(-\delta\tau/2 - \varphi_{\text{AC}})] \frac{1}{\sqrt{2}} \left((1 - \epsilon) \exp[i\varphi_{\text{off}}] a_{2,p+\hbar k_{\text{eff}}}(t_0) + (1 + \epsilon) \exp\left[i(-\delta t_0 + \frac{\pi}{2})\right] a_{1,p}(t_0) \right). \quad (2.11b)$$

Accordingly a nearly perfect π -pulse of the length 2τ yields

$$a_{1,p}(t_0 + 2\tau) = \exp[i(\delta\tau - 2\varphi_{\text{AC}})] \left(\exp\left[i(\delta t_0 + \frac{\pi}{2})\right] a_{2,p+\hbar k_{\text{eff}}}(t_0) + O((\delta_{\text{AC}} - \delta) + \epsilon) a_{1,p}(t_0) \right) \quad (2.12a)$$

$$a_{2,p+\hbar k_{\text{eff}}}(t_0 + 2\tau) = \exp[i(-\delta\tau - 2\varphi_{\text{AC}})] \left(\exp\left[i(-\delta t_0 + \frac{\pi}{2})\right] a_{1,p}(t_0) + O((\delta_{\text{AC}} - \delta) + \epsilon) a_{2,p+\hbar k_{\text{eff}}}(t_0) \right) \quad (2.12b)$$

where the small remnants in the original state can be neglected as they do not contribute to the output of the interferometer. Here the abbreviations

$$\varphi_{\text{AC}} := \frac{\Omega_1^{\text{AC}} + \Omega_2^{\text{AC}}}{2} \tau, \quad \delta_{\text{AC}} := \Omega_2^{\text{AC}} - \Omega_1^{\text{AC}}, \quad \varphi_{\text{off}} \approx \frac{\delta_{\text{AC}} - \delta}{\Omega_{\text{eff}}} (1 + 2\epsilon) \quad (2.13)$$

are used.

During light interaction various phase factors are imprinted into the atom. These need to be considered in detail. The main contribution comes from a detuning δ from perfect resonance of the $|1\rangle - |2\rangle$ -transition. If the state is swapped, a phase shift of $\delta(t_0 + \tau/2)$ in case of a $\pi/2$ -pulse or $\delta(t_0 + \tau)$ for a π -pulse is acquired with the sign dependent on the atoms initial state. This shift can be interpreted as the phase of the perturbation at the midpoint of the pulse and justifies to treat the effect of the Raman pulse as occurring at a specific point in time.

For an atom accelerated with respect to the lasers in rest, δ is caused by a growing Doppler shift with opposite sign for the counterpropagating beams and can be written as

$$\delta(t) = \frac{v_{\text{atom}}}{c} (\omega_1 + \omega_2) = (v_0 - g t) k_{\text{eff}}. \quad (2.14)$$

The imprinted phase is obtained as the integral over the time-dependent frequency, which gives

$$\phi(t_0) = \int_0^{t_0} \delta dt = v_0 t_0 - \frac{1}{2} g t_0^2, \quad (2.15)$$

2. Theory

recovering the position dependence used in the simplified picture from the beginning of this chapter. The interferometer phase is thus the same if assessed in a frame falling with the atoms or at rest with the lasers, as could be expected.

Related to the detuning is a factor of $\exp[\pm i\delta\tau/2]$ acquired during $\pi/2$ -pulses without changing state, which is troublesome and needs to be suppressed, see below. Additions of $\pi/2$ during change of state ensure a phase difference of π between both outputs of the interferometer.

The phases φ_{AC} and φ_{off} relate to combinations of the AC Stark shifts of the ground levels. φ_{AC} is common to both paths of the interferometer on a per-pulse basis and therefore cancels if light intensities along the beams are unchanged over the spatial separation of the two paths. φ_{off} occurs in $\pi/2$ -pulses when conditions of perfect resonance are not met—a situation which is unavoidable with non-uniform intensities of Gaussian laser beams as the AC Stark shifted frequency varies over their aperture. The effect would only cancel if the situation was perfectly symmetric, which would require that laser intensities as much as size and position of the atomic cloud are stable over the course of the interferometer. The latter is difficult to achieve due to finite velocities of the laser cooled atoms, which gives rise to a significant systematic in a high precision atom interferometer [48]. The effect can be suppressed by choosing a ratio of laser intensities where the AC Stark shifts of both ground levels become the same and their difference—which leads to φ_{off} —therefore cancels. This is possible even if various cross-couplings are taken into account, as each separate shift caused by a particular coupling is dependent on the detuning of the corresponding laser frequency from the addressed optical transition; see also [70] for a detailed calculation.

2.1.2. Thick Beamsplitters

The analysis outlined above is helpful to understand some characteristics of light-matter interaction and to identify a harmful systematic effect. But it is sufficient only if the effect of the beamsplitters on the wave-packet's shape and trajectory can be neglected. With the high precision obtainable in an instrument like the one described here, such modifications have to be taken into consideration, especially when evolution of the atom is influenced by additional gravito-inertial fields.

When a laser pulse is applied, the atom propagates through a periodic potential similar to a "light crystal". As in e.g. diffraction of neutrons in highly ordered materials, this results in an altered dispersion relation

2.1. Atom Interferometer in Gravity

for those waves allowed to travel in the crystal. For an (effective) two-level system an analytical treatment is given in [62], yielding the condition

$$\left(\frac{(\mathbf{p} + \hbar \mathbf{k}_{\text{eff}})^2}{2m} - E' - \hbar \Delta \right) \left(\frac{\mathbf{p}^2}{2m} - E' \right) - \hbar^2 \Omega_{\text{eff}}^2 = 0 \quad (2.16)$$

with $E' = E - \frac{1}{2}(E_1 + E_2) - \frac{\hbar}{2}\Delta$, E the total energy and $E_{1,2}$ the energies of the ground states. For a given E' this fourth-order equation allows for four momenta, that is $\mathbf{p}_{1,2}$ and $\mathbf{p}_{1,2} + \hbar \mathbf{k}_{\text{eff}}$, where for the z-component $p_1^z = p_2^z$ due to the symmetry of the situation.

Propagation of the wave-packet is governed by its group velocity v , which is not necessarily proportional to the momentum due to the modified dispersion relation. Instead

$$v = \nabla_p E' \quad (2.17)$$

which for the interesting z-component gives

$$v_{1,2}^z = \frac{p^z}{m} + \frac{1}{2} \left(1 \pm \frac{y}{\sqrt{1+y^2}} \right) \frac{\hbar k_{\text{eff}}}{m}, \quad (2.18)$$

where

$$y := \frac{1}{2\hbar\Omega_{\text{eff}}} \left(\frac{(\mathbf{p} + \hbar \mathbf{k}_{\text{eff}})^2}{2m} - \mathbf{p}^2 - \hbar \Delta \right) \quad (2.19)$$

vanishes in case of perfect resonance. This is an interesting result as it states that if $y = 0$ the wave-packet does split only after the light pulse. Before both parts evolve along the same curve, which is given by the mean of the unperturbed path and that carrying the additional momentum from the two photons. Deviation from the resonance condition will result in four distinct parts, where two pairs differ in the photon momentum carried and the constituents of each pair in the momentum perpendicular to the beam. Such cases would complicate the interpretation of experimental results considerably.

As covered in [71] gravitational acceleration during the beamsplitter process leads to such a detuning and consequently to significant changes to the beamsplitter-process. This is why it is good practice in atom gravimeters to compensate the growing Doppler shift by adequately tuning ("chirping") the laser frequencies. The information otherwise read from the phase difference between the two paths is thus shifted into the rate with which the frequency needs to be chirped in order to retain resonance, indicated by all atoms being in the initial state in the interferometer output.

2. Theory

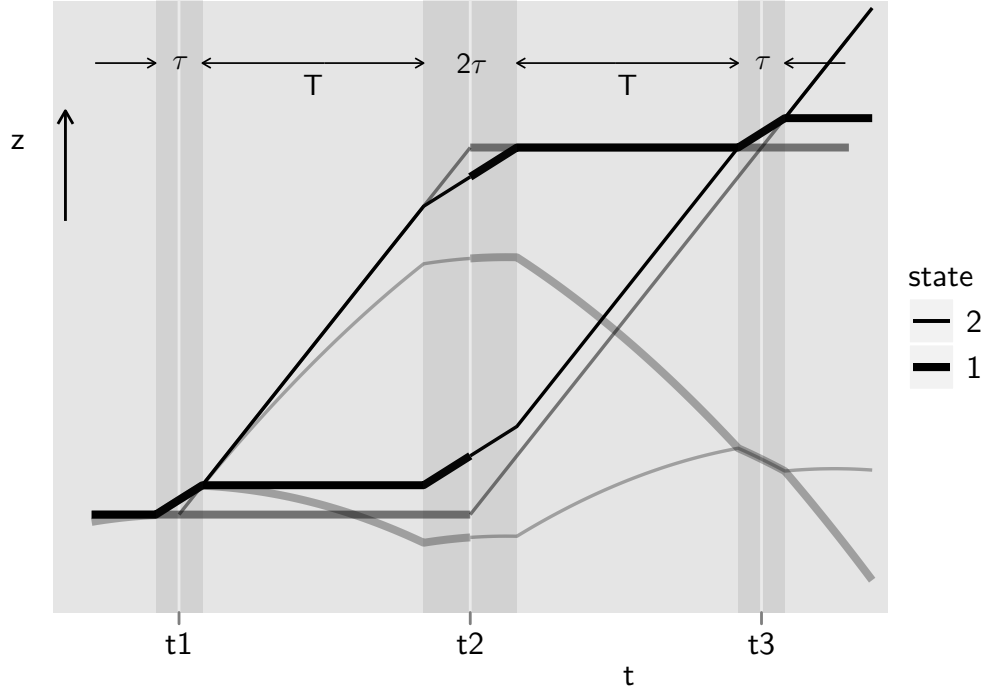


Figure 2.3.: Trajectories due to modified propagation during light pulses. The limit of infinitely thin beamsplitters (**light grey, straight**) is to be compared to the situation where both paths feature the same group velocity in the "light crystal" (**black**). To obtain a comparable picture with gravity (**light grey, bent**) the laser frequencies have to be chirped in order to retain resonance.

The change in group velocity during light interaction implies a spatial shift and consequently corrections to the phase acquired in successive beamsplitters even for the "unperturbed" path. This also slightly affects the dependence of the interferometer on g , making a re-evaluation necessary.

Full analytic treatment of the atoms subjected to strong electro-magnetic interaction is only possible for certain spatial or temporal geometries of the light fields. For a rectangular profile in the time domain (square pulses) the details have been worked out in [72] with a discussion of the case of interest here: a three-pulse interferometer with the spatio-temporal Mach-Zehnder geometry from above and pulse durations of τ and 2τ respectively, separated by periods of free evolution of length T .

The result is that if the width of the initial wave-packet in momentum

space is smaller⁵ than $m\Omega_{\text{eff}}/k_{\text{eff}}$, further dispersive effects of the beamsplitter can be neglected. Due to the altered trajectories in the beamsplitters of finite length, the interferometer geometry then resembles figure 2.3 and the overall phase shift⁶ becomes

$$\Delta\phi_{\text{light}} = \mathbf{k}_{\text{eff}} \cdot \mathbf{g}T(T + 2\tau) + \varphi_{\text{bsp}} \quad (2.20)$$

where the modified time dependence can be attributed to the adjusted spatio-temporal area enclosed by the two interferometer arms. An additional phase φ_{bsp} of the order $O(T\tau)$ is to be added, if the condition $y = 0$ is not met at all times.

It is further worth noting, that the action of the beamsplitter can still be reduced to an instantaneous effect at a specific point in time (*generalized ttt scheme* [72]), while the atom is otherwise considered to evolve under influence of the external fields only, albeit on perturbed trajectories. This is the justification for a separate treatment of light fields and free evolution, even in the case of strong laser fields.

2.1.3. Free Evolution

While the biggest part of the phase shift accumulated in the interferometer sequence is due to light interaction, understanding the effect of external fields acting on the atoms is crucial to make highly accurate measurements. Especially non-uniform inertial fields need to be taken into account, as these shift the energy of the two arms of the interferometer differently, which possibly leads to a significant phase offset.

Calculating the propagation of the wave-packets by solving the Schrödinger equation over full periods between light-interaction would be cumbersome, especially when variable fields are involved. A treatment in the position picture is then appropriate, where the advantage of the momentum picture—each component can be treated separately in a closed family with a finite number of states—is lost.

The situation is alleviated considerably if the action

$$S_{\Gamma} = \int_{t_a}^{t_b} dt L[z(t), \dot{z}(t)] \quad (2.21)$$

along the possible paths Γ an atom can take is much larger than \hbar , that is in

⁵This can be ensured by selecting a narrow velocity class of atoms, see the next chapter.

⁶This holds in the limit of very small detuning, that is very small gravity or adequately chirped lasers.

2. Theory

the classical limit of macroscopic paths. This results in the phase S_Γ/\hbar of a matter wave assumed to follow Γ to be a highly oscillatory function of even microscopic path variations, as long as it is not the path which makes S_Γ stationary. In such case only the neighbourhood of the distinguished path Γ_{cl} will add significantly when contributions of all possible paths starting from a certain point $z_a := z(t_a)$ are allowed to interfere in a chosen endpoint $z_b := z(t_b)$. According to the principle of stationary action Γ_{cl} is the path a classical particle would travel along and, with the reasoning just given, also the path which determines the phase of a quantum particle in the classical limit.

This limit defines the picture in which a description of an atom interferometer as in figure 1.1 makes sense. The depicted paths are those the centres of mass of the atom's wavepacket fragments can be thought of to propagate on. This is not exactly true as the contributions of all possible variations of the path need to be summed at the endpoint, but those not very close to the classical path do vanish due to destructive interference. As detailed in e.g. [73], if additionally the Lagrangian of the system is at most quadratic in coordinates and momentum, the Feynmann path integral can be separated so that the phase of the quantum particle at z_b is only given by its initial phase and the—now classical—path integral along Γ_{cl} .

Applying this principle to the problem of free evolution greatly simplifies the calculation. For the phase in the interferometer this gives

$$\Delta\phi_{\text{free}} = \frac{1}{\hbar} \oint_{\Gamma_{\text{cl}}} L dt \quad (2.22)$$

where Γ_{cl} is the closed loop formed by path A and B concatenated together. If unknown, the precise trajectories can be derived from e.g. the Euler-Lagrange equation.

In the case of uniform acceleration g the Lagrangian reads

$$L = \frac{m}{2} \dot{z}^2 - mgz \quad (2.23)$$

which needs to be integrated along sections of the well-known form

$$z(t) = z_a + \dot{z}_a(t - t_a) - \frac{1}{2}g(t - t_a)^2, \quad (2.24)$$

where $\dot{z}_a := \dot{z}(t_a)$.

The interferometer loop consists of four sections (first/second half, upper/lower path) where initial velocities differ by $v_{\text{rec}} = \pm \frac{\hbar k_{\text{eff}}}{m}$ between

concurrent sections. Obeying the orientation of the path during integration yields indeed vanishing action after some straight-forward calculations.

2.1.4. Gravity Gradient

On Earth's surface a scalar gravity gradient of about $\gamma = 3 \times 10^3 \text{ nm s}^{-2}/\text{m}$ is present, leading to a significant difference in acceleration of approximately 750 nm s^{-2} over the height of a typical interferometer sequence and 10 nm s^{-2} over the spatial separation of the paths.

The Lagrangian now takes the form

$$L = \frac{m}{2} \dot{z}^2 - mgz + \frac{m}{2} \gamma z^2 \quad (2.25)$$

from which the classical path can be derived by evaluating the Euler-Lagrange equation, giving

$$z(t) = \frac{g_0}{\gamma} + \left(z_0 - \frac{g_0}{\gamma} \right) \cosh(t\sqrt{\gamma}) + \frac{v_0}{\sqrt{\gamma}} \sinh(t\sqrt{\gamma}) \quad (2.26a)$$

$$\dot{z}(t) = \left(z_0 - \frac{g_0}{\gamma} \right) \sqrt{\gamma} \sinh(t\sqrt{\gamma}) + v_0 \cosh(t\sqrt{\gamma}). \quad (2.26b)$$

The hyperbolic trajectories resulting from the small linear component on top of the constant background lead to some deviations from the situation from before, most notably a small gap Δz in the endpoints of the two paths of a few Å. This is not harmful as the width of the wavepacket is at least $4 \mu\text{m}$ ⁷, ensuring almost unaffected overlap. A small difference in the end-velocities of $\approx 2 \times 10^{-2} \text{ nm/s}$ gives rise to a very slow beat of the two wavepackets in each output. With time spans of about 150 ms between the last Raman pulse and detection and a mean velocity of roughly 2 m/s the resulting phase offset of $\approx 1 \mu\text{rad}$ is negligible.

The lengthy calculation of the phase from the action along the hyperbolic paths is best done using computer algebra. When adding a small contribution $p\Delta z/\hbar$ from a non-classical path segment to bridge the gap between end-points [73], the obtained result is

$$\Delta\phi_{\text{grad, free}} = k_{\text{eff}} \left(\frac{v_{\text{rec}}}{2\sqrt{\gamma}} (\sinh(2T\sqrt{\gamma}) - 2\sinh(T\sqrt{\gamma})) \right), \quad (2.27)$$

⁷Estimated from the uncertainty in the initial momentum after velocity selection, see next chapter for experimental details.

2. Theory

which amounts to 3 mrad or 4 nm s⁻² for typical T = 230 ms and gradients as given above, and becomes important for highly accurate measurements.

However, the effect on the contribution from laser phase is much larger. Calculating the phase from the position of the atoms at times of the Raman pulses⁸ yields

$$\Delta\phi_{\text{grad, light}} = \frac{4}{\gamma} \sinh^2 \left(\frac{T\sqrt{\gamma}}{2} \right) ((\gamma z_0 - g_0) \cosh(T\sqrt{\gamma}) + \sqrt{\gamma} v_0 \sinh(T\sqrt{\gamma})), \quad (2.28)$$

which leads to a shift of -0.520 rad or -610 nm s⁻² under typical experimental conditions, where v₀ = 2.2 m/s and z₀ = 0 is the chosen height of the first pulse.

If expanded in γ to first order, measured gravity due to the laser phase is written as

$$g_{\text{grad, light}} = g_0 - \gamma \left(z_0 + \left(v_0 + \frac{\hbar k_{\text{eff}}}{2m} \right) T - \frac{7}{12} g_0 T^2 \right) + O(\gamma^2). \quad (2.29)$$

From the expression in brackets a gradient-dependent height-correction can be drawn, specifying the point at which the actual value of g equals the measured one. This is at 1.35 m—close to the apex—for a height of the first pulse of 1.15 m. It is also evident that in order to determine g with an accuracy of 5 nm s⁻², the height of the interferometer needs to be known with an uncertainty of ≈ 1 mm.

2.1.5. Transfer Function of the Interferometer

To ease characterization of the instrument, it is useful to be able to calculate the impact of observed perturbations on the outcome of the interferometer. A convenient method is the sensitivity function, which gives the relation between small phase fluctuations $\delta\phi$ occurring at random times in the Raman beams and the resulting shift $\Delta\phi(\delta\phi, t)$ deduced from the ratio of atoms. In a further step the transfer function can be derived from the Fourier transform of the sensitivity function, which is helpful to assess e.g. the variance in measured values of g resulting from a given spectral distribution of noise densities.

⁸Exactly the same results for the contributions of free evolution and laser interaction are obtained by Bordé in [65], using a framework which is the quantum-mechanical equivalent to the ABCD-matrices known from geometrical optics.

2.1. Atom Interferometer in Gravity

The sensitivity function is defined as

$$g(t) := \lim_{\delta\phi \rightarrow 0} \frac{\Delta\phi(\delta\phi, t)}{\delta\phi} \quad (2.30)$$

which for an atom interferometer measuring at the slope of the fringe can intuitively be evaluated being -1 for the first half of the interferometer sequence, +1 for the second and zero otherwise, as either the middle or the last Raman pulse write the resulting phase into the atoms. A small modification is necessary due to the finite width of the pulses, which is calculated in [74] to be

$$g(t) = \begin{cases} \sin(\Omega_{\text{eff}}(t+T)) & -T-2\tau \geq t > -T-\tau \\ -1 & -T-\tau \geq t > -\tau \\ \sin(\Omega_{\text{eff}}t) & -\tau \geq t > \tau \\ 1 & \tau \geq t > T+\tau \\ -\sin(\Omega_{\text{eff}}(t-T)) & T+\tau \geq t > T+2\tau \\ 0 & \text{else} \end{cases} \quad (2.31)$$

where for convenience $t = 0$ coincides with the middle of the π -pulse. The Fourier transform [74]

$$\begin{aligned} G(\omega) &:= \int_{-\infty}^{\infty} e^{-i\omega t} g(t) dt \\ &= \frac{4i\Omega_{\text{eff}}}{\omega^2 - \Omega_{\text{eff}}^2} \sin\left(\frac{\omega(T+2\tau)}{2}\right) \left(\cos\left(\frac{\omega(T+2\tau)}{2}\right) + \frac{\Omega_{\text{eff}}}{\omega} \left(\frac{\omega T}{2}\right) \right) \end{aligned} \quad (2.32)$$

can be used to examine fluctuations in the frequency domain. To this end one observes that (2.30) is equivalent to

$$\Delta\phi = \int_{-\infty}^{\infty} g(t) d\phi = \int_{-\infty}^{\infty} g(t) \frac{d\phi}{dt} dt. \quad (2.33)$$

Making use of the Plancherel theorem, this leads to

$$\text{Var}(\Delta\phi) = \int_{-\infty}^{\infty} |H(\omega)|^2 S_{\phi}(\omega) d\omega \quad (2.34)$$

where $S_{\phi}(\omega)$ is the power spectral density of the phase fluctuations and H the transfer function given by

$$H(\omega) := \omega G(\omega). \quad (2.35)$$

2. Theory

For the last definition it is used that with $h = e^{i\omega t}$

$$|\mathcal{F}(\dot{h})|^2 = \omega^2 |\mathcal{F}(h)|^2 \quad (2.36)$$

for any real-valued $\omega \neq 0$.

Vibrational noise is often the biggest concern in the gravimeter. It expresses itself as phase fluctuations caused by movements of the mirror reflecting the pair of Raman beams⁹, which can be quantified as

$$\delta\phi = \mathbf{k}_1 \cdot \delta\mathbf{z} - \mathbf{k}_2 \cdot \delta\mathbf{z} = k_{\text{eff}}\delta z. \quad (2.37)$$

Vibrations are easily measured as residual accelerations with suitable seismometers, which is why the transfer function is often needed for $\delta a = \ddot{\delta z}$. Using (2.36) again gives

$$H_a(\omega) = \frac{k_{\text{eff}}}{\omega} G(w). \quad (2.38)$$

As can be seen from figure 2.4, the interferometer exhibits a strongly modulated sensitivity to fluctuations when examined in the frequency domain with overall characteristics of a bandpass and a lowpass respectively. This is due to accumulation of said fluctuations in between and averaging during beamsplitters, limiting the susceptibility to certain ranges of frequencies.

The considerations from above do not account for the cyclic character of the interferometer. To cover extended periods in time, the interferometer sequence needs to be repeated with a (fixed) repetition rate. As every sampled system with a duty cycle less than unity, it thus becomes prone to aliased signals present at frequencies which are an integral multiple of the repetition frequency. However, this behaviour depends strongly on the coherence time of the noise signals, making e. g. high-frequency oscillations in electronic control loops particular cumbersome. Here the assumption of uncorrelated noise was made, where each measurement is independent from preceding cycles.

⁹Vibrations are far less critical for all other optical elements, as they affect both beams equally, so that the resulting deviations in phase cancel in the interferometer.

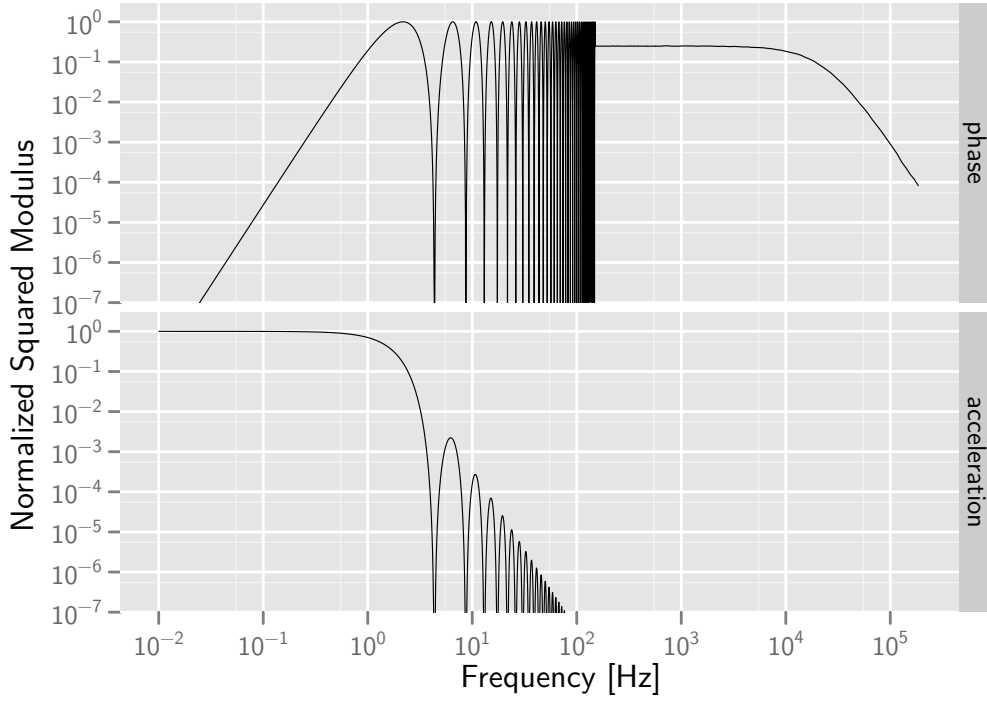


Figure 2.4.: Normalized transfer functions of phase and acceleration. For the calculation $T = 230$ ms and $\tau = 20$ μ s. For frequencies higher than 150 Hz only the mean is depicted.

2.2. Gravity Variations

A challenge associated with highly accurate determinations of local gravity is its pronounced variability in time and space, which can amount to up to 2000 nm s^{-2} during typical measurements. Often these variations are not the object of interest, but rather perturbations to be rejected to obtain the targeted accuracy of a few nm s^{-2} . The situation is further complicated by many of the disturbing sources not being fully understood or random and therefore hard to predict. Luckily these disturbances are often either of high frequency (vibrations), rare (e. g. rapid change of ground water level due to massive rain fall) or very slow (e. g. postglacial rebound of the crust, a few 10 nm s^{-2} per year) and can be filtered out.

An influence which needs modelling to be removed is the time-dependent gravitational effect of celestial bodies, especially Sun and Moon, and the elastic and inelastic answer of Earth's masses. While the former could be calculated rather straightforward from ephemerides, the latter is only

2. Theory

partly understood and subject of research which reaches back to the 18th century. Modern models include effects of a rotating ellipsoidal earth with elastic core, liquid outer core, inelastic mantle and some hydrodynamical aspects of mantle convection [75] complemented by the effects of large water masses (oceans and seas), their redistribution and resonant excitation as well as elastic reactions of the crust to their loading [76].

To connect these models with observations and to give predictions in a consistent manner, an agreed mode of description is needed. This is commonly done in the frequency domain. In time the most important contributions are of periods of half and full a day due to Earth's rotation, with thousands of frequencies needed if one wishes to account for the subtle influence of all planets in our system [77]. Still, most of the effect ($> 99\%$) is contained in a dozen spectral components related the dynamics of the sun and the moon [78]. To characterize a site from measurements or to communicate a prediction, amplitude- and phase-factors for each component are given, as in appendix A for the physics department of the Humboldt Universität zu Berlin. Here, the major part is from solid earth ($> 90\%$), with the rest caused primarily by oceanic tides (up to 10% close to coasts, dropping to a few percent inside continents). The remaining deviation found in measurements needs other explanations, see below.

In the space domain it has proven useful to develop Earth's gravity potential

$$V_{\oplus} = G \iiint \frac{dm}{s} \quad (2.39)$$

with G the Gravitational constant and s the distance of a point outside Earth's ellipsoid to the infinitesimal mass dm into a series of spherical harmonics Y_{lm}

$$V_{\oplus} = \frac{GM}{r} \left(1 + \sum_{l=1}^{\infty} \sum_{m=0}^l \left(\frac{a}{r} \right)^l C_{lm} Y_{lm} \right). \quad (2.40)$$

Here M is Earth's mass as the coefficient of the spherical harmonic of degree 0, a the major axis of the ellipsoid and r the distance to Earth's centre. This series converges rapidly and can be truncated at any degree l and order m when sufficient spatial resolution is reached. Modern approximations from large scale satellite measurements can go up to $l = m = 200$, equivalent to spatial resolutions of 100 km [79], and are patched with local gravimetry when higher resolution is needed. To assess the gravitational modulation the (time-varying) gravity potential of celestial bodies can also

be developed around earth as such a series [80]. From these, predictions can be derived with the help of the models from above.

Sensitive measurements with a resolution of 100 nm and below also need correction for polar motion, variations in Earth’s rotational frequency and local weather. Polar motion—the slow movement of Earth’s rotational axis with respect to its body—and length of day changes modulate the latitude dependent centrifugal acceleration and are easily corrected for when known, e. g. from the International Earth Rotation and Reference Systems Service [81].

The impact of atmospheric fluctuations is much harder to predict. It can be split into gravitational pull and elastic loading of the crust leading to height changes, which both modulate with barometric pressure. To be modelled correctly, information about local air distribution as well as local geology is necessary [82], making exact predictions tedious. Therefore for standard gravimetric measurements these effects are most often estimated by a simple linear factor of $3 \text{ nm s}^{-2}/\text{hPa}$ and referenced to the site-dependent standard pressure

$$p_n = 1013.25 \left(1 - \frac{0.0065h}{288.15} \right)^{5.2559} [\text{hPa}] \quad (2.41)$$

with h the topographic elevation.

To ease the calculations in strive for a prediction of local gravity changes, several programs are available. One is TSoft, developed by the Royal Observatory of Belgium [83], which can compute synthetic tides of solid earth natively and the effects of polar motion and ocean loading when given appropriate parameter sets. A comprehensive source for ocean loading coefficients calculated for a given site is [84]. A typical dataset obtained from such computations is shown in figure 2.5 and later used for corrections of a first long-term measurement, see section 4.2.

2. Theory

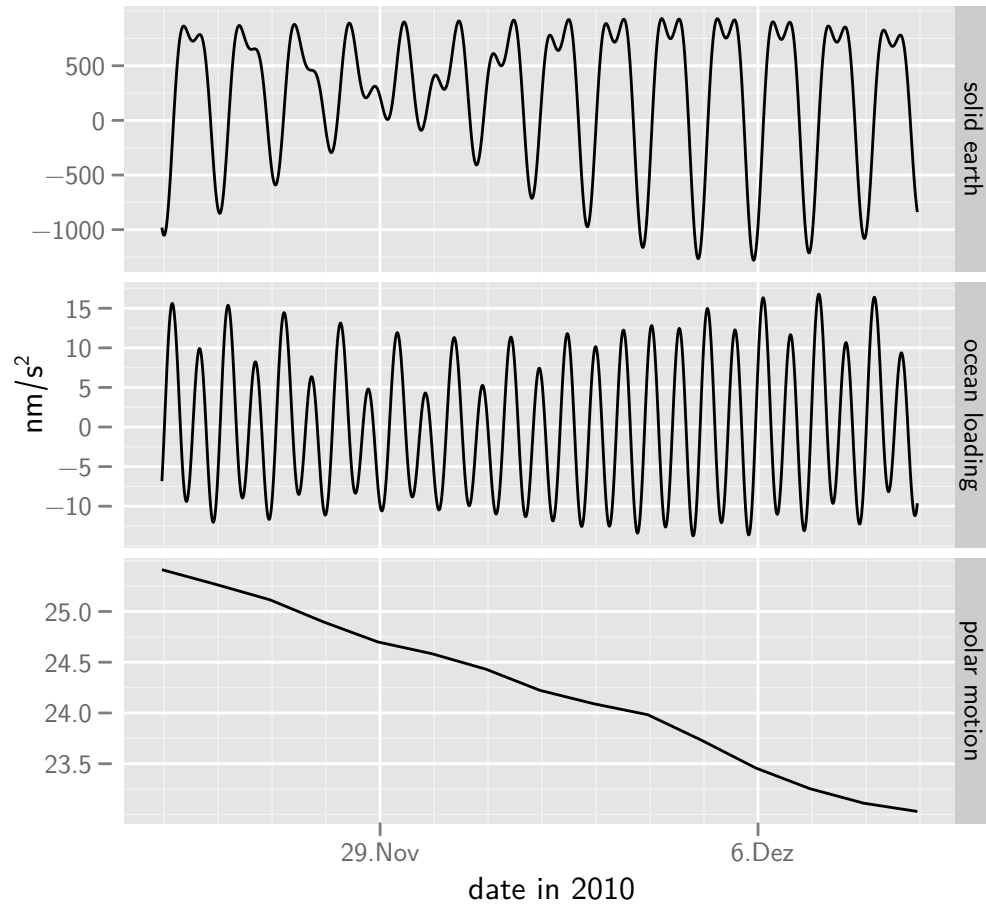


Figure 2.5.: Predicted tides including solid earth, ocean loading and polar motion effects for a location close to the physics department of HU-Berlin. The typical modulation due to Sun and Moon is apparent.

3. Experiment

To obtain high precision measurements with the atom interferometer, some care has to be taken when preparing and launching the atoms. First, a suitably high number of atoms has to be collected and cooled to sub-Doppler temperatures, which is done in a MOT with adjacent optical molasses. The cloud of cold atoms is then launched upwards with the help of light forces and subjected to a series of selection processes in order to obtain a pure sample with low momentum spread in a magnetic insensitive internal state. This sample is processed in the actual interferometer sequence in a zone well shielded from external influences close to the apex of its free flight parabola. On its way down, the two outputs of the interferometer are interrogated by detection of resonantly scattered light, from which the ratio of atoms in the outputs and thus the phase shift between the two arms of the interferometer can be deduced. This procedure—from here on referred to as a "shot"—takes a bit more than a second, and is repeated in an endless loop to obtain a time series of gravitational data. In the following sections a more detailed walk through the apparatus and the necessary steps is given.

Due to the absolute nature of the measurements to be taken, systematic effects are of highest importance and have been examined thoroughly in previous work [61, 85–87]. Still there are areas found, where the published results lack the details necessary to cover all thinkable aspects of erroneous effects. While not yet studied in greater detail, some considerations to possible influences are added, when appropriate.

3.1. Preparing the Atoms

The choice of ^{87}Rb as the atomic species for the interferometer is motivated mostly by its first optical resonances being in the near infrared, which can be addressed conveniently by diode lasers. These devices and suitable light amplifiers based on the same semiconductor technology allow for small, rigid and comparably cheap light sources for the optical system; qualities most valuable in transportable devices. The D_2 -resonance offers furthermore a strong cycling transition from $5^2\text{S}_{1/2}, F = 2$ to $5^2\text{P}_{3/2}, F' = 3$ with

3. Experiment

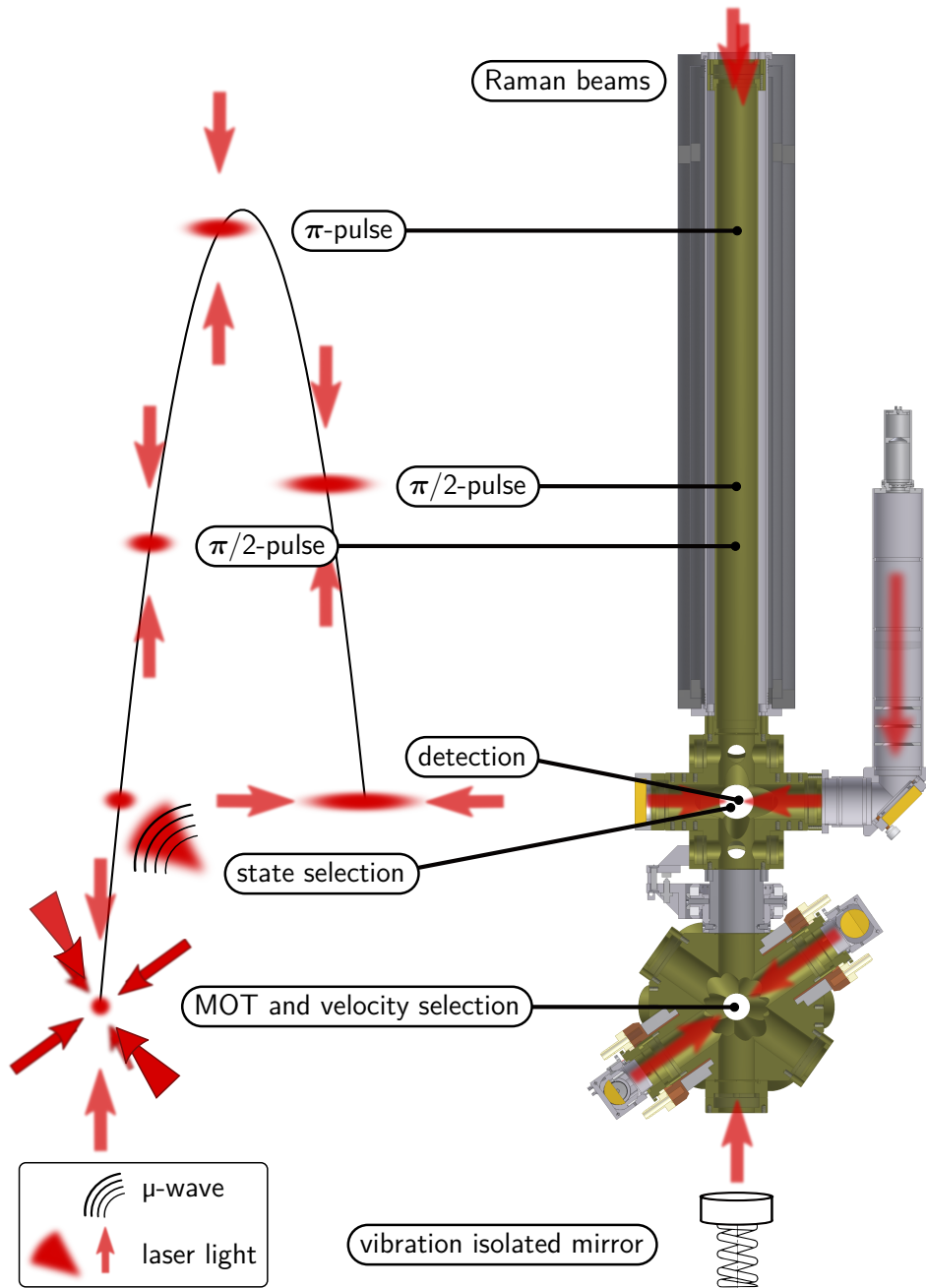


Figure 3.1.: Steps in a measurement cycle and their corresponding positions in the fountain apparatus. For clarity the flight parabola has been spread sideways; in reality the atoms are launched exactly vertical.

only a small escape probability along the $F' = 2$ hyperfine level, which suggests a scheme for the laser frequencies as depicted in figure 3.26.

3.1.1. MOT and Optical Molasses

The cold Rb-atoms are prepared in a MOT in 1-1-1-configuration [88] from low density thermal background. The Rb-vapour is provided by means of resistively heated dispensers manufactured by SAES getters. They allow for fine grained control over vapour pressure by adjusting the heating current and release a natural isotope mixture containing approximately 27 % of ^{87}Rb with low contamination by other substances. The yield of a pair of standard dispensers was found to be sufficient for more than 1500 h of continuous operation.

The cooling beams feature a $1/e^2$ diameter of 30 mm and 20 mW of laser power per beam. From 10^{-9} hPa of Rb vapour close to 10^9 atoms are accumulated in 595 ms into a roughly spherical cloud of about 5 mm in diameter.

After switching off the Anti-Helmholtz-coils and an additional eddy current decay time of 5 ms an optical molasses with growing red-detuning of up to 20Γ (Γ being the natural line width) of the cooling beams follows. The far-detuned phase is ended after 3 ms by adiabatically cutting off the cooling light and retaining the repumper for another millisecond, in order to have all atoms in the $F = 2$ hyperfine ground state. When magnetic background fields are carefully compensated for with the help of three perpendicular pairs of Helmholtz coils fixed around the MOT assembly, this procedure gives a temperature deduced from the velocity spread of the atoms of $6\text{ }\mu\text{K}$, limited by short term fluctuations. These were found to correlate strongly with variations of the background magnetic flux, probably caused by technical equipment in the laboratory. It seems likely that lower temperatures can be achieved when their influence is removed through suitable shielding.

During the last 2 ms of the optical molasses the upper and lower triplet of cooling beams are detuned symmetrically from their mean by $\Delta\nu$ to the red and blue respectively. This defines a Doppler-shifted frame moving upwards with a velocity of

$$v = \Delta\nu\sqrt{3}\lambda \quad (3.1)$$

where λ is the laser wavelength. Driven by the unbalanced light forces, the atoms accelerate to v , which amounts to 4 m/s for a detuning $\Delta\nu = 3\text{ MHz}$.

3. Experiment

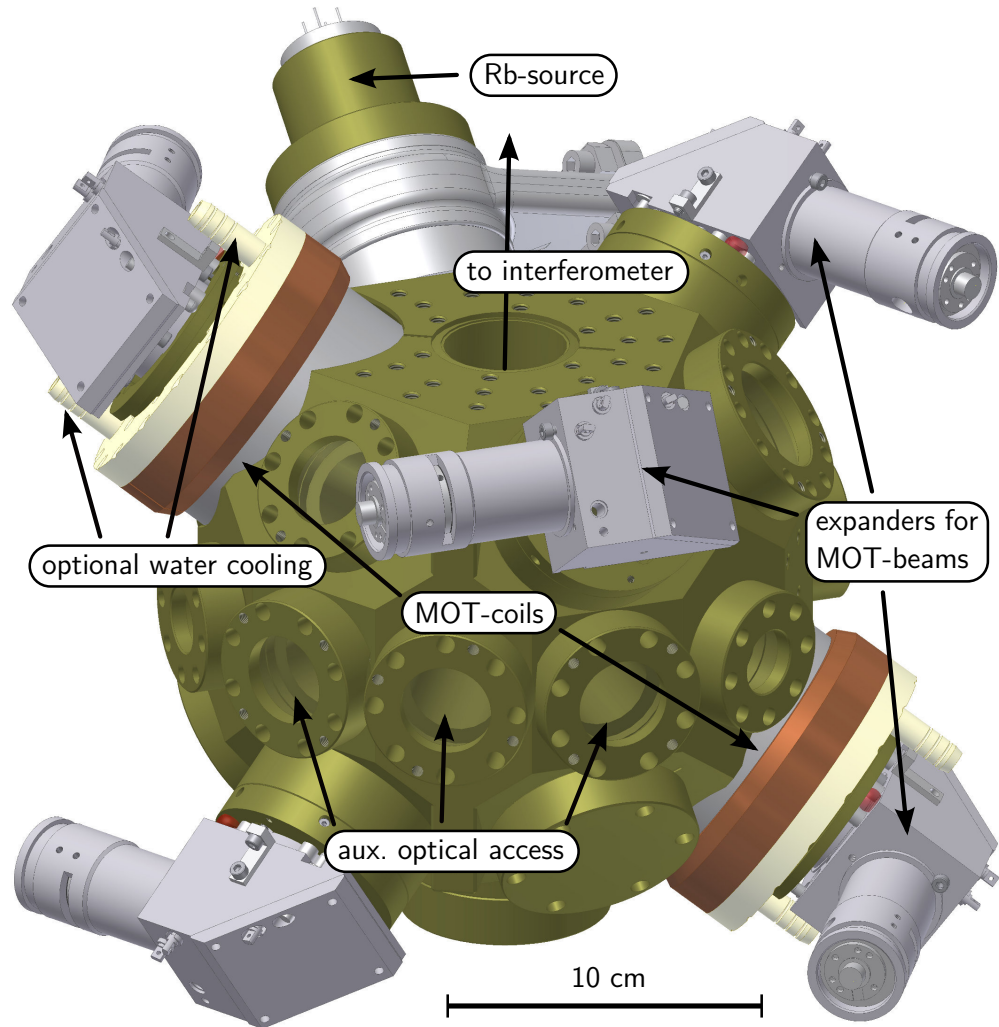


Figure 3.2.: CAD-drawing of the MOT-chamber. The main body was machined from a single block of Ti-5Al-2.5Sn. Attached are beam-expanders and coils designed to fit into the available space.

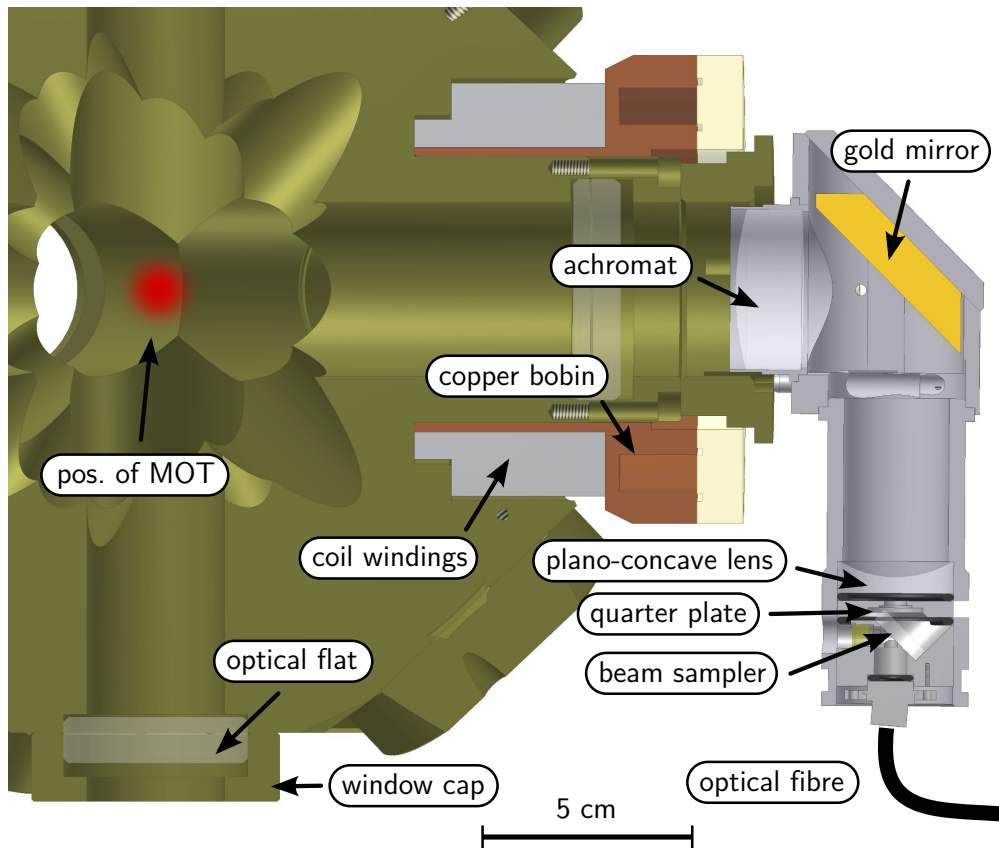


Figure 3.3.: Cut through MOT-chamber, coil and beam-expander.

3. Experiment

After switching off the light beams, this motion becomes the starting point of a free flight parabola peaking 815 mm above the MOT after 408 ms.

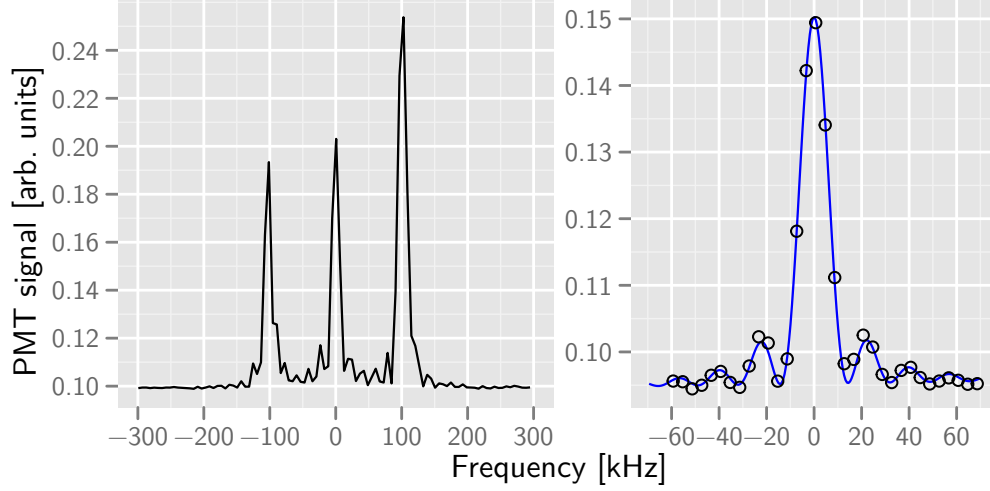


Figure 3.4.: (left) By scanning the difference frequency between the co-propagating Raman beams, magnetic sublevels can be selectively addressed. As both co-propagating beams feature the same polarization (σ^\pm), only transitions with equal magnetic sublevel in the initial and final state are allowed. Starting from $|F = 2\rangle$, three sublevels in $|F = 1\rangle$ are available and thus three peaks are observed. The shown frequency splitting is equivalent to a magnetic flux present at the location of the atoms of $7.2 \mu\text{T}$. (right) A closer look at a single resonance reveals a structure well described by Rabi transitions with fixed pulse-length and variable detuning. For this measurement a shorter π -pulse with square enveloped was applied, in contrast to the otherwise used Gaussian pulses.

The vacuum chamber for the MOT was designed with the special demands of a transportable and rugged device for field use in mind. To minimize overall size, and to maximize number and diameter of viewports, an approach was taken where the entire chamber is milled from a single block. The material of choice is a titanium alloy, as the low density results in low weight ($\approx 14 \text{ kg}$), even if larger quantities of metal are present when compared to chambers welded together from tubes. An additional advantage is the low specific conductivity, resulting in high ohmic resistance and therefore short decay times for eddy currents. It was found that the switch-off time for the MOT-fields is shorter than 5 ms with the rather large cross-sections in place depicted in figure 3.3.

3.1. Preparing the Atoms

Two cylindrical recesses were cut into the chamber where the Anti-Helmholtz-coils wound on slitted copper bobbins are mounted concentrically to a pair of opposing cooling beams. This configuration gives a magnetic flux gradient of 0.5 mT/cm at a current of only 8 A in the region of the MOT, which eliminates the need for cumbersome water cooling.

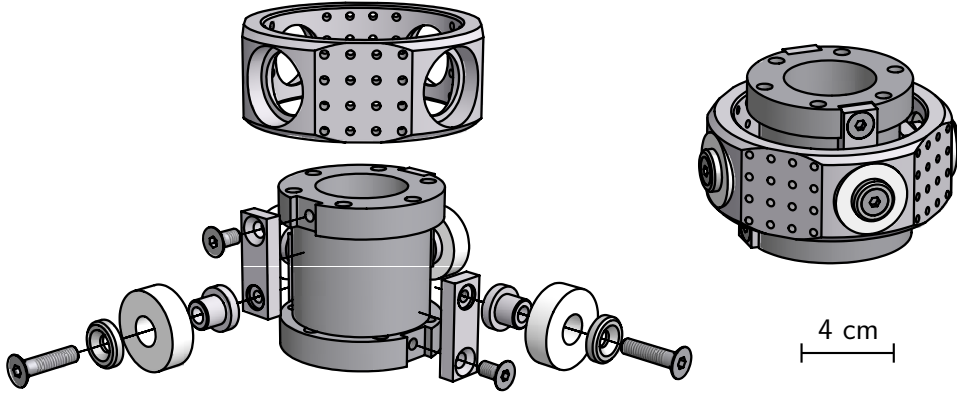


Figure 3.5.: Vacuum Pivot exploded (**left**) and in assembled form (**right**).

The cooling beams are delivered by folded collimators attached directly to the window caps holding the optical flats, which serve as view-ports. The collimators are designed to expand the cooling light coupled through polarization maintaining fibres to a diameter of 30 mm in a space-efficient way (f-number 3.6, still reasonably good beam quality, overall dimensions $50 \times 50 \times 130 \text{ mm}^3$). Special care was taken to use only materials with $\mu \approx 1$ to keep magnetic interference low.

The collimators also allow for precise steering of the beam through the chamber (six degrees of freedom), which is useful for initial alignment of the MOT beams. Here one triplet is first set to propagate colinearly with the respective boreholes, in order to profit from tight machining tolerances when adjusting perpendicularity. The other triplet is then aligned so that every beam is anti-parallel to its opponent by maximising mutual coupling into the fibres. In a last step all beams are tilted vertically by 3 mrad to avoid large scale interference patterns, which were found to give unstable MOT conditions.

Afterwards, the collimators can be locked as the orientation of the atomic fountain is tuned by rotating the whole MOT-chamber around a point defined shortly above the chamber with a vacuum pivot. The pivot was

3. Experiment

designed to allow for angular movements with very low friction. As conventional parts often contain magnetizable components, ball-bearings made from glass and nylon were chosen. With only a small load acting on them (the weight of the MOT-chamber is almost fully compensated by the pressure difference), the bearings could be pre-stressed by fitting them snugly into suitable holding fixtures. The resulting action free of play and stick-slip enables angular adjustments with high precision. Using suitable actuators, the pointing can be set with a resolution $< 10 \mu\text{rad}$, equivalent to a displacement of $\approx 30 \mu\text{m}$ of the atomic cloud in the detection area. This ability becomes important, when the effect of Coriolis forces is to be compensated, see section 4.2.

3.1.2. Velocity Selection

1 ms after launching the atoms, the z-component of the compensating magnetic field is ramped up to $120 \mu\text{T}$. This way, a quantization axis parallel to the linearly polarized Raman-beams is defined, which propagate vertically from top to bottom and are back-reflected of a horizontal mirror below the MOT-chamber. A properly aligned $\lambda/4$ -plate in front of the mirror gives a linear polarization of the reflected beams perpendicular to the incident polarization. Restricted by polarization selection rules this lin-lin configuration only drives Raman-transitions stimulated by counter-propagating beams. From the two pairs present a specific set is chosen by tuning the frequency difference to the Doppler-shifted resonance of the atoms moving upwards.

A π -pulse with a Gaussian envelope of width $56 \mu\text{s}$ selectively transfers only atoms with the proper velocity component along the vertical axis to $|F = 1\rangle$ [89], whereafter the remaining atoms in $|F = 2\rangle$ are scattered away by a short pulse of one of the cooling beams. The Fourier-width of the Raman-pulse corresponds to a momentum spread of 1/10th of the recoil momentum of the transferred atoms. This is in fulfilment of the condition for negligible dispersive effects of thick beamsplitters and also improves the achievable fringe contrast. It further ensures that the vertical size of the atomic cloud is virtually constant over the course of a shot, which helps in detection, as clipping effects are avoided.

The frequency-selective Raman-pulse is also a useful tool to quantify the magnetic flux in the MOT-region. The Zeeman-splitting of the atoms can be resolved (figure 3.4) by scanning the difference in frequency of the two beams in a Doppler-insensitive configuration, obtained by switching the beams to circular polarization and blocking the bottom mirror. As

the magnetic sub-levels of both hyperfine levels split by equal but opposite amounts when a certain flux is applied, a net difference of $14 \text{ kHz}/\mu\text{T}$ between adjacent sub-levels is the result. The resolution of this method is sub- μT , as the Raman pulses have a Fourier-width of 2.8 kHz .

Even more useful than scanning is a "real-time" method, where a single pulse (now back in Doppler-sensitive mode) resonant with the mean velocity of the cloud is applied. This selects three classes of atoms, as those in sub-states $m_F \neq 0$ are preserved when their Doppler-shift is compensated by the corresponding Zeeman-shift. The three classes have slightly different velocities, which leads to a spatial splitting at the end of the free-flight parabola. When the atoms pass through a narrow detection beam, an easily resolvable time pattern is observed, where the temporal splitting is proportional to the Zeeman splitting. Overlapping the pulses during detection by adjusting the compensation coils guarantees for good cancellation of background fields.

Another advantage of the second method is the much higher temporal resolution as well as a crude guess of the atom's temperature, which can be gathered from the height of the detection signal. Higher temperatures of the atomic sample mean a higher spread in the velocities and thus a lower signal, as less atoms fulfilled the tight velocity constraints of the Raman pulse. This allows for an in situ examination of the magnetic flux fluctuations in the MOT, which enabled to identify magnetic noise as the main obstacle to lower temperatures. This was deduced from a strong correlation found between fluctuations in residual Zeeman-splitting, signal height and the signal of a pick-up coil.

3.1.3. State Selection

In order to minimize unwanted phase shifts caused by inhomogeneous stray fields in the interferometer zone, the atoms need to be prepared in the magnetically insensitive sub-state $m_F = 0$. Optical pumping would involve multiple scattering of photons, leading to considerable heating of the atoms. A better approach is to discard all atoms in wrong sub-states, which also serves to clean the sample from residual velocity components caused by atoms in sub-states $m_F \neq 0$.

State selection takes place in the central part of the vacuum system, again machined from bulk material. A chamber with 8 windows on its octagonal perimeter in the horizontal plane allows multiple optical access to the atomic cloud in its middle. Two axes (4 windows) are used for detection, while one of the remaining windows serves as a microwave

3. Experiment

port. A coaxial-to-wave-guide-adaptor (Omecon RA-14-PQB-012-B-SMA-F) mounted to the window cap couples ≈ 2 W of microwave radiation resonant with the D_2 -hyperfine splitting into the viewport. The wave travels through the chamber and is reflected back by an aluminium mirror fixed to the opposing side, so that the amplitude of the standing wave at the centre of the chamber can be maximised by adjusting its position. A single microwave π -pulse with a width of $45\ \mu\text{s}$ is preceded by $1\ \text{ms} \times 10\ \text{mW}$ of light resonant with the $(F = 2 \leftrightarrow F' = 3)$ -transition and backed by $5\ \text{ms} \times 1\ \text{mW}$ tuned to $(F = 1 \leftrightarrow F' = 0)$. The light is delivered by a bare fibre and fed through a hole in the back of the microwave coupler, from where it is allowed to diverge into the chamber. With a magnetic flux of $100\ \mu\text{T}$ and suitable orientation of the linearly polarized microwave at the location of the atoms, only those initially in $|F = 1, m_F = 0\rangle$ are left in $|F = 2, m_F = 0\rangle$, while all other atoms gather additional horizontal momentum by the scattered light and get lost.

3.2. Interferometer Sequence

3.2.1. Magnetic Fields

The well defined sample of cold atoms enters then the interferometer zone formed by a 750 mm long titanium tube with a diameter of 40 mm mounted at the top of the vacuum system. A vertical quantization axis is provided by the field of a cylindrical coil wound on an aluminium cylinder covering the whole length of the tube. Two helical groves with opposing direction of rotation, a precise pitch of 3 mm per turn and a diameter of 70 mm were machined on its outer mantle to define the exact position of the windings. This technique gives minimal spatial variations of the magnetic flux while it is possible to suppress the small horizontal component generated by a short coil when interconnecting the two helices with a current going from bottom to top along one of the windings and down along the other. Both, the interferometer tube and the quantization field coil are contained in a custom magnetic shield designed by The Mushield company. It consists of three equally spaced concentric cylinders made from 0.75 mm thick sheets of high-permeability nickel-iron-molybdenum alloy. The innermost cylinder has a length of 675 mm and a diameter of 79 mm while the outermost is 723 mm long and 130 mm wide with the middle and outer cylinder capped to the open diameter of the inner cylinder. For a volume close to its centre the shield provides an attenuation factor of roughly 1000 for magnetic

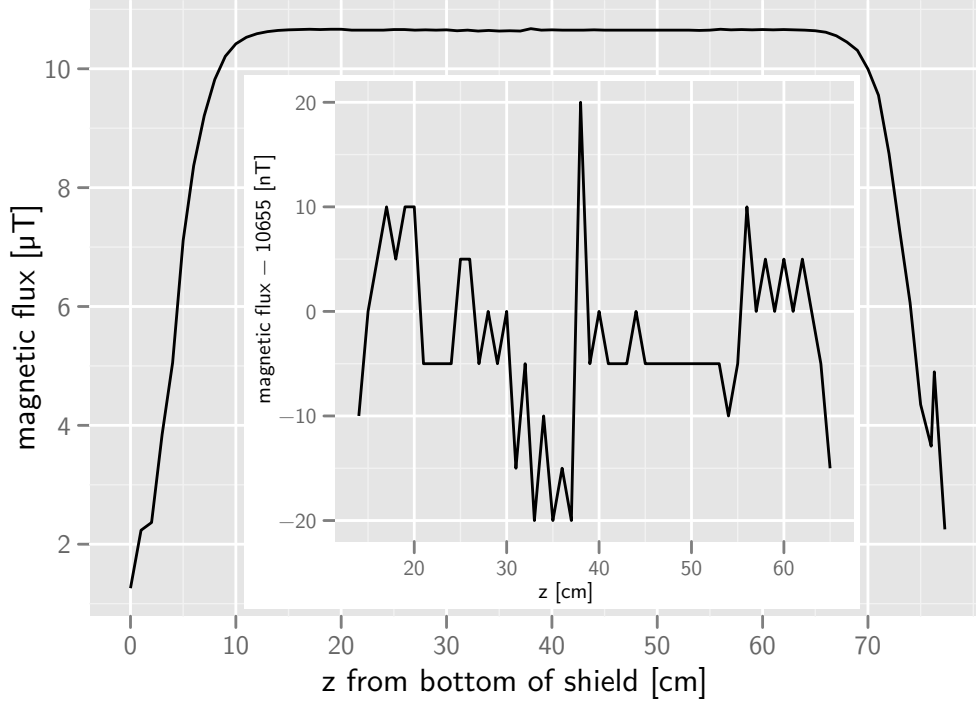


Figure 3.6.: Longitudinal flux of quantization coil at 10 mA measured along the axis inside the magnetic shield. Background fields were rejected through field reversal. The **sub-plot** shows the very good flux homogeneity achieved over the middle range of the coil. Please note the magnified scale; discrete steps are an artefact due to limited resolution of the probe.

influences of frequencies and amplitude common in typical technical environments. This is enough to limit variations in flux to < 40 nT (compare figure 3.7), caused by small residual backgrounds and unavoidable remnant magnetization of the carefully demagnetized shield.

The magnetic environment in the interferometer area needs to be well defined to control systematics arising from Zeeman shifts. While the atoms are prepared in the mostly insensitive state $m_F = 0$, a small dependence on magnetic flux stems from the quadratic Zeeman effect, which causes an additional symmetric shift in the hyperfine splitting of [90]

$$\Delta\nu_{\text{hfs}} = 5.7515 \text{ kHz/mT}^2. \quad (3.2)$$

Typical backgrounds, together with variations in the quantization flux, lead to deviations of at most 100 nT from a perfectly homogeneous bias of $10 \mu\text{T}$. When considering a worst-case-scenario, where only the second

3. Experiment

half of the sequence is affected by the erroneous flux—which geometrically is not possible for the π -pulse close to the apex—this would give rise to a phase shift of

$$\Delta\phi_{\text{quad}} \approx \Delta\nu_{\text{hfs}} 10 \text{ } \mu\text{T} 100 \text{ nT } 0.25 \text{ s} = 1.4 \text{ mrad.} \quad (3.3)$$

Because both paths are always close together with respect to the length scale of flux variations and because the interferometer is almost symmetric to the apex, the real phase shift is much lower and thus negligible.

As a quadratic dependence on the bias flux can be expected for the strength of errors caused by irregularities of the coil, it might be that much higher settings are connected to measurable shifts in the interferometer phase. Such higher flux would be necessary to completely separate atoms in sub-states other than $m_F = 0$ in the frequency domain, when rectangular Raman pulses with typical lengths of 25 ms for $\pi/2$ are used. With the comparatively low setting at hand, undesirable mixing between adjacent sub-states is the consequence e.g. for not perfectly linear polarizations of the Raman beams. Careful state-selection of the atoms is therefore a prerequisite for accurate measurements.

In order to avoid edge effects of the quantization coil and of residual fields leaking through the apertures of the shield, the interferometer sequence should be limited to the length of the vacuum tube reduced by 150 mm at each end. This gives a vertical space of 450 mm equivalent to a free fall time of 600 ms. The largest temporal separation T of the interferometer pulses is therefore 275 ms, if a minimal distance from the apex of 15 ms is chosen to ensure unambiguous addressing through adequate Doppler-shifting. The rather long tube makes it also possible to use shorter T and stack two simultaneous interferometers on top of each other by "juggling" the cold clouds [47], which should enable measurements of the Gravity gradient.

3.2.2. Raman Beams

The light for the Raman beams is delivered by a polarization maintaining fibre with both frequencies ω_1, ω_2 sharing the same linear polarization. A beam-expander (60FC-T-4-M200-37 by Schäfter+Kirchhoff) is used, where the light is allowed to expand freely after leaving the fibre and is collimated by an achromatic lens to an $1/e^2$ -diameter of 29.5 mm, when using a fibre with a numerical aperture $\text{NA}(5\%) = 0.09$. The lens is

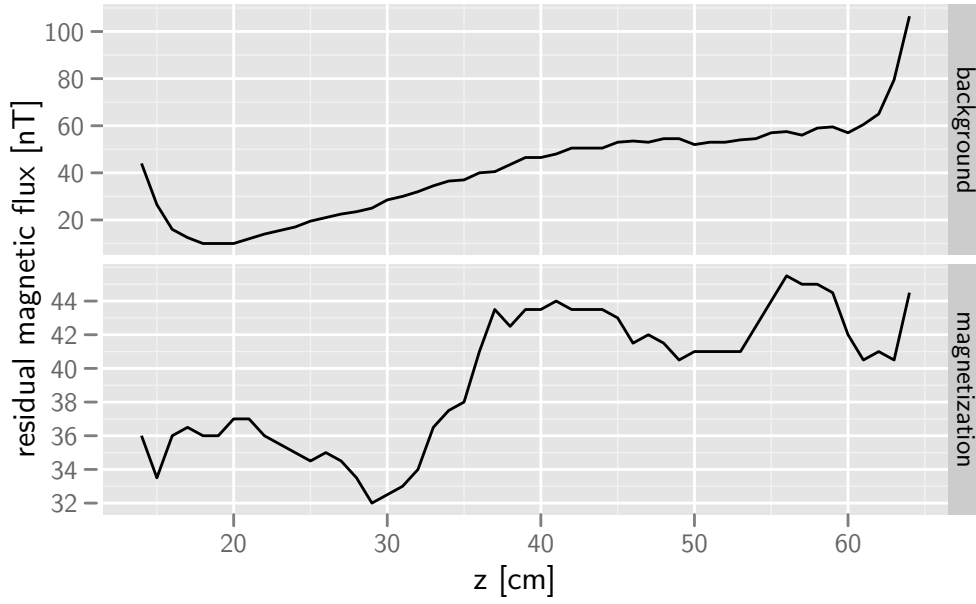


Figure 3.7.: Small flux in the magnetic shield due to remnant magnetization and residuals of typical background fields in a technical environment. Measured with a fluxmeter and separated through flipping the shield.

designed to give a wavefront aberration of $\lambda/20$ over the aforementioned aperture, while the beam diameter is chosen to minimize stray light and wavefront perturbations caused by the beam clipping at various openings of minimal $\varnothing = 40$ mm in the vertical beam-path through the apparatus.

The collimated beam enters and leaves the vacuum-system through 50 mm diameter optical flats with an antireflection coating specified to better than 0.25 % at 780 nm, parallelism better than $1'$ and wavefront aberration better than $\lambda/20$. The windows are mounted in soft indium seals and are 15 mm thick in order to minimize beam perturbations caused by stress or bending.

Below the lower window a $\lambda/4$ -plate (Laser Components, QWP0-780-20-4, zero order, flat to $\lambda/10$, 10-5 scratch-dig) is mounted in front of a vibration-isolated high-quality mirror (BFI Optilas, $\lambda/20$, 10-5 scratch-dig), from where the beam is reflected back to the beam-expander. An additional $\lambda/4$ -plate, which can be shifted into the optical path between beam-expander and upper window, will lead to a $\sigma^+-\sigma^+$ configuration for a pair of co-propagating beams. These can be used to drive Doppler insensitive Raman transitions when the back-reflected beams are blocked.

3. Experiment

The Raman beams have a power of 40 mW each, which gives pulse lengths of 22 μs ($\pi/2$) and 44 μs for the rectangular envelope required by theory. As the velocity-selective pulse was set to be of Gaussian shape with $\sigma = 56 \mu\text{s}$ (intensity), the remaining Doppler spread of the atoms is well within the Fourier width of the Raman pulses, ensuring that all atoms are equally addressed during the interferometer.

Wavefront Aberrations

The optics involved were chosen to give minimal deviation from perfect plane waves for the Raman beams, but the small perturbations still present need some consideration nonetheless. With wavefront radii large enough to neglect the effect of beam propagation over the dimensions of the experiment, the phase errors induced by co-propagating beams will be the same and thus cancel. In the case of counter-propagating beams this holds only for wavefront errors caused by optical elements present in both beams. Those due to the lower window, the lower quarterplate and the mirror, which are traversed only by the retro-reflected beam, are discussed here.

The simplest form of wavefront aberrations are curvatures over the full aperture, centred on the optical axis, and are considered here, as the treatment is straight-forward. The maximal error for the optical elements used in the Raman beams is specified to be less than $\delta = \lambda/20$, which is equivalent to radii of up to some 1000 m for the given beam diameter. The phase difference imprinted into the atom by two counter-propagating beams with curved wavefronts is equivalent to that caused by only one beam carrying the difference in curvature, quantified by δ_0 at a radius w_0 (compare figure 3.8). As the beam is reflected back by a mirror, the errors due to any optical element traversed twice will count doubly, thus giving

$$\delta_0 \approx 2 \sum_{\alpha} \delta_{\alpha} + \delta_{\text{mirror}}, \quad (3.4)$$

where δ_{α} of each optical element has a sign depending on the orientation (up or down) of its induced curvature for a beam passing through it in a fixed direction. In the situation at hand with two elements (lower window and retarder plate) plus the mirror, cancelling can not be expected, thus errors significantly larger than that of a single element are to be considered.

For $\delta_0 \ll R$ the spherical wavefront can be approximated by a paraboloid and the deviation at a certain distance w from the optical axis can be

written as

$$\delta \approx \left(\frac{w}{w_0}\right)^2 \delta_0. \quad (3.5)$$

When following a single atom through the interferometer sequence and omitting the small splitting of the trajectories, the additional phase shift due to wavefront curvature can be expressed as

$$\Delta\phi_{\text{wfc}} = \frac{2\pi}{\lambda} \delta_0 \left(\left(\frac{w(t_1)}{w_0}\right)^2 - 2 \left(\frac{w(t_2)}{w_0}\right)^2 + \left(\frac{w(t_3)}{w_0}\right)^2 \right). \quad (3.6)$$

Noting that a cut through a paraboloid of revolution in a plane parallel to the central axis will give an intersection congruent with the revolved parabola maps the two-dimensional case to a one-dimensional problem. With the t_i being equally spaced by T and the movement of the atom in a plane perpendicular to the z -axis being given by a constant velocity v_{lat} , the expression from above reduces to

$$\Delta\phi_{\text{wfc}} = 2\pi \frac{\delta_0}{\lambda} \frac{2(v_{\text{lat}}T)^2}{w_0^2}, \quad (3.7)$$

which is remarkable for the fact that the phase shift an atom experiences is independent of its initial position.

For laser cooled atoms the distribution of their horizontal velocities is fixed by the temperature of the cloud after optical molasses. To estimate the effect of wavefront curvature on gravity measurements, the contribution of all atoms detected after the interferometer sequence is to be averaged. In a simple model the atoms are thought to start from Gaussian distributed points in a disc centred on the optical axis after the cooling beams have been shut off. After time \hat{T} , during which their horizontal movement is unaffected by the Raman pulses, the atoms are interrogated by fluorescence detection in a circular area of suitably chosen radius D .

The averaged phase shift is most conveniently expressed as a complex amplitude factor. Due to the axial symmetry the integrals over starting points and velocities can be reduced to 1D-integrals, which gives

$$A_{\text{wfc}} = \frac{\int_0^\infty \int_0^\infty \gamma(r, v) \rho(r, v) \exp \left[i 2\pi \frac{\delta_0}{\lambda} \frac{2(vT)^2}{w_0^2} \right] dv dr}{\int_0^\infty \int_0^\infty \gamma(r, v) \rho(r, v) dv dr} \quad (3.8)$$

3. Experiment

where

$$\rho(r, v) = \exp \left[-\frac{1}{2} \left(\frac{r}{r_0} \right)^2 \right] r \exp \left[-\frac{1}{2} \left(\frac{v}{v_0} \right)^2 \right] v. \quad (3.9)$$

To reflect that not all atoms with velocity v originating in a point with distance r from the axis will be within the detection area at $t = \hat{T}$ an angle γ is introduced (compare figure 3.8) as

$$\gamma(r, v) := \begin{cases} 0 & \text{if } |r - v\hat{T}| > D \\ 2\pi & \text{if } r + v\hat{T} < D \\ \arccos \left(\frac{(v\hat{T})^2 + r^2 - D^2}{2v\hat{T}r} \right) & \text{else.} \end{cases} \quad (3.10)$$

For $r_0 = 2.5$ mm, $\hat{T} = 0.7$ s and $\delta_0 = \pi/10$, numerical integration gives the result depicted in figure 3.9, where the averaged phase shift is shown as a function of the radius of the detection area for various temperatures of the cloud. With D presently being approximately 4 mm the accumulated phase shift would be about 11 mrad, which is equivalent to 1×10^{-9} in g and thus too high for the targeted accuracy. As the overall phase grows almost linearly with the small wavefront deviations at hand, the situation can be expected to deteriorate significantly when possible local curvatures several times as high are considered.

It should be noted that the error does not vanish if the detection radius is reduced to zero. This might be puzzling at first glance but is understandable when looking at atoms which enter the detection area from outside its diameter with finite velocities. Other techniques to reduce the phase error would be to lower the temperature, to shrink the initial diameter of the cloud or to minimize the time between Raman pulses or between launch and detection. All these solutions would necessitate large modifications of the apparatus—e. g. to reach significantly lower atomic velocities far more involved cooling techniques like Raman sideband cooling [91] are needed—or would have a negative impact on interferometer performance—as e. g. cold collisions induced by high atomic densities. Mapping of and correcting for phase deviations of the Raman beams will therefore be a necessary step in order to reach highest accuracy.

The simple model sketched above does not account for wavefront distortions other than small uniform curvatures. In practice there are various other perturbations to be dealt with, where those caused by small scatterers seem especially cumbersome. Dust particles do inevitably find their

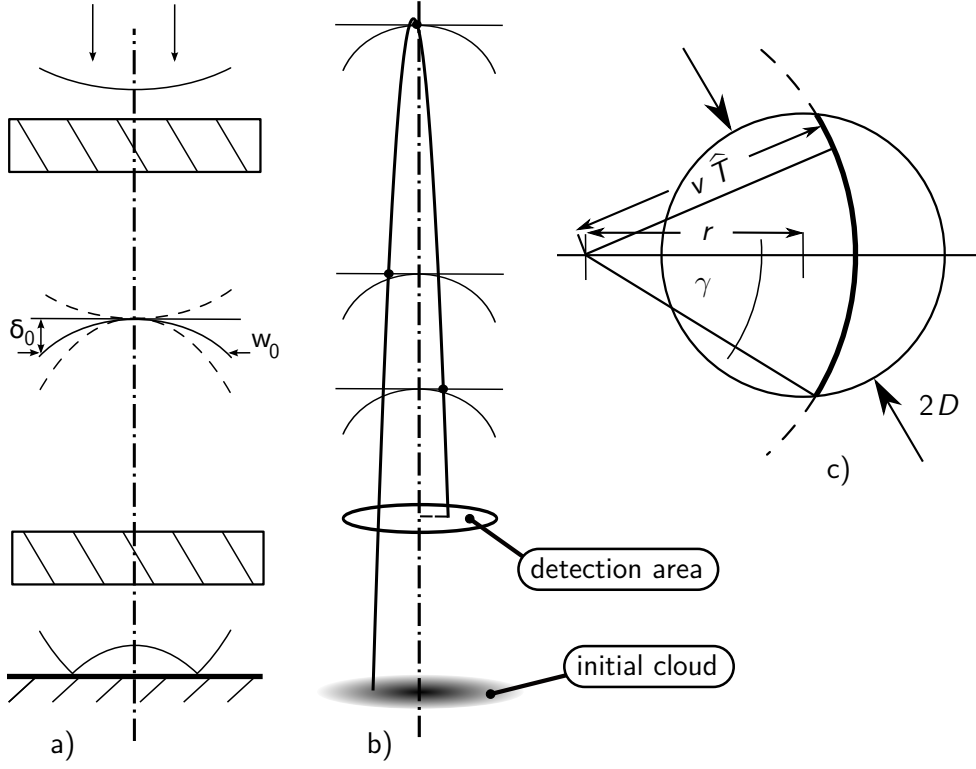


Figure 3.8.: **a)** The difference of two wavefronts curved due to imperfect optical elements can equivalently be expressed by a single curved front. **b)** Atoms sample the curvature at three points equidistant in the horizontal plane. **c)** Look at detection area from above showing the integration variables.

way onto optical surfaces, leading to complicated fringe patterns (compare [48]). It is shown in the cited reference that interference formed by many of these scatterers (speckle) will not lead to observable phase shifts in the interferometer. This might be interpreted as the effect of averaging over a large set of random fluctuations experienced by the atoms moving in and out of zones with positive or negative phase lag between Raman pulses, which results in a mean departing little from the unperturbed value.

It is therefore the effect of only a few scatterers which is most concerning. As developed in [61] the perturbation caused by a small diffusive scatterer in one of the Raman-beams can be estimated as an Airy pattern spreading spherically from the scatterer's position, which is superimposed onto the the beam. The shift experienced by an atom in the central Airy disk during

3. Experiment

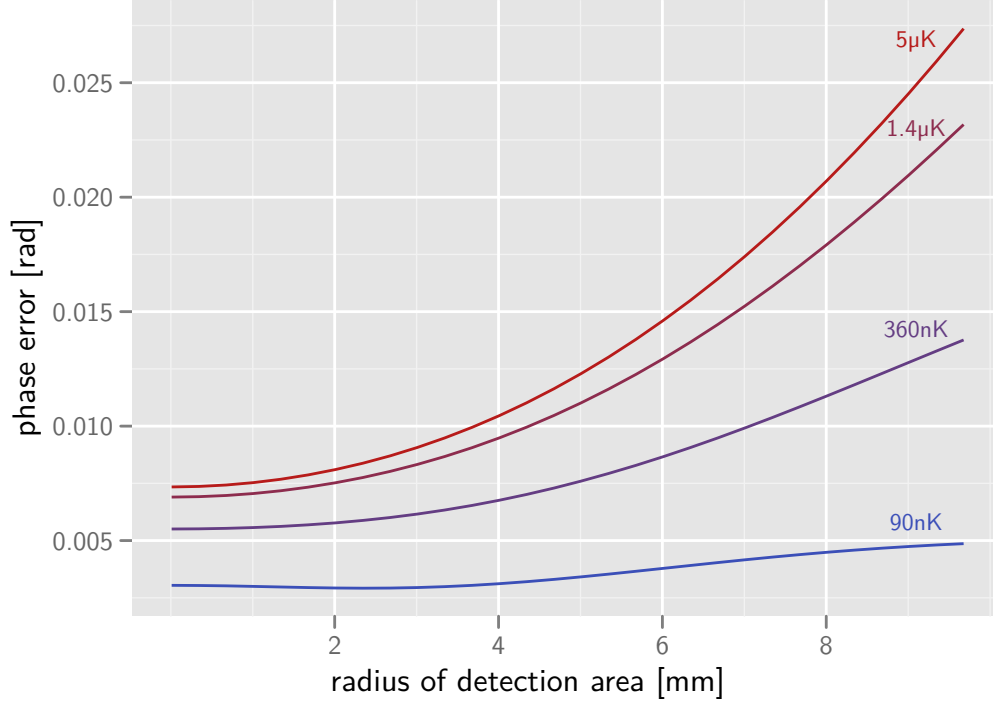


Figure 3.9.: Averaged interferometer phase shift due to wavefront curvature of the Raman beams. The temperatures shown are equivalent to velocities v_0 of the atoms of 1/2, 1, 2 and 3.7 times the recoil velocity of 5.9 mm/s.

a Raman pulse is then given by

$$\Delta\phi_{\text{scat}} = \frac{a^2(\Delta x)^2}{2\lambda d_s^2} k_{\text{eff}} \quad (3.11)$$

where $a \ll w_0$ is the radius of the particle, d_s its longitudinal distance from the atom and Δx the lateral offset of the atom from the optical axis, for a particle centred in the beam. For an estimate of the interferometer phase shift it is sufficient to consider only a scatterer on the top window disturbing the downward pointing Raman beam, as the effect drops off with the square of the distance between particle and atom.

The problem is treated similarly to that of uniform curvatures. To account for a scatterer off the optical axis, the averaging integral needs to be swept over the angles β and γ (compare figure 3.10), then reading

$$A_{\text{scat}} = \frac{\int_0^\infty \int_0^\infty \int_0^{2\pi} \int_{-\gamma(r,v)}^{\gamma(r,v)} \rho(r,v) \exp[i\Delta\hat{\phi}_{\text{scat}}] d\gamma d\beta dv dr}{\int_0^\infty \int_0^\infty 2\pi\gamma(r,v)\rho(r,v)dv dr}. \quad (3.12)$$

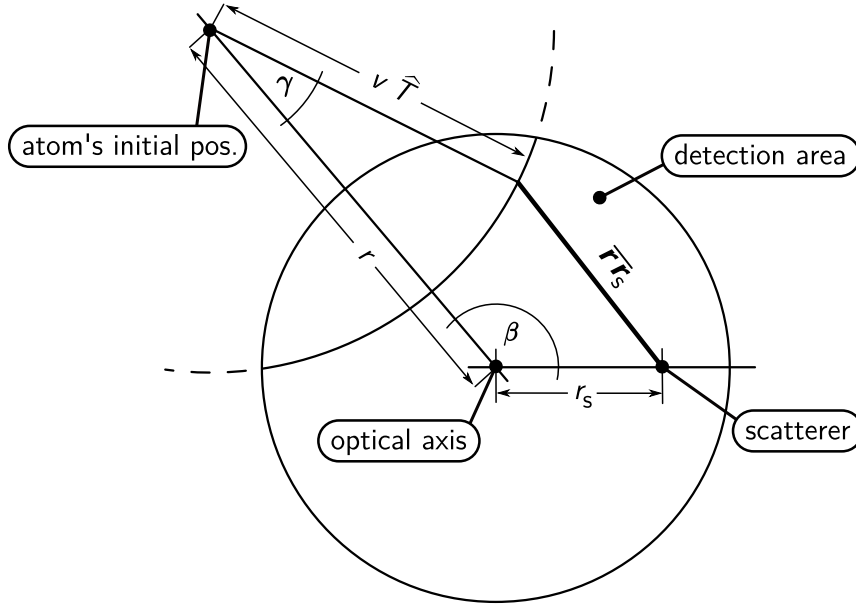


Figure 3.10.: Top view of detection area showing the integration variables used in the estimation of the effect of a single scatterer in the Raman beam.

where the phase perturbation is due to three light pulses (splitting of the paths is again neglected)

$$\Delta\hat{\phi}_{\text{scat}} = \Delta\phi_{\text{scat}}(t_1) - 2\Delta\phi_{\text{scat}}(t_2) + \Delta\phi_{\text{scat}}(t_3). \quad (3.13)$$

A slight modification to the phase-factor is necessary to reflect the position of atom and scatterer, where the latter is r_s apart from the optical axis

$$\Delta\phi_{\text{scat}} = \exp \left[-\frac{1}{4} \frac{r_s^2 - r^2}{r_{\text{beam}}^2} \right] \frac{a^2 \mathbf{r} \mathbf{r}_s^{-2}}{2\lambda d_s^2} k_{\text{eff}}. \quad (3.14)$$

The exponential entering the phase gives the amplitude-ratio of the light at the positions of scatterer and atom, which together with a factor $a^2/(d_s\lambda)$ determines the relative strength of the Airy pattern compared to the Raman beam. Numerical evaluation for a particle with $a = 20 \mu\text{m}$ and the π -pulse situated 15 cm from the top window then gives the result depicted in figure 3.11. For a scatterer on the optical axis the phase shift is acceptable, but grows to cumbersome levels with the particle moving outwards due to the comparatively strong curvature of the perturbation. Shifting the fountain away from the window strongly lessens the error due to the sensitive dependence of $\Delta\phi_{\text{scat}}$ on d_s , but this effect is compensated quickly

3. Experiment

by growing the scatterer. Dust particles with a radius larger than $100\text{ }\mu\text{m}$ are not uncommon—especially under field conditions—which would give rise to impermissible errors in gravimetric measurements. Therefore considerable effort has been made to encapsulate all elements of the optical path the Raman-beams take after leaving the fibre.

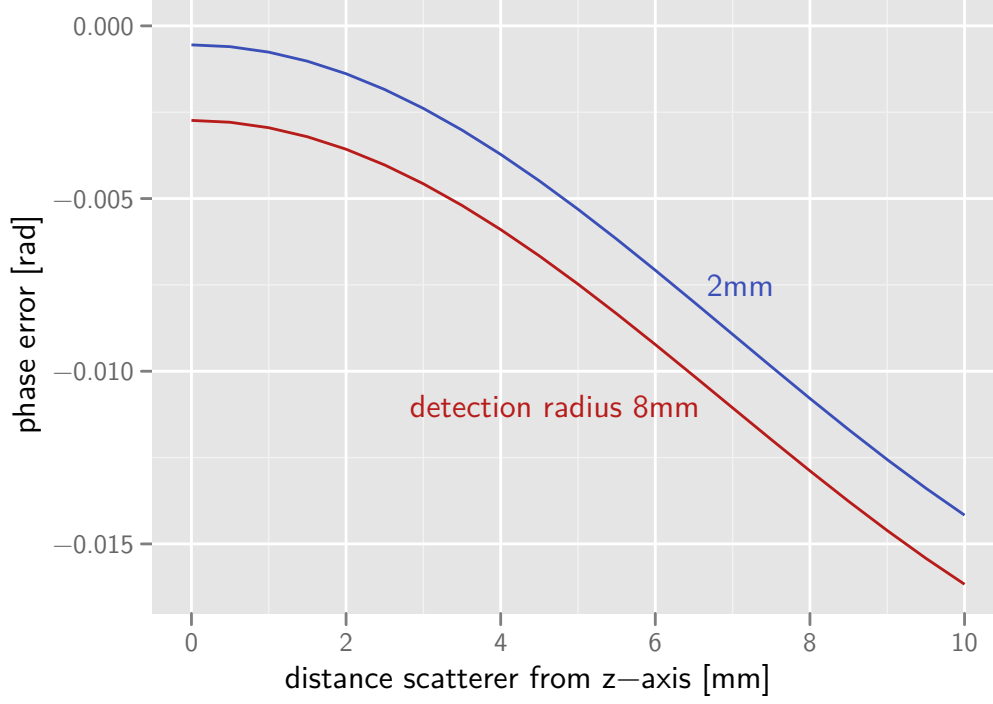


Figure 3.11.: Interferometer phase shift experienced by an atom due to a small scatterer on top window perturbing the Raman beams. While the radius of the detection area does have a small influence, variation of temperature is of negligible effect.

Gouy Phase

Two points on the optical axis far away from and on opposite sides of the waist along a Gaussian beam show a phase difference of π additional to the phase accrued due to beam propagation. In terms of the Rayleigh range it can be expressed as

$$\zeta(z) = \arctan\left(\frac{z}{z_0}\right). \quad (3.15)$$

3.2. Interferometer Sequence

For the Raman beams originating in the same beam expander and one being reflected from a mirror, the atoms see a phase shift which can be expressed in terms of the Gouy phase of the unreflected beam alone

$$g(z, \Delta z) = \zeta(z) - \zeta(z + \Delta z). \quad (3.16)$$

Here Δz is two times the distance between atoms and mirror if both beams are assumed to share the same focal plane. The net effect due to the Gouy phase is then

$$\Delta\phi_{\text{Gouy}} = g(z_1, \Delta z_1) - 2g(z_2, \Delta z_2) + g(z_3, \Delta z_3). \quad (3.17)$$

The Rayleigh range of the Raman beams is 900 m and other typical experimental parameters are $\Delta z_1 = 1.528$ m, $\Delta z_2 = 1.988$ m and $\Delta z_3 = 1.39$ m for which (3.17) evaluates to 1.76 mrad at $z = 0$ close to the extremum. This indicates that the Gouy phase is only of minor concern in order to reach the targeted accuracy.

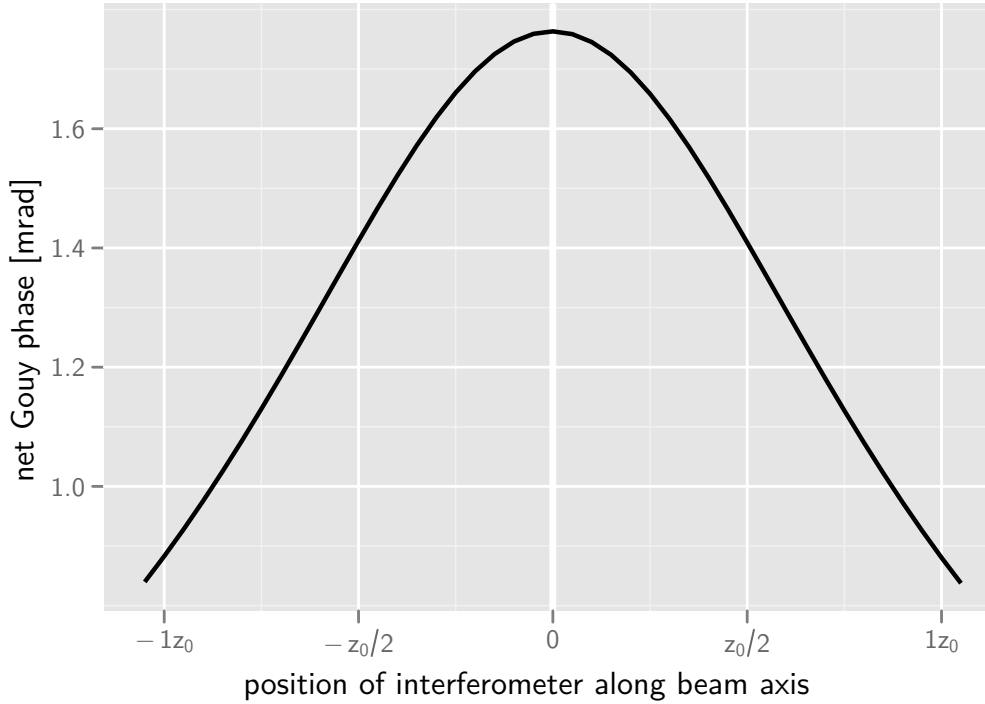


Figure 3.12.: Error caused by the Gouy phase as a function of the position of the π -pulse with respect to the waist of the downward pointing Raman beam.

3. Experiment

Beam Alignment

The direction in which the interferometer is sensitive to accelerations is given by the wave vectors of the Raman beams. For small deviations θ from perfectly parallel alignment, the interferometer phase can be written as

$$\Delta\phi = \mathbf{g} \cdot \mathbf{k}_{\text{eff}} T^2 = g k_{\text{eff}} T^2 \cos \theta \approx g k_{\text{eff}} T^2 (1 - \theta^2). \quad (3.18)$$

It is easy to see, that in order to achieve an accuracy $\Delta g/g$ of 10^{-10} , θ must be less than $10 \mu\text{rad}$. Up to a factor of two the same holds for parallel alignment of the retro-reflected beam with the incident one.

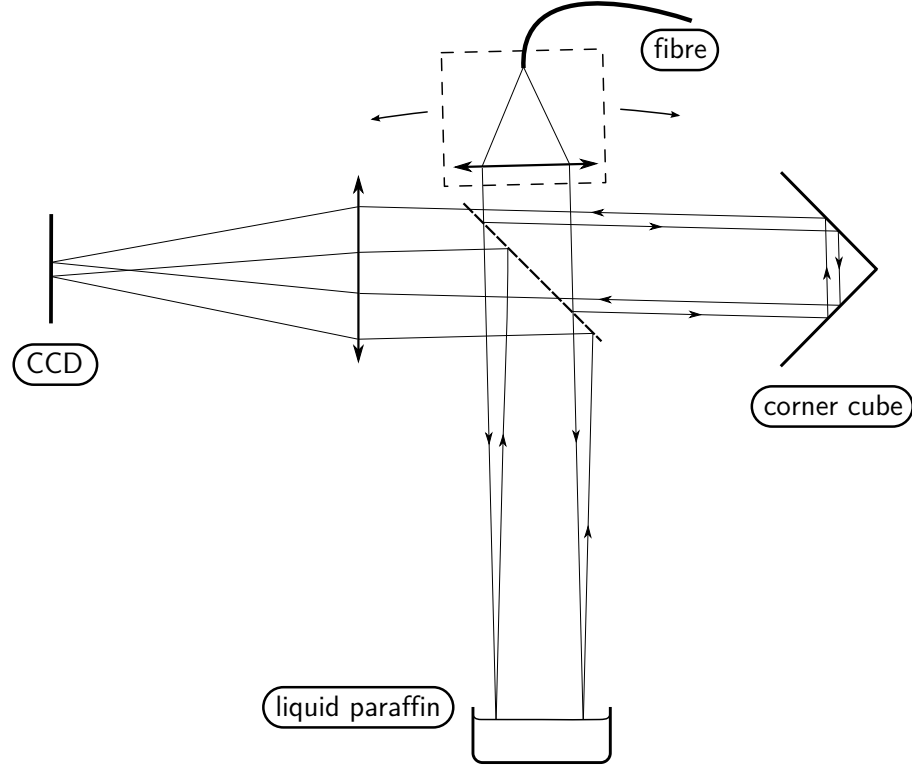


Figure 3.13.: Principle of the procedure used to align the Raman beams vertical and parallel. By overlapping the foci on the CCD-chip through tilting of the beam-expander, verticality is achieved. For clarity, not all beams are drawn.

To ensure proper orientation of the beams a beamsplitter can be inserted between Raman beam expander and vacuum system to make use of a dedicated alignment tool permanently fixed to the set-up. 50 % of the incident light is directed onto a hollow corner cube, which reflects the light

back onto the beamsplitter under an angle specified to be less than $5\text{ }\mu\text{rad}$. The two sides of the beamsplitter are specified to be parallel better than $10\text{ }\mu\text{rad}$, deflecting the light passing through it by less than $5\text{ }\mu\text{rad}$ ¹. A plano-convex lens with a focal length of 200 mm is used to focus the light onto a CCD-chip, salvaged from a simple webcam. The excellent quality of the wavefronts allows for a focal waist close to the Rayleigh-limit of $2.5\text{ }\mu\text{m}$, which about matches the pixel size of the chip. This configuration provides an easy way to control the alignment of the beam down to approximately $20\text{ }\mu\text{rad}$ from the picture taken by the camera.

A cup filled with liquid paraffin replacing the mirror on top of the vibration isolation stage below the vacuum system acts as a horizontal reference. The low viscosity of the fluid along with the reduced effect of vibrations allows to locate the focus of the light reflected from its surface and directed onto the CCD-chip by the beamsplitter to about a pixel. Making the focal points of both beams coincide thus guarantees good vertical alignment of the Raman beam. Putting the mirror back in its place and adjusting its tilt as to overlap the foci again results in both Raman beams being parallel within the requirements.

The procedure is limited by the wedge of the lower vacuum window of less than $1'$ which gives an upper bound on verticality of about $150\text{ }\mu\text{rad}$. This is clearly insufficient to achieve the desired accuracy, but provides a good starting point to optimize vertical adjustment. Tilting the pair of Raman beams will result in the measured value of g being a parabolic function of the tilt angle, which allows to identify the correct setting [48].

A tilt sensor (Applied Geomechanics, 756-1129) fixed to the mirror from beneath allows for continuous monitoring of both tilt axes with $1\text{ }\mu\text{rad}$ precision and thus for corrections of the variations caused by the somewhat wobbly vibration isolation. The rigid fixture holding the Raman beam expander and attached parts on top of the experiment (compare figure 3.19) was designed to provide a stiff base immune to deflection and vibrations. Plates of wooden laminate material were used to further promote stability and to minimize ringing, which is a problem with all-metal structures. Regular inspection of the Raman optics showed no significant tilt for the upper optics within the limits of the alignment tool over the course of multi-day measurement campaigns.

¹For an optical flat with a small wedge made from most common materials, the deflection angle can be estimated to be roughly half of the wedge angle.

3. Experiment

3.3. Detection

The outputs of the interferometer are read out when the atoms fall back into the central chamber (compare figure 3.1). For this purpose a simple fluorescence scheme is implemented, where the two hyperfine states are successively addressed by resonant laser light and a fraction of the scattered photons are collected onto a photomultiplier tube. From the ratio of the integrated signals the interferometer phase can then be obtained.

3.3.1. Optics

The detection light is delivered through a fibre from where it passes a quarter-wave plate and is otherwise allowed to expand freely. An achromatic lens with focal length of 250 mm is used to collimate the beam to a $1/e^2$ -diameter of 50 mm, which gives a large central area with almost uniform intensity in order to minimize spatial dependency of the detection. The actual diameter of the detection beam is set by an iris diaphragm positioned between fibre and lens and a series of baffles after the collimator is used to catch most of the light diffracted at its rims. The beam is then steered through the chamber in a horizontal plane and reflected back by a mirror on the opposite side to balance light forces acting on the atoms.

Light scattered by the cloud is distributed isotropically in all directions for circular polarization of the detection beam. A solid angle of $\approx 4\pi/100$ sr is sampled by two plano-convex lenses mounted back-to-back as close to the vertical axis as possible in a dedicated viewport perpendicular to the ones used to deliver the detection light. The combined focal length is chosen as to image the cloud with unity scale onto a slit mounted in front of a photomultiplier tube (PMT). During measurements, beam diameter and slit aperture are set to select a central volume of $8 \times 8 \times 8$ mm³ of the cloud in order to minimize systematic effects. Attached to the viewport opposing the PMT is a horn-shaped light dump which gives an almost completely dark background. Along with the measures to avoid stray light from the detection beam, this results in a residual signal of the PMT limited by photons scattered from thermal background vapour.

In order to assess the background-signal, which can be as high as the interferometer signal, the detection scheme described in the following paragraph is implemented twice: a first sequence is applied when the atoms returning from the interferometer zone are in front of the PMT, and a

second measurement is taken 20 ms later when all atoms from the initial MOT have left the detection area. Simple subtraction then separates the background from the interferometer signal.

During detection, two pulses of light 400 μs long and red-detuned by 1 MHz to the ($F = 2 \leftrightarrow F' = 3$)-transition are separated by 50 μs of repumper ($F = 1 \leftrightarrow F' = 2$). This pattern subsequently samples the fraction of atoms in $|F = 2\rangle$ and then all atoms as those left in $|F = 1\rangle$ are transferred to the other hyperfine ground state during the middle pulse. The intensity is set to the saturation intensity, which results in the PMT receiving about 60 photons from each atom in resonance. Even for low quantum efficiencies it is thus ensured that determination of the ratio of atoms is not limited by photon statistics. The short pulse-lengths were chosen to prevent optical pumping, which would otherwise result in atoms being transferred to $|F = 1\rangle$ during detection pulses and consequently a bias in the observed ratio of atoms.

3.3.2. Electronics

The PMT is a Hamamatsu R10699 with a specified quantum efficiency of 10 % at 780 nm and an active area of $8 \times 24 \text{ mm}^2$, mounted in a magnetic shield. The attached voltage-divider was modified such that the photocathode can be shortened to the second dynode at the signal of a TTL-pulse in order to prevent saturation effects during MOT-phase with its excessive light levels. The photo current is transduced by a Hamamatsu C7319 pre-amplifier unit with a bandwidth of 200 kHz to voltages of a few volt. This signal is then sampled with 400 kHz and 16 bit resolution over a range of 20 V and stored for further processing.

3.4. Vibration Isolation²

The interferometer is built to measure very precisely the acceleration experienced by the atoms with respect to the mirror beneath the vacuum chamber, as the latter fixes the frame in which the phase of the effective wave vector is to be described. The measured acceleration thus equals local g only if the mirror is resting with respect to the masses which

²This component of the fountain set-up was developed together with Christian Freier and is part of his diploma thesis [92]. Much of the benefit drawn from the vibration isolation is due to his excellent work.

3. Experiment

are the cause of said gravity³. An important source of erroneous movements of the mirror are vibrations of the supporting floor—mostly due to technical noise abundantly present in human environments, but also of natural origin in the form of microseisms caused by ocean waves and wind.

The relevant spectrum ranges from roughly 30 mHz given by the lower end of predominant frequencies found in wave patterns and goes up to a about 10 Hz defined by the finite bandwidth of the interferometer's sensitivity (compare figure 2.4). Accelerations in this frequency band are readily measured with high precision by commercially available seismometers and can in principle be removed retrospectively from gravity data [93, 94]. However, it was found to be more reliable and efficient to reject acceleration noise during measurements. This is done by placing the mirror on top of a vibrationally isolated stage formed by a passive spring system enhanced with an active feedback loop to lower its eigenfrequency. A similar system was employed in an earlier gravimeter and proved to be a key component to reach competitive performance [95].

Common vibration isolation systems are based on the observation that a mass coupled elastically through a spring to a moving foundation will follow the motion with progressively lower amplitude for frequencies higher than the (highest) eigenfrequency of the oscillatory system formed by spring and mass. The simple example of a mirror suspended from a tension spring could in principle be applied to the task at hand. But to reach a sufficiently low eigenfrequency a spring over 250 m long would be needed, which does not agree well with the constraints of a mobile apparatus. Instead, a device had to be designed to fit into the available space of about $40 \times 40 \times 30 \text{ cm}^3$ and be rugged enough for field use.

3.4.1. Mechanics

The foundation of the system is the commercial isolation stage 50BM-10 by MinusK Technology, measuring $30 \times 30 \times 12 \text{ cm}^3$ and weighting about 16 kg. Utilizing a patented mechanism it features a vertical resonance as low as 0.5 Hz for masses of up to 25 kg on top of its platform. In order to

³As Earth itself is a rather wobbly affair if looked at scrupulously, it is hard to tell what exactly the reference should be to which the mirror is to be tied. To the best of the author's knowledge "local gravity" is in practice defined as the effect left over when all known sources of error are removed. This approach in turn seems somewhat flawed by not always fully established conventions of what to count as error; see discussions related to "permanent tide".

be soft enough to give the desired low eigenfrequency while at the same time supporting the isolated mass against gravity in a tight vertical space, the spring system needs to be highly non-linear. The spring constant is low only for deflections in a limited region around equilibrium and grows rapidly with larger displacements. As for accelerations due to typical environmental noise a range of a few millimetres is sufficient, very compact overall dimensions are possible.

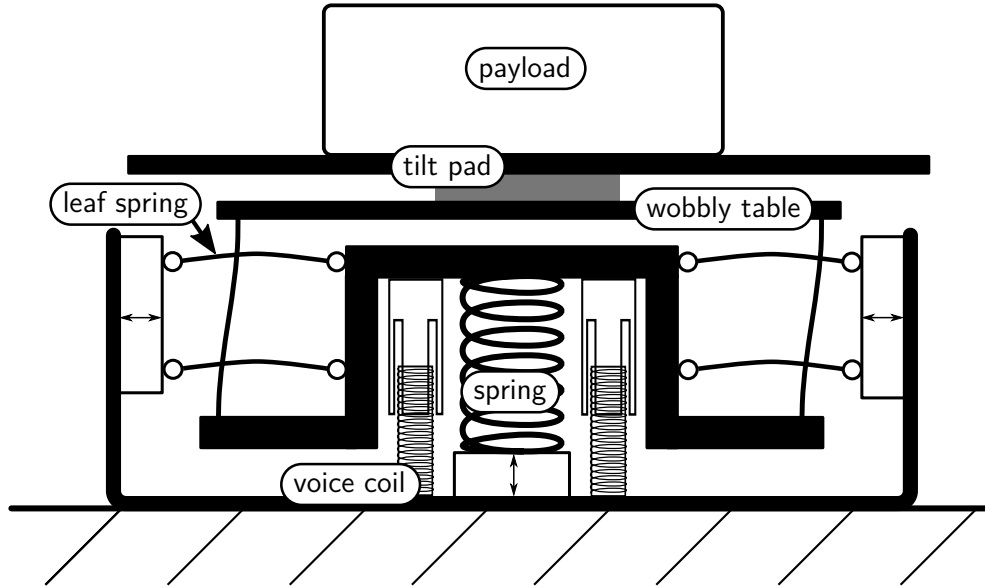


Figure 3.14.: Schematics of the commercial vibration isolation modified for active feedback. By setting the compression stress on the springs, the platform can be adjusted for different payload mass and vertical resonance frequency. Two voice coils were added symmetrically to the central spring as controllable actuators.

The working principle relies on balanced forces generated by a vertical compression spring to countervail gravity and a symmetrical pair of leaf springs mounted horizontally, which put an adjustable compression stress on a joint at the upper end of the vertical coil. For a fully horizontal alignment of the leaf springs their anti-parallel forces cancel, while for small deflections they counteract the force exerted by the compression spring. This happens with an almost linear dependence on departure from equilibrium position, effectively lowering the vertical spring constant.

In figure 3.15, the characteristic curve for several eigenfrequencies is

3. Experiment

given. While with care resonances even lower than 0.4 Hz are achievable, the system exhibits a growing tendency to drift from equilibrium position towards one of the ends of the soft range as the springs react to minute changes of their temperature and creep in the system. This limits the useful interval of settings to above 0.6 Hz if long-term stability is needed. For the isolation platform being part of the active feedback loop an even higher frequency of 0.8 Hz was chosen to diminish hysteresis and other nonlinear effects which otherwise might compromise feedback characteristics. A modest hardening of the spring system for greater elongations was found useful, though, to limit run-away caused by transients.

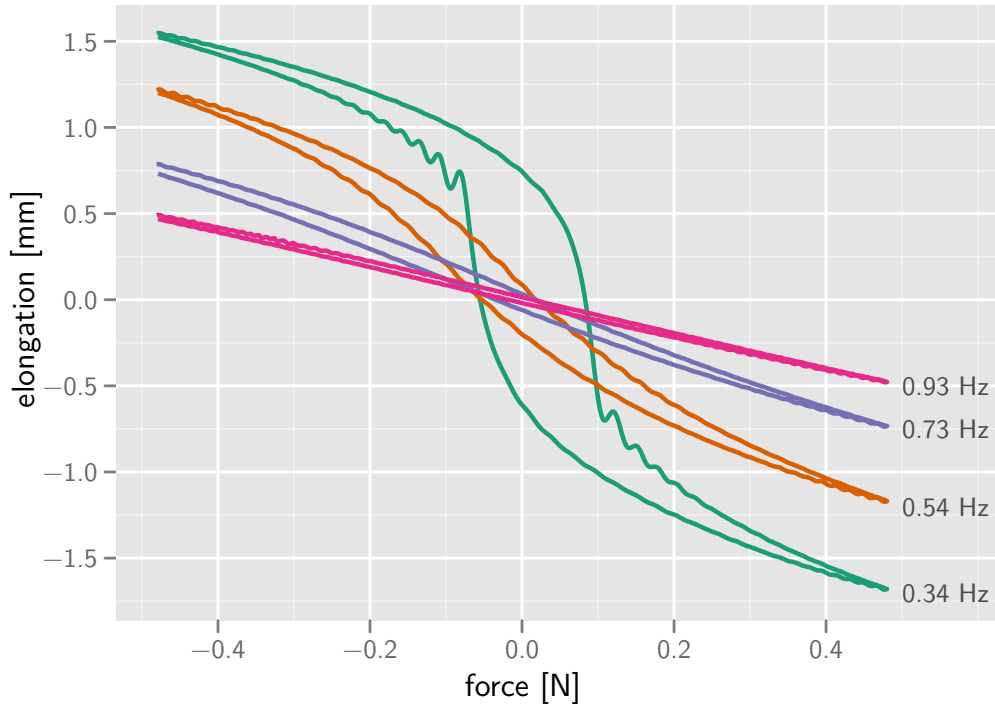


Figure 3.15.: Elongation vs. force exhibited by the negative-stiffness mechanism employed in the vibration isolation. Pronounced hysteresis appears when the system is made softer to obtain lower eigenfrequency. Wiggles in the curves are an artefact caused by the platform "bumping into" the spring becoming swiftly stiffer.

The isolation stage also features suppression of horizontal vibration by means of supporting a rigid plate on top of four thin rods at its corners. This inverted-pendulum configuration—nick-named a "wobbly table"—relies on the restoring force exercised by the rods clamped at both ends

when deflected in the course of the plate departing from its horizontal equilibrium position. Originally the rods were fabricated as to provide a natural frequency of about 1.5 Hz for supported masses close to 25 kg. Upon request the manufacturer provided custom rods which produce a resonance at 0.5 Hz for a similar mass. This helped in alleviating cross coupling effects found to occur at larger horizontal amplitudes excited if the horizontal eigenfrequency of the platform coincided with resonances of the building at 1.7 Hz.

Mounted in between the "wobbly table" and the top plate is a pad of visco-elastic polymer roughly $4 \times 4 \times 1 \text{ cm}^3$ in size. It is promoted as "tilt pad", suggesting that its purpose is the suppression of oscillatory tilt modes. Additionally it was found to be crucial in damping noise due to eigenmodes of the vibration isolation between 10 and 50 Hz which otherwise would badly compromise isolation performance. Albeit the effect on tilt stability—important for the performance of the interferometer—is detrimental, its benefits were found to outweigh its drawbacks. Therefore initial tilt of the top plate has to be nulled by careful positioning of the masses and subsequent creep is to be monitored with a tilt-sensor.

A second effect of the tilt pad is an additional sharp resonance produced at 100 Hz. While direct implications for the interferometer are negligible this is still cumbersome since the connected phase shift limits the feedback gain applicable for frequencies larger than a few Hertz. Until a remedy is found, the effect needs to be incorporated into the model from which a design of the active vibration isolation system is to be derived. Evaluation of the response to oscillations stimulated by the voice coils suggests, that it can be best described as a hysteretically damped oscillator with a transfer function

$$G(\omega) = \omega_0^2 \frac{1 + i \tan(\beta)}{\omega_0^2(1 + i \tan(\beta)) - \omega^2}. \quad (3.19)$$

where the parameter β was derived from fits to be 0.17 rad [92].

To enable active control of the platform, two voice coils (PBA, $\varnothing 16 \text{ mm}$, length when in central position is 31 mm) were mounted between base and upper end of the vertical isolation stage (compare figure 3.14) symmetrically to the compression spring. Their combined force exerted at a maximum coil current of 1.5 A is 6 N, much larger than the 200 mN estimated to compensate for residual accelerations in the frequency band up to 100 Hz acting on a mass of 20 kg. An additional LVDT sensor (Solartron OP6) placed in another corner allows for friction-less monitoring of the vertical displacement with micrometre resolution.

3. Experiment

An integral part of the feedback loop is a Gralp CMG-3VL seismometer customized to provide a flat acceleration response of $2 \text{ kV}/(\text{ms}^2)$ over the range of 0.003–100 Hz on top of the MinusK-platform. The seismometer is a uni-axial sensor with a cross coupling rejection of $> 65 \text{ dB}$ and equivalent self-noise below what is found at the seismologically quietest sites on Earth. Its cylindrical housing made from mild steel measures 101.6 mm in diameter and 208 mm in height. Mounted to its upper end in a tube fitted to a stable kinematic mirror mount is the retro-reflector assembly comprising the mirror with quarter-wave plate and the tilt-sensor, compare figure 3.18.

To prevent cross-coupling of residual horizontal and tilting accelerations into the seismometer signal, careful alignment is necessary. The naive approach would be to place the seismometer exactly vertical in the middle of the platform. But it was found in earlier work [95], that the position of the actual sensor inside the housing is slightly asymmetric. By subjecting the seismometer to tightly controlled angular motions it was confirmed that for this specimen the sensitive axis is indeed centrosymmetric. The seismometer was also tested for sensitivity to horizontal motions, which revealed a disconcerting angle of 18 mrad, by which the device had to be tilted to minimize cross-coupling. Consultation with the manufacturer disclosed the possibility of severe misalignment during assembly, which an improved design of the seismometer is expected to forbid in the future.

3.4.2. Feedback Loop

The bare vibration isolation as bought from MinusK is described well as an under-damped spring-mass system with a natural frequency of here 0.8 Hz. Vibrations of lower frequency will pass through essentially unsuppressed while for higher frequencies the amplitude decreases initially with ω^{-2} and above a frequency depending on the amount of damping (typically $2\pi * 10 \text{ Hz}$) with ω^{-1} . This gives a mean attenuation of only a factor 10 in the important range from 1 to 10 Hz and even an amplification of the vibrations close to resonance. To extend the band over which transmission is decreased—which simultaneously lessens the transmitted amplitude in aforementioned range—an active feedback loop was implemented. The underlying idea is to measure the residual accelerations on the platform and to apply a proportional force counteracting the force of the spring, effectively lowering its spring constant k . This is the feedback control analogue to the negative stiffness technique realized in the MinusK-platform by purely

mechanical means.

In mathematical form this principle is readily expressed as

$$(1 + K)\ddot{z} + 2\gamma\omega_0(\dot{z} - \dot{z}_g) + 2H\omega_0\dot{z} + \omega_0^2(z - z_g) = 0 \quad (3.20)$$

which basically is the well-known differential equation of a harmonic oscillator at position z with viscous damping, where position (z_g) and motion (\dot{z}_g) of the supporting ground with respect to a fixed reference are accounted for. $\omega_0 = k/m$ denotes the unperturbed resonance frequency and γ the damping ratio which is rather small (typically < 0.1) for the MinusK platform. Two terms have been added to reflect the influence of feedback: $K\ddot{z}$ is due to the force $F_a = -mK\ddot{z}$ exerted by the voice coils to counter-act the mechanical spring, and a second term according to a force $F_v = -2m\omega_0H\dot{z}$ needs to be introduced to adjust viscous damping. The latter is necessary as without, the damping ratio of the system in-loop would be $\tilde{\gamma} = \gamma/(1 + K)$, leading to excessively sharp resonances. The new unperturbed eigenfrequency can be expressed as $\tilde{\omega}_0 = \omega_0/\sqrt{1 + K}$, which is exactly the desired result.

For K, H being constants, the feedback-loop would easily be realized with the help of a simple amplifier and an integrator switched between seismometer and a voltage-controlled current source to drive the voice coils. The situation becomes more complicated with the high proportional gain $K \approx 300$ necessary to achieve the targeted reduction in resonance frequency. As signals inevitably suffer from phase shifts caused by the very nature of platform, seismometer and voice coils when passing through the loop, some frequency components will not be attenuated but amplified, since the corresponding feedback is nearly in phase with the perturbation. This leads to unwanted oscillations for certain amplitude conditions, typically when the closed-loop gain is close to or larger than unity. Therefore, to achieve maximum performance, careful design of the feedback parameters is necessary. The goal is to raise the gain maximally over a range as wide as possible, but to keep it low where the phase shift approaches or exceeds $\pm\pi$. This task has been undertaken and described in [92] and yields the result shown in figure 3.16.

The gain becomes a complex-valued function of frequency and substitutes the parameters K and H . The resulting open-loop transfer function shows the combined effect of the seismometer, processing filters to implement the gain function and voice coils together with the response of the mass actuated by the isolation platform. As its phase shift always stays within safe operation limits in the range of frequencies with feed-

3. Experiment

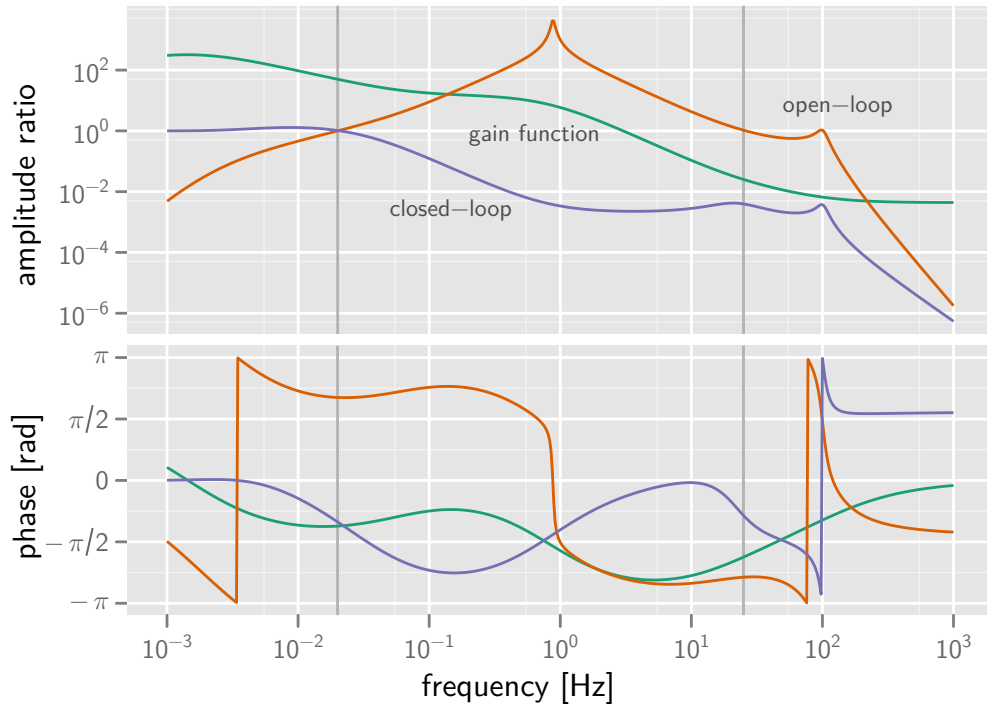


Figure 3.16.: Bode plots of calculated transfer-functions and designed gain of the vibration isolation. In order to prevent positive feedback, the gain needs to be a function of frequency with careful tailored phase response. When the feedback-loop is closed the vibration isolation features a predicted cutoff-frequency of 0.03 Hz.

back gain > 1 (between grey vertical lines) the closed feedback-loop is stable.

3.4.3. Electronics

The found gain function is a series connection of several filters—a high-pass and three lag compensators—which in principle could be executed in analogue circuitry. However, it is much more convenient to implement the functionality in software, which also gives higher flexibility and the possibility to record data for monitoring purposes.

To this end, the seismometer signal is fed to a National Instruments compactRIO-system. It comprises a real-time kernel running on a 400 MHz CPU and a field-programmable gate array (FPGA) backplane. The FPGA module features an AD converter which samples the seismometer signal

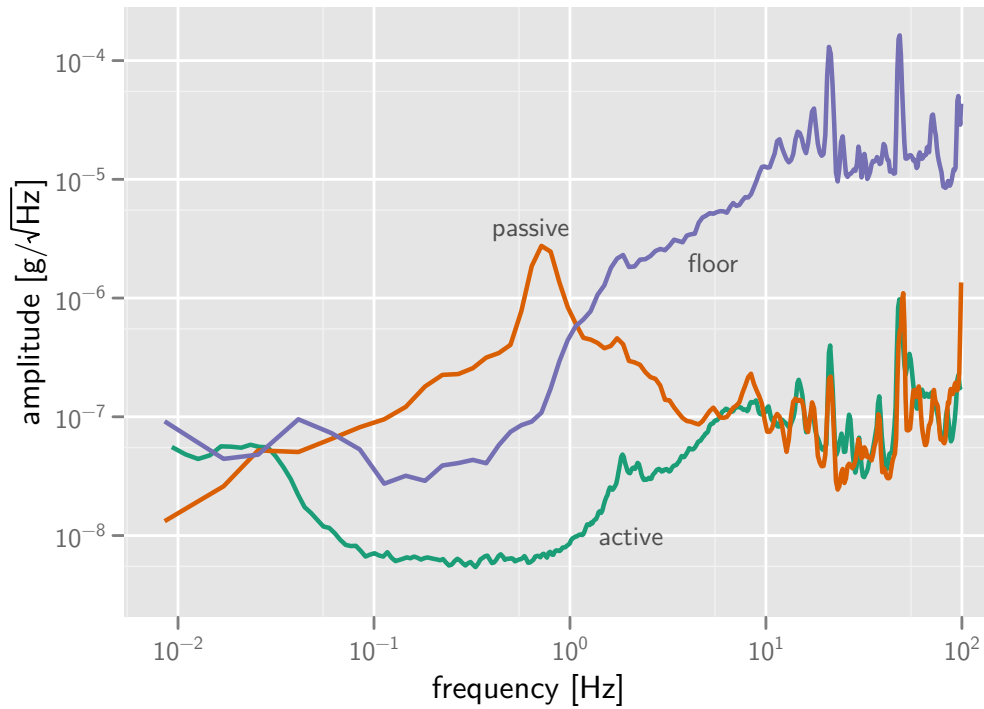


Figure 3.17.: Comparison of the power spectral density of vibrations without attenuation ("floor") and with passive and active isolation stage. Performance of the commercial platform alone is excellent for higher frequencies but suffers from a strong resonance close to 1 Hz which is successfully suppressed by active feedback. Data taken by C. Freier.

with 1 kHz and 24 bit resolution. The obtained data stream is processed by an infinite impulse response filter (IIR) derived from the gain function by means of the bilinear transform and implemented in the FPGA to guarantee stable timing. Feedback of the filter response to the voice coils is done via a 16 bit DA-converter actuating a voltage-controlled current-driver. The IIR-filter is supervised, and can be altered live, by a monitor program running on the real-time system. This part of the software also contains the heuristics necessary for handling switch-on and transients and can even recover from failure e. g. due to external disturbances. The resulting system is self-contained and—once started—fully autonomic to prevent interference from other controlling systems. If desired, however, it is possible to interact with the real-time system via ethernet.

The current driver for the voice coils was designed to give low-noise bipolar output of up to 2 A with a bandwidth of 1 kHz. This is larger than

3. Experiment

the relevant frequency range of the feedback-loop by a factor of 10 and guarantees that phase shifts are negligible, making this device one of the longingly desired "set-and-forget"-type.

Suppression of vertical floor vibrations is documented in figure 3.17. While the passive isolation alone is efficient in reducing accelerations on the platform for frequencies higher than 4 Hz, its narrow resonance produces a cumbersome amplification of vibrations around 0.5 Hz. The active feedback integrated into the system is highly effective in subduing the resulting oscillations and extends the range of attenuated frequencies by two decades down to 0.03 Hz. For frequencies higher than a few Hertz the performance is close to the original systems as feedback gain trails off. It should be noted that the curve for the active vibration isolation was obtained in-loop and thus does not necessarily reflect the actual residual vibrations experienced by the mirror on top of the seismometer. However, corresponding results from gravimetric measurements strongly suggest equivalent reduction in erroneous accelerations, compare sub-section 4.1.1.

3.5. Fountain Set-up and Mobility

During the MOT, as well as the free flight phase, the atoms have to be conserved from collisions with thermal atoms e. g. from background vapour as this is equivalent to a loss of the effected particle. This requires ultra-high vacuum of the order of 10^{-9} hPa or lower, necessitating particular attention during the design of the transportable chamber.

Pumping is achieved by a commercial ion pump (Varian Star Cell, 20 L/s at flange) and a titanium sublimation pump realized in a vertical tube with $\varnothing 70$ mm and a height of 280 mm attached on opposite sides to the central chamber. The latter also acts as kind of a gate-way with the UHV-valve for external access mounted to its upper end. These types were chosen for being vibration-free and—in the case of the sublimation pump—being capable of sustaining the vacuum for at least several days without electrical power. Their combined pumping speed at the central chamber is estimated to 20 l/s when conduction losses are taken into account.

Most parts of the system were made from titanium alloys, which are known for their good vacuum compatibility, excellent mechanical properties, low density and a magnetic permeability close to unity. Together with the choice of other building materials to be aluminium and stainless steel of the variant EN-1.4406, which also feature low magnetic permeability, the

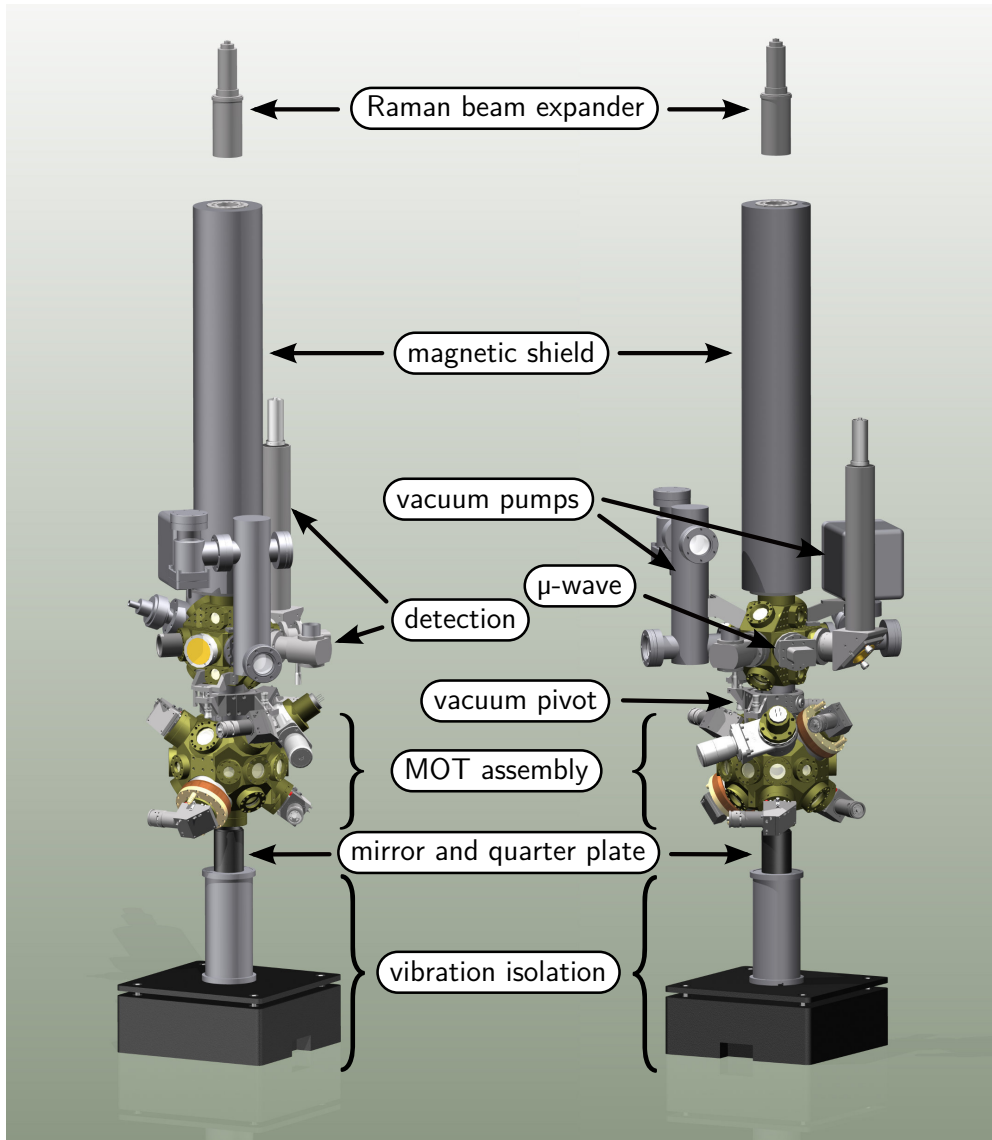


Figure 3.18.: Vacuum system and attached parts necessary to generate an atomic fountain and perform gravimetric measurements. The set-up is shown from two angles. The parts of the experiment which provide laser light and microwave along those needed for controlling are housed in separate trolley frames.

3. Experiment

vacuum system can be considered almost amagnetic, perturbing only minimally any magnetic flux needed to control the atoms.

Welding is cumbersome with titanium due to the high reactivity of the material to oxygen and the resulting embrittlement. It was unavoidable with the tube forming the interferometer zone and needed the attention of a company specialized to this task. With the MOT-chamber and the central chamber this technique could be avoided by milling each from a single block of titanium alloy, which also gives compact outer dimensions. A constraint of the bulk-method is that 3 mm of wall thickness should not be under-run to avoid possible leakage through small voids. These inevitably form during casting in the rods used as starting product.

Of special concern were the many view-ports necessary for optical access to the atoms. Commercial products of the desired optical and magnetic properties are expensive and often rely on soldering the glass piece to a metal sleeve, which can introduce mechanical stress and birefringence. Additionally, the flanges holding the window need to support further equipment fastened to them, which forbids the use of copper-gasket sealed CF-flanges. As the copper yields to the induced stress, leaks might form, which could compromise vacuum to an unacceptable level.

Instead, an approach was used where optical flats are pressed into a soft metal seal sitting in flat recesses machined into the chambers. The window cap holding the glass in place is bolted firmly to the chamber in this process, enabling it to carry high loads. An improved technique—described in appendix B—was developed, with the potential to outperform similar methods in the future. However, due to technical problems and tight schedules, sealing the windows to the chamber with soft indium wires [96] was used instead.

One of the drawbacks with indium is its low melting point of 157 °C, which prohibits high bake-out temperatures and necessitates additional care when cleaning and preparing the vacuum parts. After several weeks of baking at 145 °C the residual pressure could be lowered to a few 10^{-10} hPa. An integrated leak rate of less than 10^{-10} hPa l/s, together with a pumping speed of 20 l/s, ensures that pressure returns to similar levels even after flooding the chamber with Rb-vapour at pressure levels typically ten times as high during multi-day measurement campaigns.

The vacuum system along with the attached optics and auxiliary parts has a mass of ≈ 80 kg. In order to be easily transportable it is mounted on a trolley frame build from aluminium profiles (ITEM Building Kit System) of similar mass running on air-filled heavy-duty wheels. Due to its low centre-of-mass the complete package is handled smoothly by two people

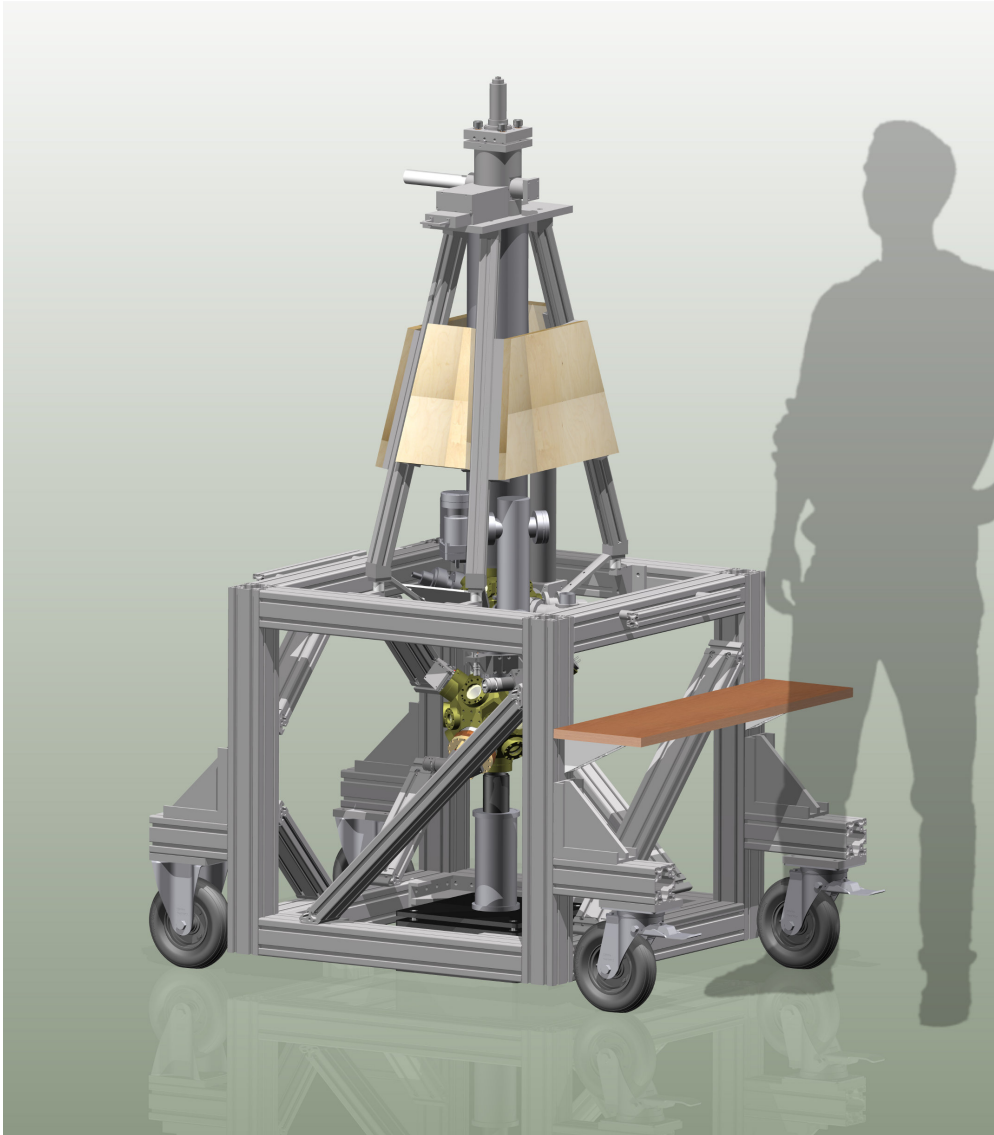


Figure 3.19.: Fountain set-up mounted in a dedicated undercarriage. The vacuum system is supported only at the central chamber close to the centre of mass of the complete package, leaving the MOT assembly free to be tilted to ensure vertical alignment of the atomic fountain.

3. Experiment

under more difficult circumstances and can be moved easily by a single person on hard, level surface.

Validation of mobility was done during moving of the work-group from the city to Adlershof, a campus situated in the outer rims of Berlin. The whole operation went hassle-free and showed the set-up fit for transportation in an ordinary truck with very good stability of vacuum. Deployment at a new site involves only levelling—which is done by propping the trolley on three adjustable feet—and vertical alignment, reconnection of power, signal lines and optical fibres and establishment of the vibration isolation. With some exercise this procedure can be accomplished in a few hours, enabling regular relocation of the apparatus. Future enhancements could even lead to automation of many of these tasks, which would reduce the effort of setting-up to pushing a few buttons.

3.6. Gravity of Fountain Set-up

With the mass of the interferometer apparatus approaching 160 kg, the question of the magnitude of gravity induced by the experiment itself springs to mind. As this systematic effect can hardly be modulated and thus separated from others, it is most useful to calculate the necessary correction. The task at hand is made comparatively easy by the circumstance that almost all parts of the real set-up have their virtual counterpart included in a comprehensive CAD-model (compare figure 3.19) as the result of the design process.

Still, with about 700 parts (not counting a few hundred screws) of roughly 250 different types, manual estimation would be tedious at best. To automate the process, the CAD-assembly was transformed to an AP 214 variant of the STEP-model. STEP is meant to be an abstract representation of all aspects of a product and an open standard promoted by the ISO. AP 214 is a subset especially useful to describe three-dimensional geometries and assemblies thereof. To this end, a product—here the atom interferometer—is represented as a tree with the root node being the complete set-up and subsequent nodes constituting sub-assemblies. Consequently, the leaf nodes are the single parts from which the apparatus is built and are given in the form of a boundary representation (BREP), that is their boundary as a set of simple surfaces and lines. Each branch of the tree not only acts as the connection between its ends, but also gives information of how to position the children by means of rotations and translations with respect to the position of the parent.

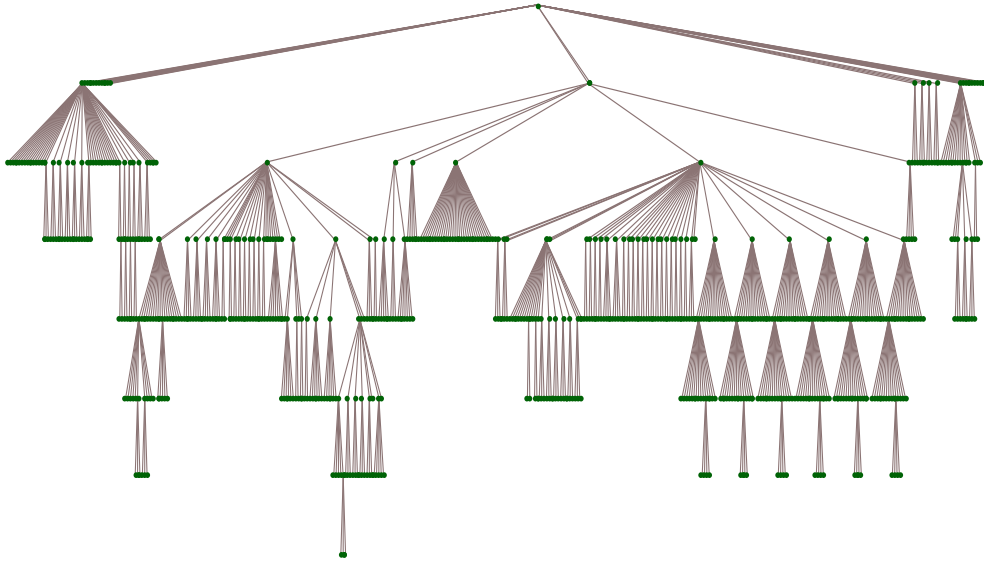


Figure 3.20.: Tree representation of fountain apparatus. Every end-point represents a single part while intermediate nodes stand for sub-assemblies. E. g. the MOT-assembly can be identified in the right half of the diagram by its six-fold symmetry.

A simple parser was written which crawls the tree to first extract a list of unique parts and subsequently builds a database with their material, occurrences and according positions in the 3D-set-up and extracts the BREP to be saved into a separate STEP file. In a subsequent step, the BREP of each part needs to be transformed into a representation suitable for estimating its gravitational effect. A convenient way to do so is to fragment the volume enveloped by the BREP into a set of polyhedra, a technique named mesh generation. As it is widely used in finite element methods, a range of powerful tools is available for this purpose.

The program of choice is gmsh [97] for being open-source, user-friendly, scriptable and potent. While optimal mesh generation in two dimensions is a solved problem, the same does not hold for three-dimensional bodies, making some interaction from the user indispensable. However, it was found that with irregular meshes of tetrahedra generated by the MeshAdapt-algorithm in 2D and extended with the Frontal-algorithm to 3D, only minor tweaks were necessary to perform the task to a satisfactory level in an automated batch-process, for all but a few parts. Mainly some caution is needed with three-dimensional objects having surfaces which feature some kind of singularity, like cones, where—for the purpose of ini-

3. Experiment

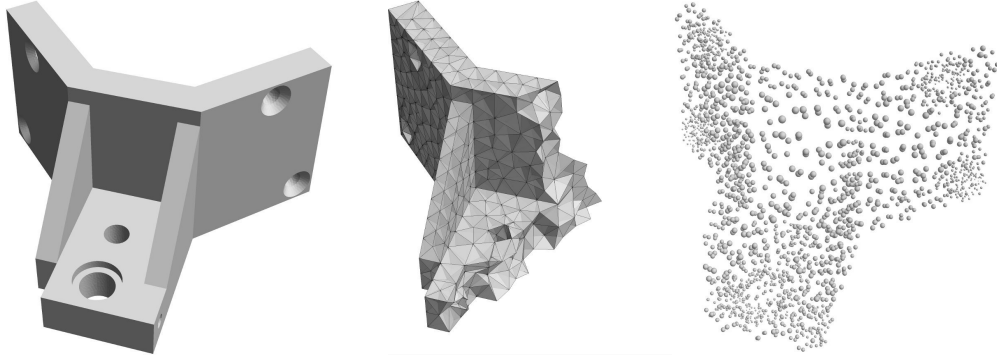


Figure 3.21.: (left) part of the interferometer used for test of mesh quality. The material is aluminium. (middle) mesh build from tetrahedra. (right) representation of the point-masses used for calculation (volume is to scale with the mass). Please note that to enhance clarity, the depicted mesh is chosen coarser than those employed for gravity estimation.

tial 2D-triangulation—the tip cannot be easily mapped to a rectangular parameter space along with the rest of the lateral surface. In such cases the remedy is to alter the CAD-file accordingly.

As each single part from the CAD-model represents a piece made from homogeneous material, its gravity at a given point is simply approximated as the sum of the effects induced by each of its fragments. Here, the deviation of the gravity potential of any tetrahedron from that of the corresponding point-mass needs to be considered as a source of error. For a point far away from the object it can be expected to vanish, but in the situation at hand at least some parts of the fountain apparatus are "close" to the path of the atoms. To get a feeling for the magnitude of the error, the gravity induced by a fairly irregularly shaped piece (see figure 3.21) of the apparatus at a distance of 100 mm, comparable to that of the objects closest to the atoms (not including the vacuum tube and enclosing cylindrical parts), was evaluated for different mean volume of the tetrahedra constituting its approximating mesh.

When comparing the convergence of the estimated gravitational attraction with that of the overall mass of the object (see figure 3.22), it becomes clear that most of the discrepancy at any mean size of the tetrahedra is due to the falsely estimated volume of the object. The error made by approximating the tetrahedra as point-masses is only a secondary effect, and also becomes less important with shrinking volume of the fragments as seen from the ratio of the errors. As most other parts of the set-up are

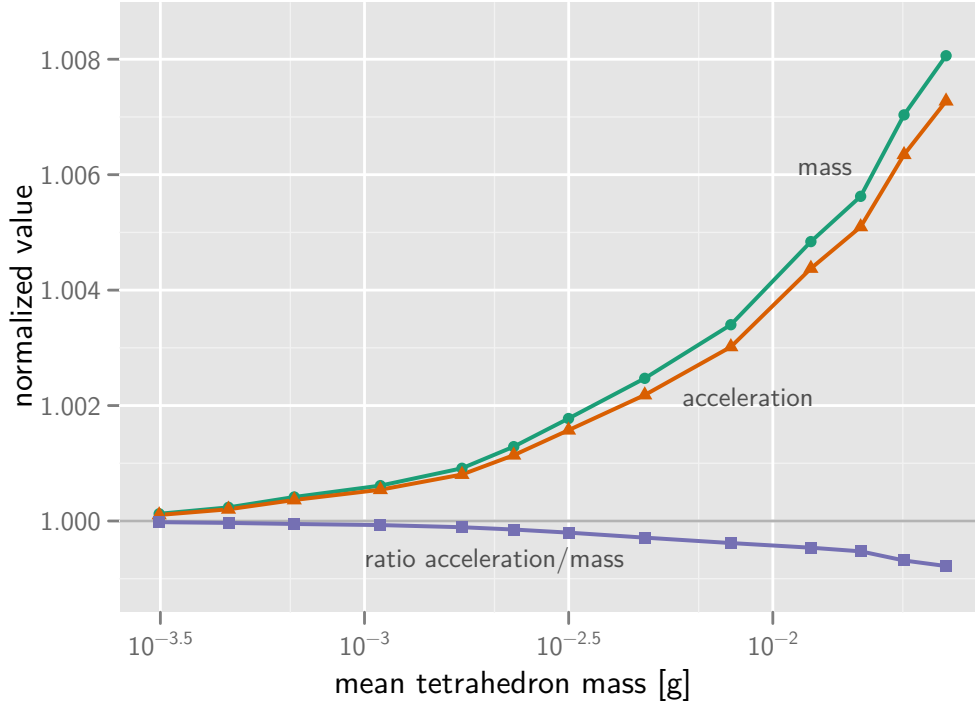


Figure 3.22.: Total mass and acceleration computed for the test-piece with varying coarseness of the mesh and scaled to limit value. Both quantities converge with growing number of tetrahedra (shrinking mean mass), but the ratio of the quantities close to unity reveals, that the main effect is an improvement in the estimation of the part’s volume and thus mass.

further from the atoms and more regularly shaped, it seems sufficient to chose a mean mass of the tetrahedra of 10 mg to obtain an upper bound on the error of 0.5 %. This approach takes into account that parts made from less dense materials e.g. aluminium will also contribute less to the gravity of the apparatus and hence are allowed a slightly larger error budget.

When meshing the parts of the apparatus, the chosen mean volume proved also to be the limit feasible with reasonably capable hardware, as more voluminous and complicated parts needed 4 GiB of RAM during processing. The resulting mesh contained up to 10^6 tetrahedra for the larger parts (e.g. the MOT-chamber) and a total of 2×10^7 for the complete apparatus.

In a next step, the gravitational acceleration exerted by each building part was calculated. To this end the corresponding set of point-masses was

3. Experiment

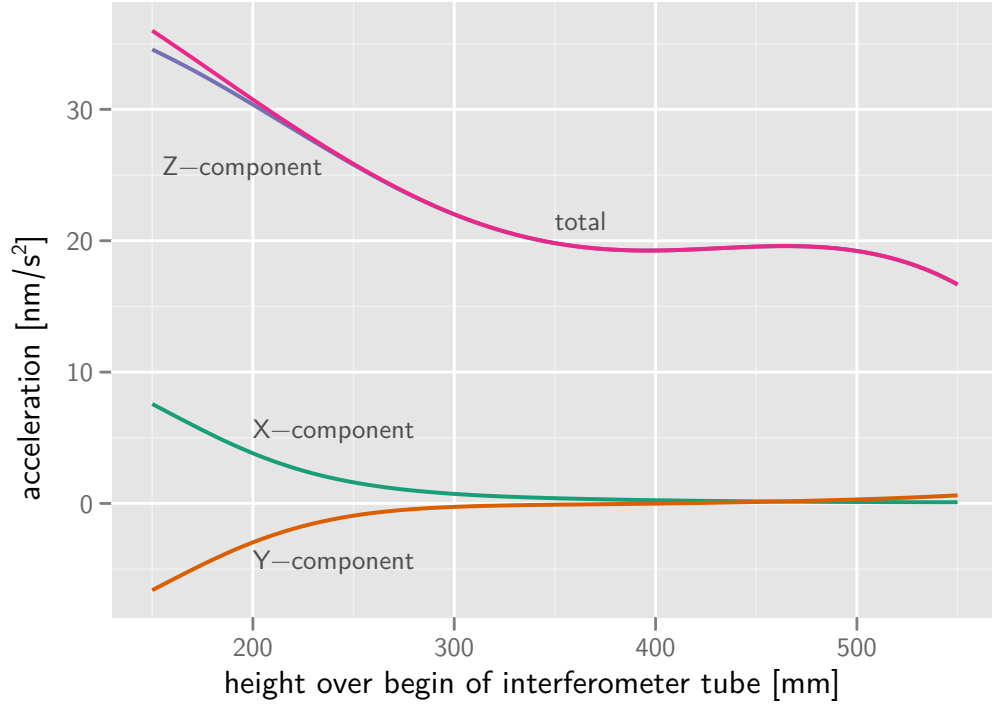


Figure 3.23.: Gravitation caused by the apparatus at the location of the interferometer. Positive values of the Z-component refer to downward acceleration.

rotated and positioned as to occupy the proper place in space, and its attraction was calculated from Newton's law for a rectangular grid of points filling the tube on top of the fountain. The result was stored into a database for further analyses. As an example, the 20 most important sources of (vertical) gravity are identified and depicted in figure 3.24. Not too surprisingly, it is the magnet of the ion pump close to the interferometer-zone with a mass of a bit more than 6 kg, which has the largest effect. As it accounts for less than 20 % of the overall acceleration, modelling of the whole apparatus is still important.

For the zone where the interferometer takes place, the combined effect—averaged over an inner area of $\varnothing 16$ mm—is plotted in figure 3.23. Mostly due to the ion pump, a horizontal acceleration is present at the lower end. As the interferometer is only sensitive in the vertical direction, and as the Z-component is much larger, it is neglected in subsequent treatment. However, the vertical component needs further consideration as its magnitude is well above the targeted accuracy of 5 nm s^{-2} .

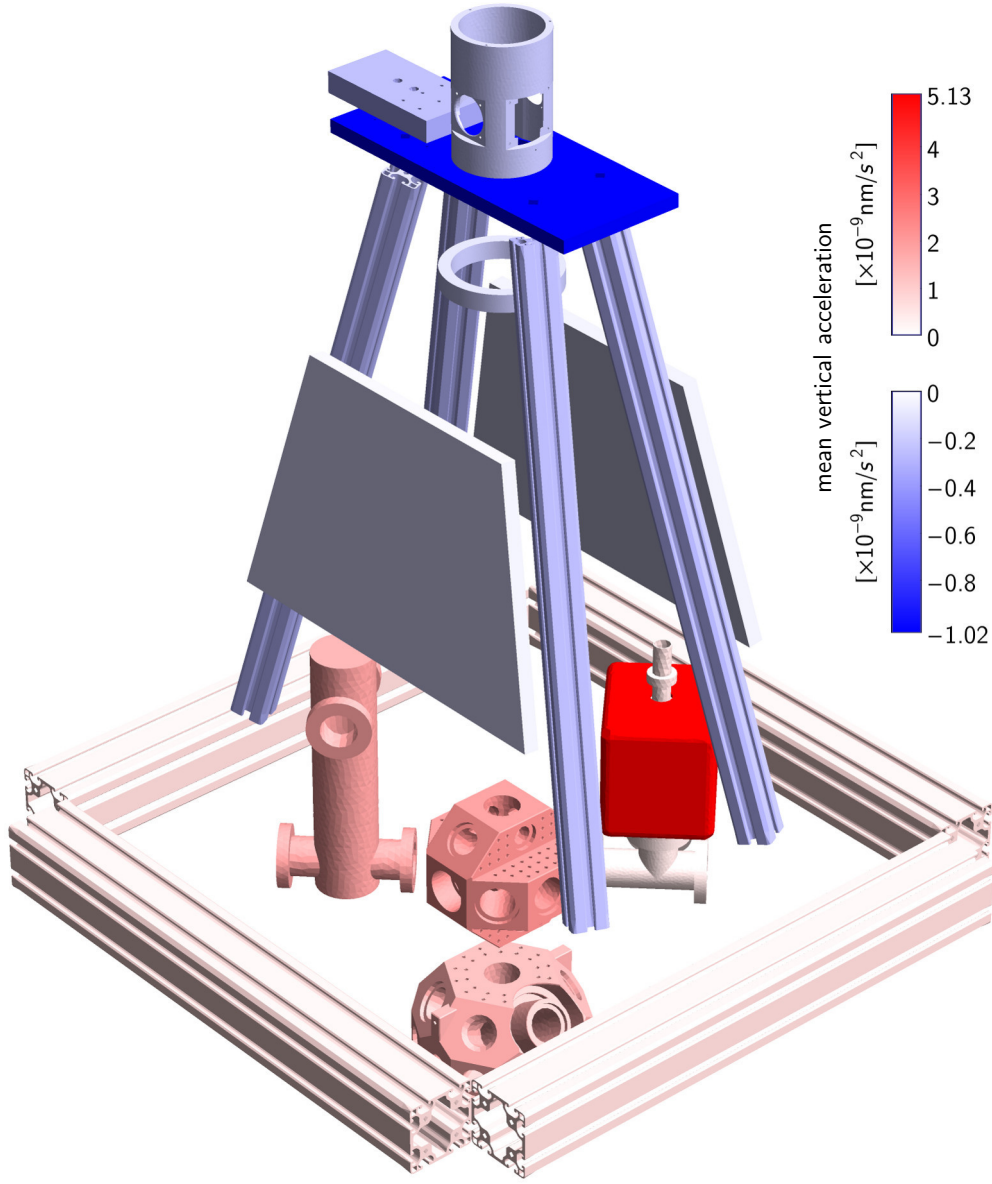


Figure 3.24.: Shown are the ten predominant sources for upward (**blue**) and downward (**red**) acceleration exerted by the apparatus at the location of the interferometer sequence. Together they provide for 51 % of the erroneous gravitational effect.

3. Experiment

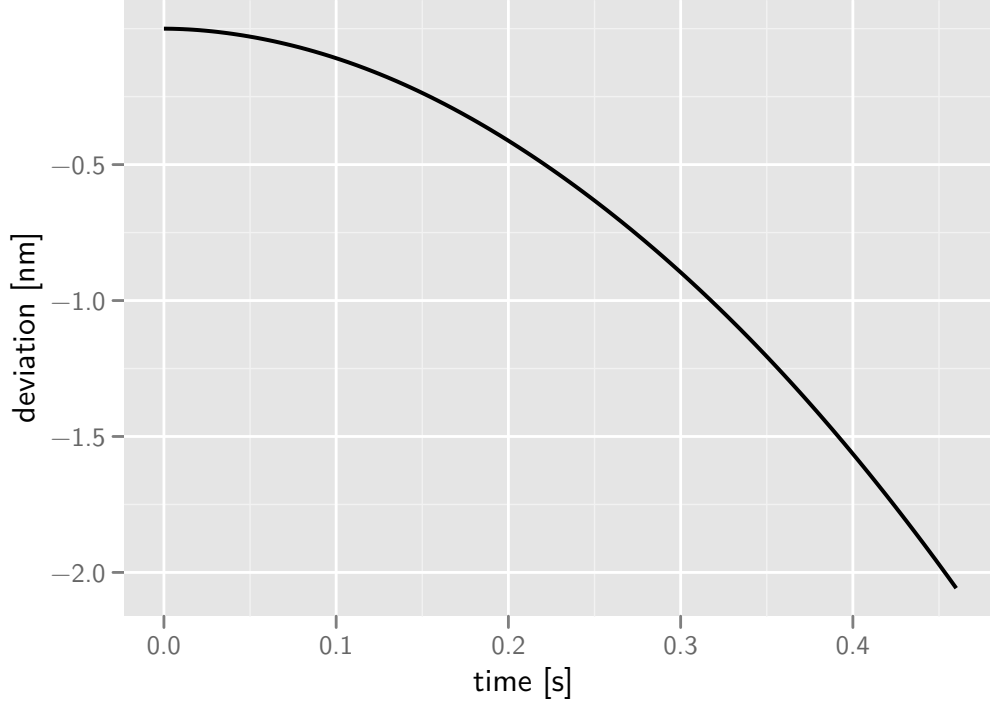


Figure 3.25.: Difference in the trajectories of the upper path with and without the additional gravity of the apparatus. A small splitting of 0.007 nm in the end-points when compared to the analogue for the lower path would not be visible.

The evaluation of the deviation in g is split into a part originating from light-interaction and another connected to free evolution. The perturbed trajectories are calculated as a simple numerical approximation of the movement of the atom subjected to an acceleration

$$g = g_0 + g_{\text{fountain}}(z), \quad (3.21)$$

where $g_0 = 9.80665 \text{ m/s}^2$. The part from free evaluation is estimated as the discretized action integral with the Lagrangian

$$L = m \left(\frac{1}{2} \dot{z}^2 - \int_{z_0}^z g(z) dz \right) \quad (3.22)$$

over the loop of the perturbed trajectories closed with a small non-classical piece. The resulting effect in measured g is always $< 0.1 \text{ nm s}^{-2}$ and further omitted. The deviation connected to a slightly altered position of the atoms

during light pulses is calculated as

$$\delta g = ((z_{\text{up}}(T) - z_{\text{up}}(0)) - (z_{\text{lo}}(2T) - z_{\text{lo}}(T))) / T^2 - g_0, \quad (3.23)$$

where z_{up} , z_{lo} denote the upper and lower path. The resulting effect for various T and various heights h above the lower end of the interferometer tube is given in table 3.1. As most of the deviation is caused in the region where the atoms are slower, and thus stay longer, the erroneous acceleration is mostly dependent on the position of the apex. A maximum value of 20.7 nm s^{-2} is obtained for the lowest apex (only possible for a rather short $T = 200 \text{ ms}$), which places this effect among the moderately important systematics, but still one of those necessary to pay attention to.

variable T		variable h	
T [msec]	δg [nm/s ²]	h [mm]	δg [nm/s ²]
160	18.3	370	20.7
170	18.3	385	20.2
180	18.4	400	19.9
190	18.4	415	19.7
200	18.5	430	19.6
210	18.5	445	19.6
220	18.6	460	19.6
230	18.6	475	19.6
240	18.7	490	19.5
250	18.7	505	19.4
260	18.8	520	19.1
270	18.9	535	18.7

Table 3.1.: Effect of gravity of the apparatus. T is the spacing between Raman pulses and h the height of the apex above the lower end of the interferometer tube. The values were obtained for fixed height $h = 540 \text{ mm}$ and $T = 200 \text{ ms}$ respectively.

As seen before, the error in approximating the gravitational effect of the apparatus due to the finite size of the tetrahedra is less than 0.5 %. The actual positions of the parts are known with similar accuracy. So the largest source of error is connected to wrongly estimated densities of the materials (e.g. the compound of some alloys is not precisely known)

3. Experiment

and—most importantly—the uncertain geometry of the commercial parts. While some companies—like VAT, the supplier of the vacuum valves—provide detailed CAD-drawings⁴, others fail to do so. Namely Varian, the manufacturer of the ion pump, gives only very vague information about the dimensions and materials of their products. While some effort was put into estimating the geometries and masses of pump body and attached magnet an uncertainty of 10 % still needs to be assumed. For all other parts an error of 5 % in the density is assigned, which gives an overall uncertainty of 6 % connected to the values shown in table 3.1.

3.7. Laser

The tool with which the atoms are manipulated, and which ideally would also be the only influence acting on them besides gravity, is the laser light applied during the various phases of a single interferometer shot. This requires highly stable and versatile laser sources with tight control over their spectral qualities, and the ability to precisely determine when and how much light is administered. Moreover, the system used to generate and shape the light needs to be mobile and rugged in order to fulfil the specifications of an instrument for field use.

A suitable implementation was developed in the course of the work done by Malte Schmidt in pursuit of his doctorate and is described in great detail in his thesis [70]. Therefore, only a summary of the main characteristics is given in the following section.

3.7.1. Optics

Cheap diode laser (Sharp GH0781JA2C), commonly used in optical PC drives, were chosen as the source of coherent light for their availability, compactness, good modal and reasonable optical properties at wavelengths close to the desired 780 nm. They deliver 120 mW of light at currents of up to 170 mA, with a linewidth around 100 MHz determined by the short length of their optical medium of about 250 μm .

In order to properly address the atomic resonances and especially to establish a high-quality phase-lock between the Raman lasers, the spectral qualities of the diodes need considerable improvement. To this end, the

⁴Some caution seems advisable here. It is not an uncommon practice to deliberately insert errors into publicly available drawings in order to make reverse engineering more difficult.

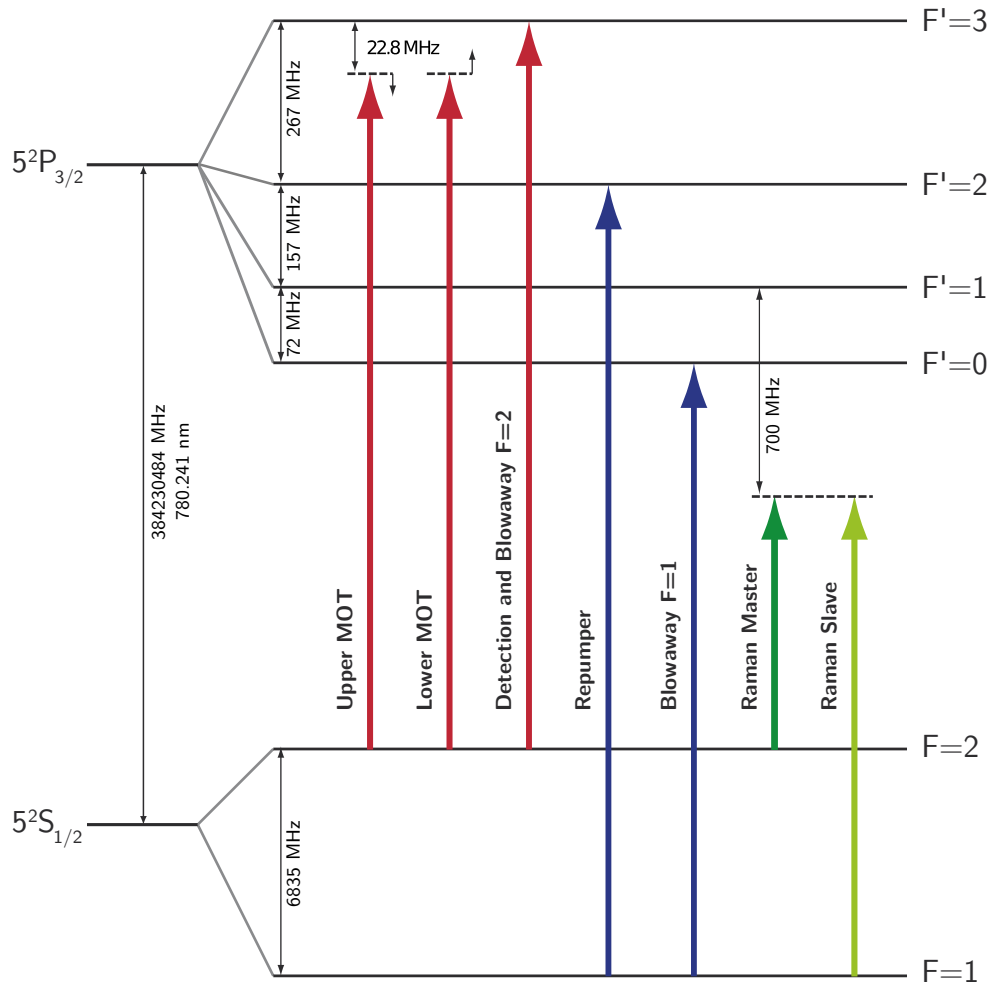


Figure 3.26.: Level scheme of the D_2 -transition of ^{87}Rb and the laser frequencies used in the atom interferometer. Based on a figure by M. Schmidt.

3. Experiment

diodes are incorporated into an external resonator formed by the back facet of the diode and an additional piezo-controlled mirror 80 mm apart, brought together in a thermally stabilized block of aluminium. A narrow interference filter inserted into the light path ensures mono-mode oscillation with only minimal displacement of the laser beam. This design—dubbed an interference-filter stabilized External-Cavity Diode Laser (ECDL)—was first described in [98] and is highly suitable for very compact and rugged laser sources. It is the basic building block of the three distinct laser modules used in the interferometer.

The greater length of the cavity reduces the linewidth to $\ll 100$ kHz. By simultaneously adjusting piezo length and diode current a mode-hop-free tuning range of over 9 GHz is achieved, spanning a spectral range including the D2-resonances of both ^{85}Rb and ^{87}Rb . By modulating the current alone, this range shrinks to 60 MHz but with a possible bandwidth of up to several GHz.

One of these improved laser sources is locked to an atomic resonance by means of Modulation Transfer Spectroscopy [99], where for technical reasons the $F = 3 \leftrightarrow F' = 4$ -transition in ^{85}Rb was chosen. Using digital phase-locks, the other lasers are bound to this reference, which enables to bridge the substantial frequency gaps between different types of light used for the experiment (compare figure 3.26). Special emphasis was put on isolating the reference laser from thermal and mechanical disturbances and on making the spectroscopy lock highly stable.

During the MOT and for the beamsplitters several hundred milliwatt of light are needed. These are generated in a Master-Oscillator-Power-Amplifier (MOPA) configuration where a fraction of the ECDL-light is used to seed a Tapered Amplifier (Eagleyard Photonics). Proper mode-matching allows to draw up to 1 W of light from these semi-conductor devices, from which with some care around 60 % can be fed into an optical fibre. Two separate pairs of MOPAs are used, one provides the light needed for cooling, state selection and detection and the other that for the Raman lasers.

Switching and shaping of light pulses is done with AOMs driven by frequencies of 80–200 MHz. This range is conveniently addressed by Direct Digital Synthesis (DDS), a versatile frequency generation technique available pre-packed in dedicated integrated circuits. The technique allows for highly precise and flexible control over the timing and the frequency of laser light at different points in the experiment, and is the basis on which the control-system of the experiment is founded (see next section). Voltage-variable attenuators in the rf-paths feeding the AOMs enable fine-grained

modulation of the amount of light diffracted by the acoustic wave and thus shaping of the light pulses.

To meet the demands for a compact system, the laser set-up was split into four modules, each at most $42 \times 42 \times 10.5 \text{ cm}^3$ in size. The splitting was based on functionality, so that sub-systems for the reference laser, cooling- and detection laser, Raman laser and switching and apportioning were formed. The light is distributed between the modules and to the experiment by means of polarization maintaining fibres, which helps greatly in decoupling the different systems. The compact dimension were made possible by miniaturized optics developed for the QUANTUS project [100], adapted for the needs of the interferometer.

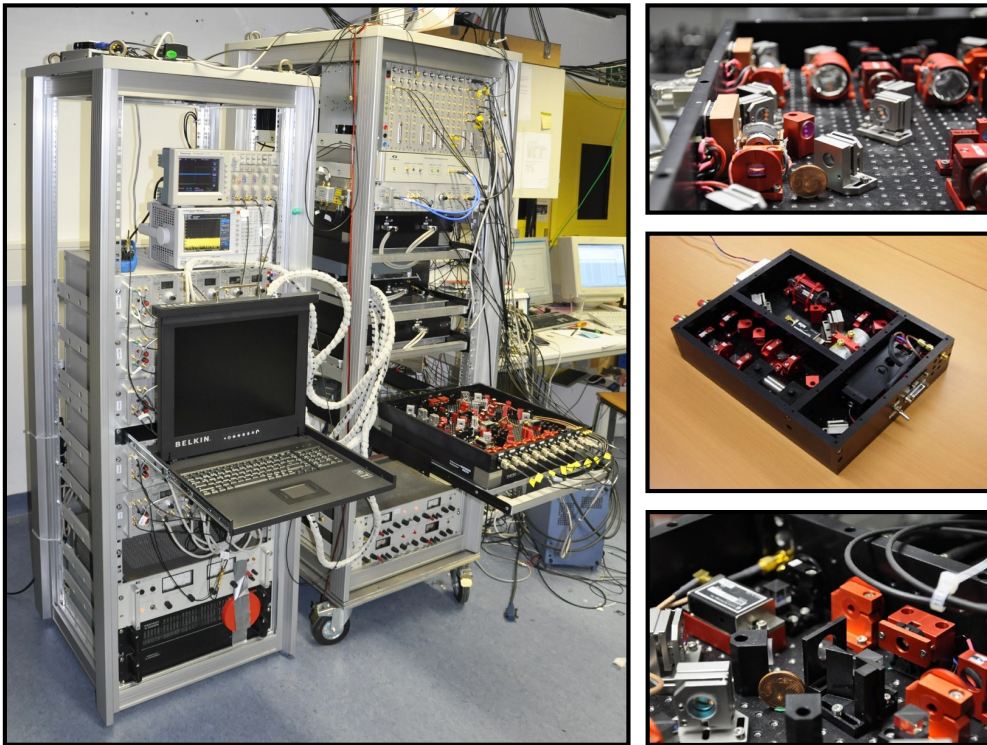


Figure 3.27.: Pictures of the miniaturized optics (**right**) used for the laser system (mounted inside a rack, to the **left**). The two racks also contain the frequency reference, electronics, control system and power-supplies and—along with the fountain set-up depicted earlier—form the complete atom interferometer. The combined mass of both racks is estimated close to 200 kg and up to 1 kW of electrical power is needed for operation. Photos courtesy of M. Schmidt.

3. Experiment

3.7.2. Raman Phase Lock

Of crucial importance for the sensitivity and accuracy of the interferometer is the phase-lock between the pair of Raman lasers which drive the matter-wave beamsplitters. Together with Marco Prevedelli from the Università de Bologna, an ultra-stable control-loop was developed as described in [101]. For this purpose, the light of the two MOPAs in the Raman-module is overlapped in an optical fibre for spatial mode-cleaning and to prevent pointing-instabilities. After the fibre, a small fraction is directed onto a fast photodiode, which gives a beat-signal close to the desired splitting of 6835 MHz.

The beat is mixed down to about 90 MHz and compared to the signal of a DDS at the same frequency by a low-noise phase-frequency-detector (On Semiconductors MC100EP140). The resulting error signal with a SNR of 121 dB/Hz is fed to a slow conventional PI-controller, which sets diode current and piezo voltage of the slave Raman-ECDL mainly for frequency compensation, and to a 30 MHz-fast phase-control path, which modulates the current of the laser diode directly. By careful tailoring of the circuitry a locking-bandwidth of 4 MHz was achieved, which keeps any detrimental resonances of the control-loop well above the range of 100 Hz to 60 kHz, where the interferometer is most sensitive to noise in the Raman beams. Consequently, the phase noise spectral density of the closed loop could be limited to less than $1 \mu\text{rad}/\sqrt{\text{Hz}}$ in this band (compare figure 3.28). Additionally, the high agility of the loop allows to chirp the difference frequency between the Raman beams in order to compensate for gravity induced Doppler shifts (required rate $\approx -25.1 \text{ MHz/s}$) by simply altering the reference-frequency provided by a DDS.

3.8. Frequency Reference, Timing and Control

The working principle of the interferometer can be summarized as the ability of the atoms to very precisely accumulate the phase of the light field experienced at three specific points in time. From this picture it becomes clear that the corresponding frequencies as well as the timing of the light pulses have to be known with high accuracy in order to reach the goals set for the gravimeter.

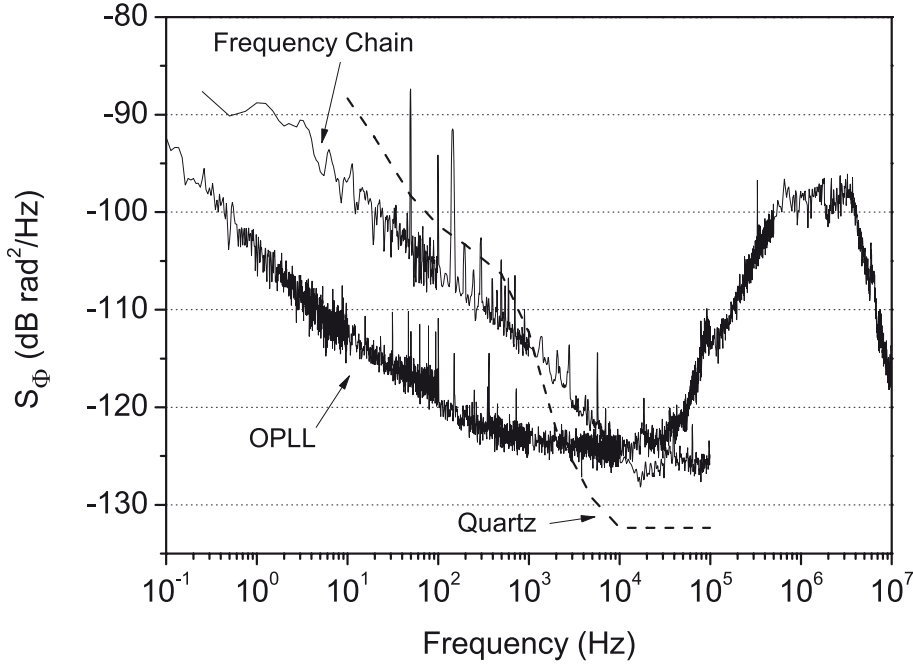


Figure 3.28.: Phase noise spectral densities of the quartz and that of the frequency chain used to scale its frequency to 6.8 GHz. Also depicted is the phase noise spectral density of the optical phase lock loop (OPLL) of the Raman lasers. Figure courtesy of M. Schmidt.

3.8.1. Frequency Chain

The basic clock of the experiment is a combination of two ultra-low-noise quartz oscillators: a 5 MHz Wenzel Blue Top to which a 100 MHz Wenzel SC Premium is locked in a Spectra Dynamics DLR-100 system. This way, the excellent short-term stability depicted in figure 3.28 is achieved. To prevent long-term drifts in the Blue Top, it is bound to a 10 MHz-GPS-signal with sub-Hertz bandwidth, which in turn profits from the characteristics of a world-wide network of atomic clocks.

To provide all other frequency references used in the interferometer (mostly 400 MHz for the DDS), as well as the microwave frequencies necessary for Raman phase-lock and state-preparation, a frequency chain developed by the group of Arnaud Landragin at SYRTE in Paris [93] is employed. The 100 MHz of the Wenzel SC Premium are doubled and then expanded to a harmonic series with multiples of 200 MHz by a comb generator (Picosecond Pulse Labs LPN 7100). Finally a dielectric resonator oscilla-

3. Experiment

tor (Raditek RDRO-A-M2-6.8-14d-18V-E-a1) is phase-locked with an offset of 55.32 MHz provided by a DDS to the 34th harmonic, resulting in the 6744.68 MHz necessary for the OPLL discussed above.

To assess the limitation to the interferometer's sensitivity given by the fluctuations of frequency reference and OPLL, the sum S_ϕ of the spectral noise densities given in figure 3.28 weighted with the gravimeter transfer function is summed, which gives the variance due to Raman phase noise

$$\text{Var}(\phi_{\text{Raman}}) = \sum_{n=1}^{\infty} |H_\phi(2\pi n f_c)|^2 S_\phi(2\pi n f_c) \approx (6.0 \frac{\text{mrad}}{\sqrt{\text{Hz}}})^2. \quad (3.24)$$

The uncertainty of $6.0 \text{ mrad}/\sqrt{\text{Hz}}$ corresponds to a standard deviation per shot of 6.9 nm s^{-2} , which is well below the noise induced by vibrations.

3.8.2. Control of the Experiment

The operation of the interferometer as a gravimeter is a rather complex task, where a variety of sub-systems need to be actuated with high reliability and accuracy. All manipulating of the light (shaping and switching of laser pulses as well as setting the exact phase and frequency) is done with AOMs, which in turn are controlled by DDS and voltage-variable attenuators in their rf-path. These again are addressed by voltage signals from a bank of computer-controlled I/O-boards, capable of generating and receiving digital and analogue signals. As these systems are essential for the quality of the gravimeter a short description of the developed techniques is given in the following sub-section.

The DDS used are AD9959 from Analog Devices which provide up to four independent frequencies. Their phase noise power spectral density at AOM-frequencies around 100 MHz is specified to be better than -134 dBc/Hz for an offset of 1 kHz from the carrier and dropping to -154 dBc/Hz for offsets larger than 1 MHz. Assuming a relevant bandwidth of 50 MHz for the rf-signal affecting the light in the AOM, this gives a rms phase error⁵ of $\leq 200 \mu\text{rad}$, which is negligible compared to other noise sources. These numbers hold for a clocking given by an external high-quality reference⁶ of close to 500 MHz fed to the chip directly, avoiding any internal clock multiplier. The DDS feature a frequency tun-

⁵The conversion from phase noise PSD to phase noise spectral density is simply $L(\delta f)(\text{dBc/Hz}) = S_\phi(\delta f) - 3\text{dB}$, compare [102].

⁶Here provided by the frequency chain.

ing resolution of at least 0.12 Hz and 2×14 bit resolution in phase offset over a range of $2 \times 2\pi$, along with the ability to phase-continuously chirp the frequency with set-able rates. All settings can be programmed to the internal registers beforehand and triggered with fixed latency by CMOS signals.

The DDS are incorporated in Novatech models 408B and 409B which provide for additional filtering (smoothing) of the outputs and for programming of the AD9959 over a RS-232 interface. The 409 features a table mode where the DDS is put through a programmed sequence of frequencies and amplitudes of all four channels, while the 408 makes use of only one channel as to avoid deteriorating of the signal due to crosstalk between outputs. All devices were slightly modified to allow for triggering of the table steps (409) or phase shifts (408) by directly feeding digital pulses to the Analog Devices chip in order to avoid jitter caused by the Novatech circuitry. Up to 12 channels of three 409s provide general-purpose frequency signals to address less critical tasks in the laser system, while two 408 are solemnly used to control the frequency chirps and phase shifts needed in the Raman phase-lock.

Except for programming of the DDS all other parts of the experiment—mostly shutters in the laser beams and switches and attenuators in the rf paths—are controlled by precisely timed voltage signals. These are generated by National Instruments I/O-boards (1×DAQ M 6259 and 2×DAQ M 6229), with a total of 64 digital and 32 16 bit-wide analogue outputs updated at a rate of maximal 4 MHz when dedicated channels are used. These cards are housed in a PXI system of the same vendor and controlled by an embedded computer system NI PXI-8196 (Pentium M 2 GHz, 2 GiB RAM) running Windows XP.

Developing (2.3) for small time variations δT yields

$$\delta\phi = k_{\text{eff}}g2T\delta T. \quad (3.25)$$

The effect of jitter—and more importantly—latencies and drifts need to be limited below the rms-noise per shot and targeted fractional accuracy respectively. For the more stringent requirement of accuracy this translates to an uncertainty of

$$\frac{2\delta T}{T} < 5 \times 10^{-10} \quad (3.26)$$

which is equivalent to a deviation $\delta T < 57$ ps from $T = 230$ ms. For the jitter a much higher limit of 2.3 ns (rms per shot) is valid. While the stability of the frequency reference as the basic clock is guaranteed to exceed these

3. Experiment

specifications, timing of the Raman laser pulses within these limits is a non-trivial task. This is especially true for a timing system which needs to be highly versatile and configurable in order to allow for quick adaptation in the course of research and prototyping.

To circumvent the notorious timing instabilities of modern PC operating systems, a scheme was adopted where all triggers are generated by a clock-system fully implemented in hardware. To this end, the I/O-boards mentioned above are tethered to a trigger pulse generator written into a Field-Programmable Gate Array (FPGA) (NI PXI7951) housed in the same PXI system as the controller and I/O-boards. By exploiting the highly stable trigger lines with fixed latency featured by the PXI system, the digital pulses needed for triggering external events can be generated with exceptional stability. This was verified by measuring the difference in arrival time of the raising edge of subsequent TTL-pulses generated by one of the I/O-boards with a Pendulum CNT-90 timer/counter, clocked by the same external reference. The resulting deviations, both random and directional, from nominal timing were well below 50 ps limited by the resolution of the counter.

The desired flexibility is achieved by implementing the trigger pulse generator with a double counter structure. While one counter is processing a list of points in time at which specified trigger lines are fired to cause the I/O-boards to output the desired voltage signals, the other counter is fed with a new data-set. Similarly, both the DDSs as well as the I/O-boards are supplied with new instructions during the 600 ms-long MOT-phase, when all settings of the experiment are static. After the MOT, counters are switched automatically and the timing hardware runs fully autonomous until the next MOT-phase, with zero dead-time between shots. This way, stable timing unaffected from OS glitches is ensured, while almost the same flexibility is obtained as with a system implemented solely in software.

The timing hardware is the lowermost layer in a hierarchically organised control system. As depicted in figure 3.29, the superordinate layers are written in LabView and run parallel to each other in the Windows OS. Communication between different parts is done through FIFOs and a messaging system, which ensures a proper sequence of interdependent steps in the otherwise asynchronous execution. This approach was chosen to allow prompt reaction to user input while being able to guarantee timely reprogramming of the hardware layer. It is also robust against some temporarily failure modes, e.g. denied storage access due to high OS disc activity. In this particular case, data to be saved is piled up in the FIFOs until writing

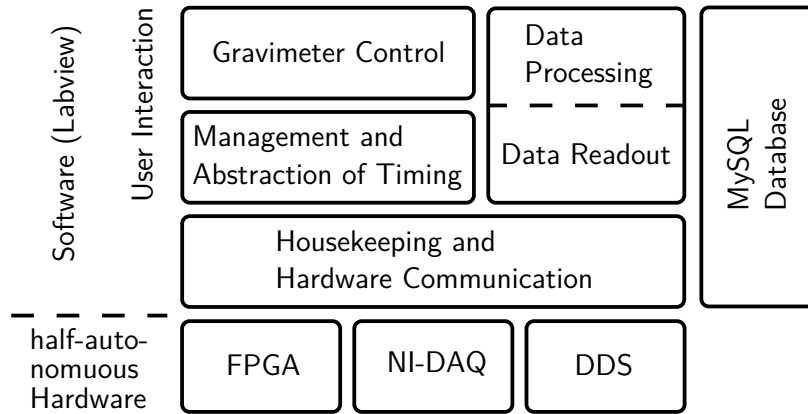


Figure 3.29.: The system used to control the experiment is organized in several layers. Situated at the bottom is the hardware, which autonomously operates the interferometer during each shot and is only reprogrammed in the static MOT phase. With ascending layers, the timing data gets more and more abstracted and is easily configured by the user through graphical user interfaces at the top. Data acquisition and storage are parallelized and run partly on different computer systems.

to the disc is possible again, without impairing the regular cycle of the gravimeter.

The middle layer is used for general house-keeping, initializing the other parts and communication with the timing hardware. The superordinate layer is responsible for user-interaction and management of the central data-structure: a list of time-spans, during which a digital or analogue signal is to be output through an associated hardware-channel. As the beginning and end of each pulse can be referenced to other pulses, functional blocks in the fountain sequence can be organized. These might shift in time according to e.g. an extension of the MOT duration, in order to reposition all subsequent steps. This way, a highly flexible description of the interferometer cycle is obtained, which allows for easy variation of certain parameters—e.g. height of the apex—without the need to manually alter all dependent time-steps.

A separate part of the program is dedicated to read and process sensor input brought in through the digitizers incorporated in the I/O-boards. Most importantly this is the interferometer signal, but also includes tilts, temperatures, residual vibrations on top of the isolation stage and other environmental data which might affect gravimeter performance. This information is stored in a MySQL-database in human-readable form along with

3. Experiment

all details of the sequence for further reference. The interferometer response is also exposed to other parts of the control system to enable feedback loops necessary for the course of the experiment.

3.8.3. Measuring Scheme for Gravity

For small phase shifts $\Delta\phi$ in the interferometer, the fraction of atoms left in the initial sub-state is described by the simple formula

$$P_{(F=2)} = \frac{1}{2} (1 + C \cos[\Delta\phi + \Delta\phi_0]) , \quad (3.27)$$

where C relates to the contrast of the fringe and $\Delta\phi_0$ describes a potential phase offset needed in data analysis. Conversely, $\Delta\phi$ can be fixed within a range of $[0, 2\pi)$ from the ratio of atoms deduced from the detection signal. This is used to monitor small modulations in g , while the main part is given by a linear chirp applied to the reference frequency to which the beat between both Raman beams is compared. From the chirp an equivalent phase offset can be calculated as

$$\phi_0 = \dot{\nu}T(T + 2\tau), \quad (3.28)$$

where $\dot{\nu} \approx -25.1$ MHz/s. A factor of $\frac{1}{2}$ is lifted as the chirp shifts both Raman lasers in opposing directions.

As part of an absolute measurement of g , the correct value for $\dot{\nu}$ needs to be found. This can be done by observing, that for imperfect cancellation of the Doppler-shift induced by gravity, the resulting phase can be expressed as

$$\Delta\phi = (\dot{\nu} - gk_{\text{eff}})T(T + 2\tau) \quad (3.29)$$

which, according to equation (3.27), leads to a shift of the observed fringe pattern when T is changed. Consequently, the correct chirp rate is found, when the fringe pattern is stationary with respect to a variation of T , as shown in figure 3.30. This is done manually before each long-term gravity measurement.

After initially obtaining the correct chirp rate, further variations in g must be kept track of. This is accomplished in the topmost layer of the control system which adjusts chirp rate and Raman phase so as to cancel any observed changes in $\Delta\phi$. However some subtleties need to be addressed.

From equation (3.27) it is evident, that the interferometer is least suscep-

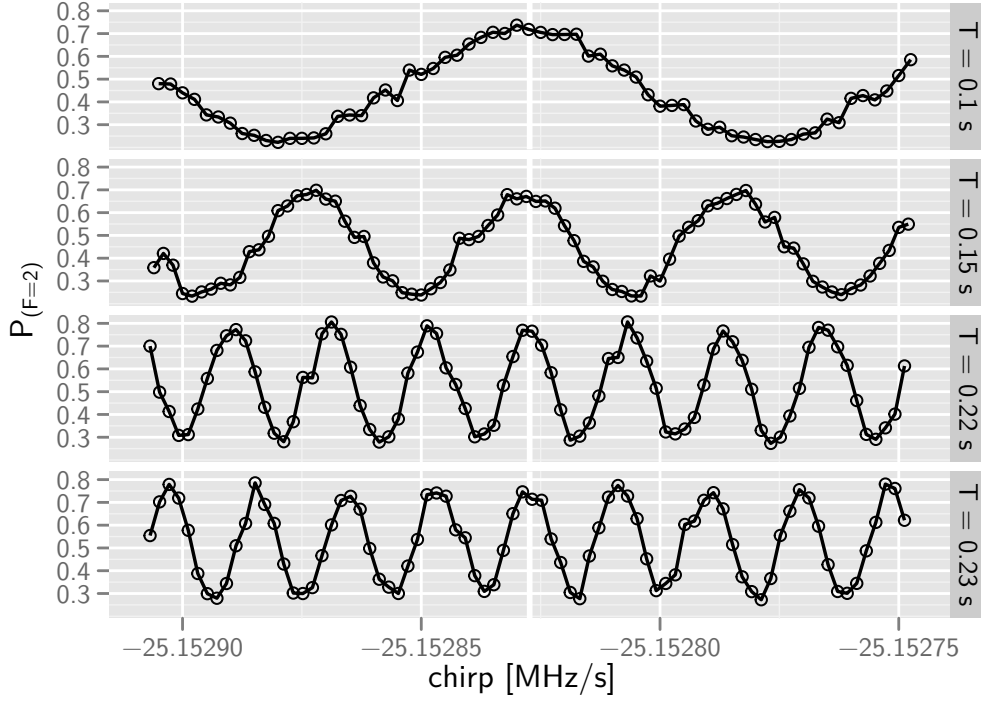


Figure 3.30.: Fringes obtained by scanning the chirp rate for multiple interferometer timings. Only for the rate which exactly cancels the gravitational Doppler-shift, the interferometer phase $\Delta\phi$ becomes independent from variations in T .

tible to small phase changes at the point where $\Delta\phi$ is cancelled. To regain maximal sensitivity it is necessary to add and subtract $\pi/2$ in subsequent shots to the specific Raman phase which perfectly balances the gravitational effect. This results in a pattern where the interferometer "hops" back and forth between the mid-range points of the slopes of the fringe. When the main noise source is independent of the quantum projection noise, a factor $\sqrt{2}$ in sensitivity is gained this way, equivalent to the ratio of the first derivative at the slope to the mean of the derivative over the complete cosine. An additional advantage is an increased robustness against variations in the fringe contrast and moderate drifts in a vertical offset, which otherwise might be interpreted as gravity changes.

The overall measurement process is split into several sections. First, a full fringe is scanned by altering the Raman phase in the second half of the interferometer sequence in small steps over the course of 72 shots. By fitting equation (3.27) to the obtained series, contrast and central phase $\Delta\phi_0$ are

3. Experiment

extracted. In a following section, the gravimeter alternates between right and left slope of the fringe, where at each point the small error of the central phase—mainly caused by noise and gravitational tides—is estimated from

$$\delta\phi_0 \approx \pm \left(\arccos \left[\frac{1}{C} \left(P_{(F=2)} - \frac{1}{2} \right) \right] - \frac{\pi}{2} \right), \quad (3.30)$$

with the sign being dependent on the side of the fringe where the measurement was taken. $\delta\phi_0$ is used as the error signal in a software feedback-loop consisting of an integrator with typical time-constants of 30 s and a weak proportional element. The output is the adjusted estimate of the central phase, which in turn is used to calculate the next "hop". When due to tidal variation $\Delta\phi_0$ approaches π , the chirp rate is altered as to zero the central phase, while the state of the feedback-loop is adapted to the discrete phase jump. For each shot, the parameters of the Raman phase-lock and the interferometer response as read from the PMT electronics are saved to the database. As these quantities contain all obtainable information about the acceleration experienced by the atoms, the measured value becomes independent of the actual implementation and state of the control-loop.

After 15 min of data-taking, the direction of \mathbf{k}_{eff} is reversed by inverting the chirp rate as to cancel a range of systematic effects [61], most importantly frequency dependent phase delays in the microwave electronics [48]. With the adjusted chirp the initial scan as well as the subsequent "hopping" is repeated until 15 min later, when the whole scheme is started all over again. This way a continuous time-series of local gravity possibly spanning several days is obtained. An analysis of such data is found in the following chapter.

4. Results

While the gravimeter is not yet developed to a point where all limiting systematic effects are fully understood, it is nonetheless possible to make high-precision measurements comparable to other state-of-the-art instruments. A valuable evaluation of its characteristics is made possible by comparing gravity data obtained with the atom-interferometer to that from a FG5 measured at the same site. This discussion can be found in a later section of this chapter, while in a first part noise and the resulting limitations to achievable sensitivity are analysed.

4.1. Noise

As the cloud of atoms subjected to the interferometer is an incoherent set of quantum systems, the measurement of the occupation of the hyperfine ground states suffers from full quantum projection noise [103], which ultimately limits the achievable SNR in the interferometer signal to $1/\sqrt{N}$, where N is the number of atoms.

After launch, the cloud consists of roughly 3×10^8 atoms, which are reduced by a factor of 23 through velocity selection, and another factor of 3 by rejecting atoms in the wrong magnetic sub-state. That leaves 4×10^6 atoms for detection, from which about 3.5 % are situated in the detection-volume of $8 \times 8 \times 8 \text{ mm}^3$ due to thermal expansion of the cloud. The resulting number of 1.4×10^5 is equivalent to a SNR of 370. From this ratio a per-shot precision in the measured interferometer phase of

$$\sigma_{\text{proj}} = \frac{C}{\text{SNR}} \approx 1.3 \text{ mrad} \quad (4.1)$$

can be deduced, where C is again the fringe contrast.

However, with the current detection being based on a PMT, this SNR might be difficult to reach.¹ This comes as the noise of photomultiplier

¹To alleviate the situation an improved detection technique is currently being developed, where the atom number is deduced from the absorption signal found in the detection laser in comparison to an unaffected beam. This balanced measurement enables rejection of technical noise intrinsic to the laser [104] and should allow for

4. Results

tubes for the relatively high light levels involved has a strong component independent of the signal, which is mostly due to gain variations connected to environmental effects and hysteresis. Based on experience by other work-groups, a $\text{SNR} > 200$ can nonetheless be expected for typical detection times.

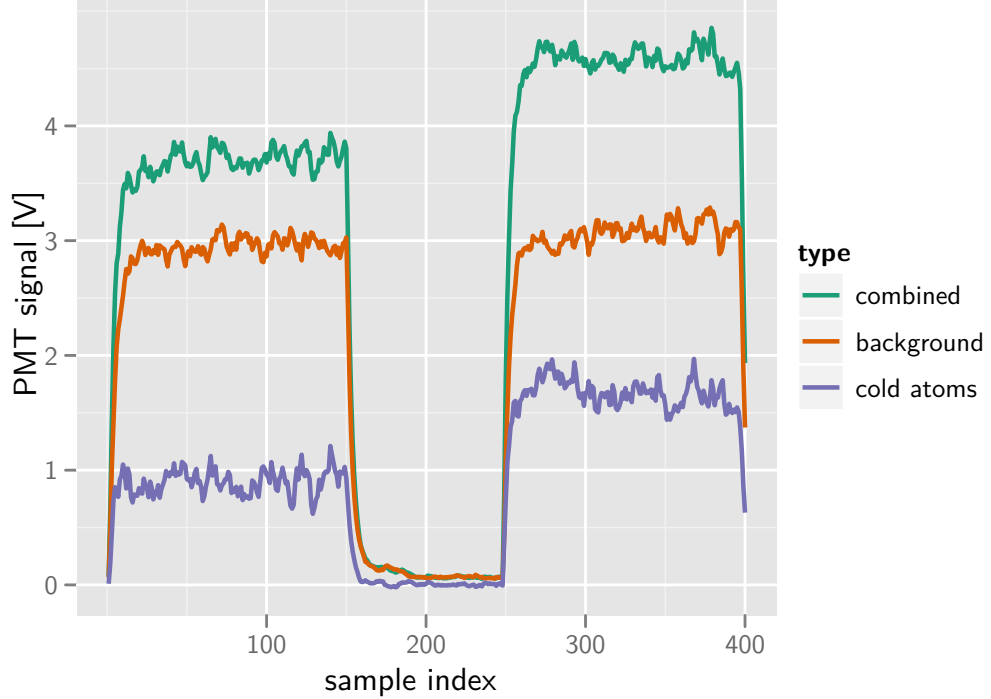


Figure 4.1.: The raw interferometer- and background-signal as obtained during detection, shown with the deduced response of the cold atoms alone.

To assess the actual SNR, the detection signal as depicted in figure 4.1 is evaluated. As described in section 3.3, the signal consists of two time-series of 400 samples each, one covering the pass-through of the atomic cloud, while the other measures the background alone. To recover a zero signal after subtraction with no cold atoms present, it was found necessary to multiply the second set with a factor of 0.95, which is attributed to thermal effects in the AOM used to switch the detection beams. From the difference of the series, the fraction of atoms in $|F = 2\rangle$ is obtained by taking the mean of the ratio of samples in the windows where the

projection-noise limited detection of 10^5 to 10^9 atoms. Some further details can be found in [92].

fluorescence signal is maximal and flat. For the analysis, the edges of the detection pulses were trimmed, as these might be susceptible to hysteresis effects in the PMT.

Calculating the standard error of the mean for the raw signal in each detection pulse, prior to subtraction of the background, yields a fractional uncertainty of 2.4×10^{-3} , which can be translated to a SNR per detection-pulse of ≈ 400 due to signal-fluctuations alone.² This is consistent with the performance expected from a PMT, further supported by the observation that the noise is non-white but shows clear signs of strong low-frequency components, often found in noise generated by technical equipment.

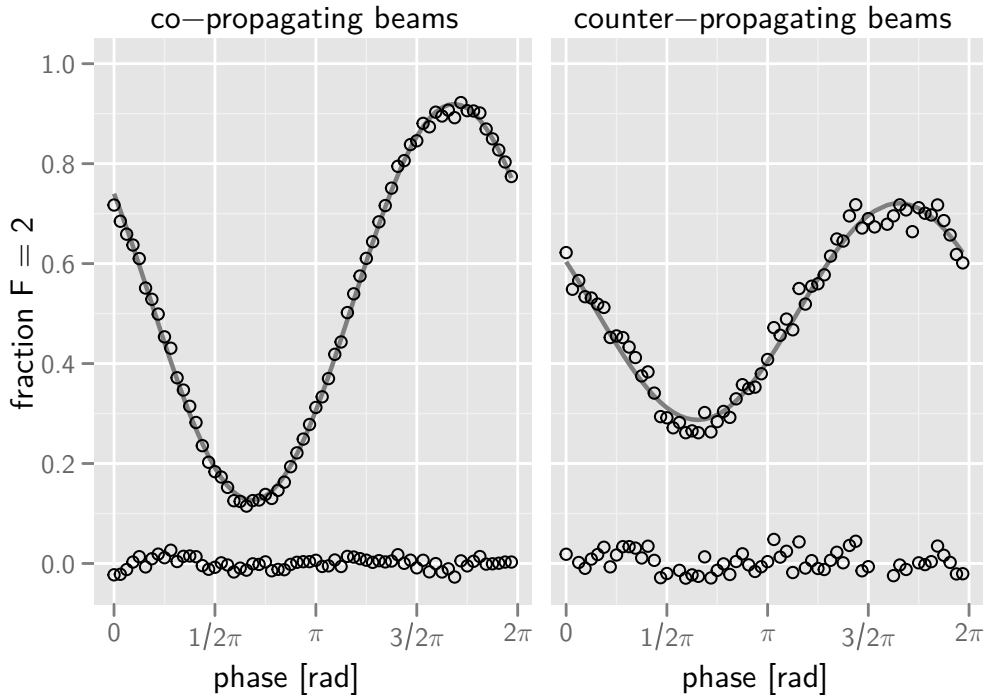


Figure 4.2.: Typical Interferometer fringes obtained with $T = 230$ ms for the case of Doppler-insensitive (**left**) and Doppler-sensitive (**right**) Raman transitions and fitted cosine. The standard deviation σ_{ratio} of the residuals plotted below is 0.011 and 0.02 respectively, yielding a SNR of 80 and 18.

²It might be puzzling at first, that the obtained SNR is higher than allowed by quantum projection noise. Here the quantum nature of the system is not a limitation, as it only concerns the ability to determine the ratio of atoms in different sub-states, not the quality of the fluorescence signal.

4. Results

Computing the ratio of atoms according to the recipe from above combines the noise from all pulses and lowers the SNR per shot to about 100 (signal amplitude is halved during background elimination, 4 pulses contribute). This is indeed what can be observed in fringe data (see figure 4.2) when the influence of vibrations is suppressed by employing a Doppler-insensitive scheme, where co-propagating beams drive the Raman transition. Here the SNR—scaled by the fringe contrast of 80 %—is 80, which allows to identify the PMT-noise as one of the candidates to limit achievable interferometer performance above what is given by quantum projection noise. When scaled to the contrast of the Doppler-sensitive case, this results in a per-shot precision of the gravimeter

$$\sigma_{\text{grav}} = \frac{\sigma_{\text{ratio}}}{Ck_{\text{eff}}T^2} \approx 65 \text{ nm s}^{-2} \quad (4.2)$$

equivalent to a fractional uncertainty of 6.6×10^{-9} in g , when measuring at the slope.

4.1.1. Measured Noise

As can be seen in figure 4.2, in the case of Doppler-sensitive Raman-transitions the noise is roughly doubled. This can best be deduced from a continuous time-series obtained according to the scheme discussed in the previous chapter. Depicted in figure 4.3 is the part of one measurement section (single direction of \mathbf{k}_{eff}) where the interferometer switches between the slopes of the central fringe. The residuals exhibit mostly white noise and little modulation of the averaged value as revealed by the added LOESS smoother³. The resulting resolution of $160 \text{ nm s}^{-2}/\sqrt{\text{Hz}}$ is substantially better than what can be expected from classical gravimeters (see next section) and is competitive with recently reported performance of other atom interferometers [59]. However, as the obtainable resolution depends on site-specific noise a direct comparison with other gravimeters is necessary in order to fully specify the performance.

Further insight is gained from a spectral analysis of the residual accelerations in a gravimetric measurement spanning 18 h, which is given in

³This method adds a curve by point-wise fitting a simple polynomial to an adjustable span of the neighbouring data weighted by their distance. Throughout this work polynomials of degree two and a span of 75 % is used, as implemented as default in the statistical computing environment R [105]. Here the intention of the smoother is only to ease perception of modulation hidden in the data; therefore further details are omitted.

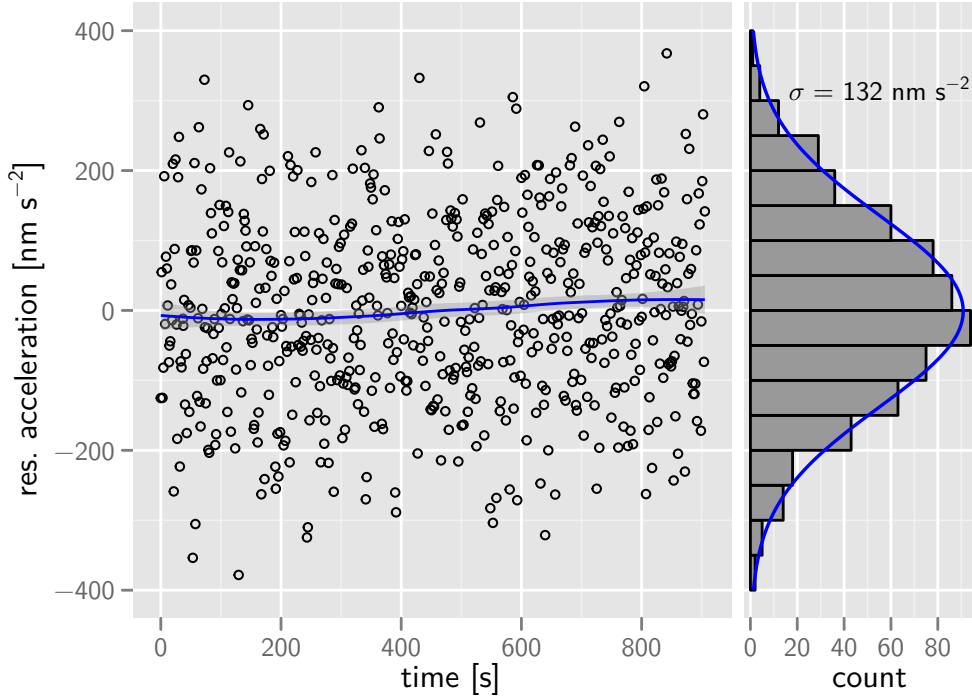


Figure 4.3.: Typical time-series of gravitational data with only tides and the mean subtracted. The depicted standard deviation translates to an equivalent resolution of $158 \text{ nm s}^{-2}/\sqrt{\text{Hz}}$ or $\frac{\Delta g}{g} = 1.6 \times 10^{-8} / \sqrt{\text{Hz}}$.

figure 4.4. The data was corrected for tides, polar motion, air pressure and effects connected to the direction of the effective wave vector, where after its power spectral density (PSD) was estimated. Please note that no further de-trending was necessary to reach the depicted long-term stability. A side-by-side comparison with the PSD obtained from the accelerometer signal on top of the vibration isolation stage shows that the gravimeter is essentially unaffected by environmental noise for frequencies lower than 0.1 Hz. The flat noise floor extending to the left is consistent with the standard deviation found in the time series from figure 4.3, which further supports the assumption of white noise in the measurements, caused mainly by perturbations at higher frequencies. Accordingly, it can be concluded that the rejection of vibrations by the isolation stage at low frequencies is good enough to allow for even better performance.

The integrated accelerometer noise, weighted with the sensitivity of the interferometer, reveals that the strong microseisms present close to 0.1 Hz have a dominant influence on gravimetric noise. As these perturbations

4. Results

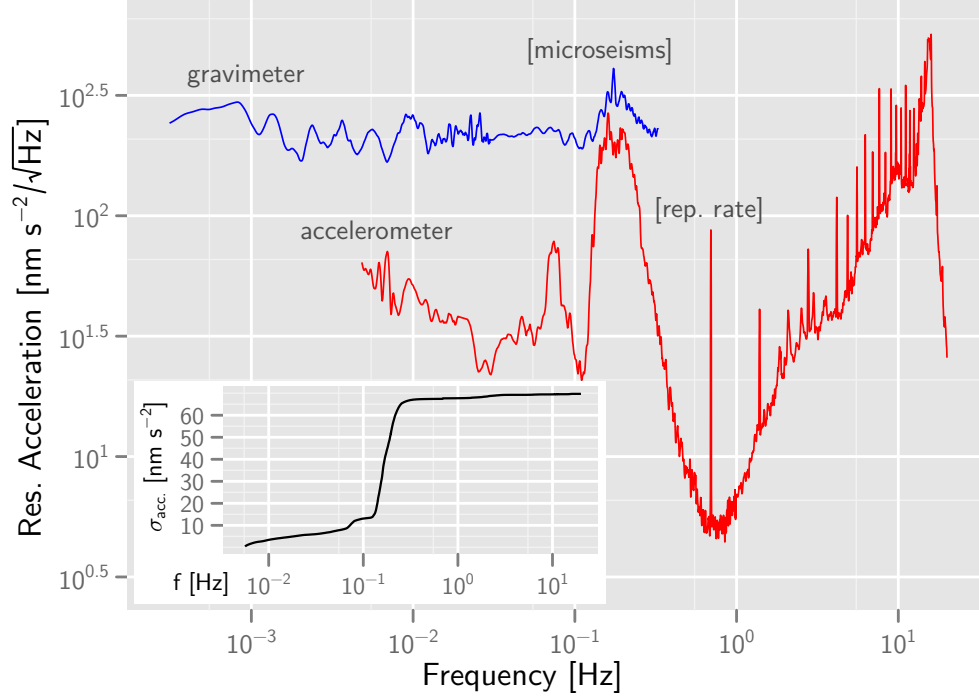


Figure 4.4.: Power Spectral Density of noise in the gravimeter data and accelerations on top of the vibration isolation. Of special concern are the microseisms around 0.1 Hz and the spike at 0.7 Hz—the repetition rate of the experiment—and its higher harmonics. The **inset** shows the square-root of the cumulative sum of the accelerometer-PSD weighted with $|H_{\text{acc}}|^2$.

are somewhat coherent, their effect on longer time-scales is diminished slightly through averaging, and consequently the noise drops off at lower frequencies.

Suppression of environmental vibrations is excellent from there on to higher frequencies, but a pronounced peak at 10 Hz is just within the sensitive range of the gravimeter. In total, the small contributions from frequencies higher than 5 Hz, likely caused by technical sources in the building, are negligible due to the high rejection featured by the isolation stage.

As the accelerometer signal was measured in-loop, the obtained PSD does not necessarily reflect the real situation with highest accuracy. While the qualitative agreement is good enough to suggest it is indeed a truthful rendering of actual conditions, some caution seems advisable concerning the exact amplitude of the residual vibrations. If the small peak found

in the PSD of the gravimeter signal at 0.1 Hz is assumed to be produced exclusively by the microseisms seen in accelerometer PSD, then a corrective factor of 1.6 needs to be applied. This is consistent with the fact that a total noise contribution of $\sigma_{\text{acc.}} = 70 \text{ nm s}^{-2}$, together with the noise from detection, is insufficient to explain the standard deviation found in figure 4.3. However, if the accelerometer signal is amplified by the factor given above—then amounting to $\sigma_{\text{acc.}} \approx 112 \text{ nm s}^{-2}$ —the root-mean-square of both contributions exactly recovers the noise figure found in gravimetric measurements.

In summary, the considerations given above allow to identify environmental vibrations as the relevant limit to currently achievable resolution at sites as noisy as a laboratory in a busy physics department. In general, locations dedicated to high-precision gravimetric measurements are much quieter, so higher performance can be expected there. Performance might then be limited by detection noise.

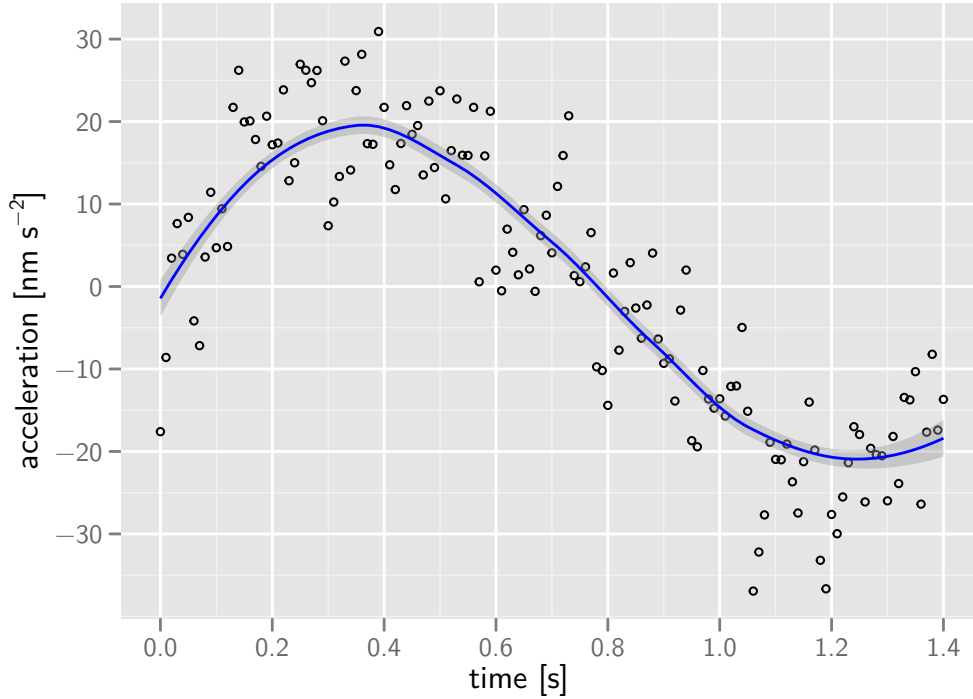


Figure 4.5.: Acceleration signal on top of the vibration isolation averaged over approximately 40000 shots. The modulation is probably caused by the influence of the switched MOT coils acting on housing and sensor of the seismometer in the time span $[0, 0.6] \text{ s}$.

4. Results

Another look at the PSD of the accelerometer reveals a disturbing feature at frequencies related to the repetition rate of the experiment and its higher harmonics. This effect is better approachable in the time domain, when the accelerometer data is cut into segments of the length of one shot synchronized with the gravimeter sequence. When all pieces are averaged, a signal as depicted in figure 4.5 is found.

This disturbance is most likely connected to the switching of the MOT-coils close to the accelerometer. The effect is probably two-fold: a first contribution comes from the accelerations caused by attraction of the steel container housing the accelerometer to the coils, which should mostly be rejected by the control loop. A second part can be assumed due to the impact of the magnetic flux on the sensor inside the accelerometer, causing erroneous acceleration signals, which in turn provoke a reaction of the feedback loop.

As the exact mechanism of the generation of this signal is unclear, as well as its exact amplitude, a reliable estimation of the necessary correction of measured gravitation is difficult. In the lack of a better approach, a value of -10 nm s^{-2} is assumed, the mean of the depicted signal during the time interval when the interferometer sequence is applied. However, the problem should be eliminated in the near future, when a magnetic shield, planned to surround the experiment except for the vibration isolation, is installed.

4.2. Gravity measurement

In late November and early December 2010, a first long-term gravimetric measurement was carried out at the physics department of the HU Berlin in Adlershof (specific characteristics of the site can be found in appendix A). Data was taken over a period of three weeks, during which some smaller technical problems concerning the laser, as well as the control system, could be identified and lifted, leading to a final measurement starting the fifth of December and spanning 15 hours. The resulting series of gravitational data is depicted in figure 4.6. Here, each 15 min-section of data is split into 6 points; one from the initial scan over the whole fringe and five from subsequent "hopping". The gap around midnight was caused by a laser running out of the range of its control loop and subsequent failure of the lock.

As can be seen, variations in g as predicted from theory are followed closely. The solid line given in the top section is the prediction and fitted

with an offset as the only free parameter. The result of the fit is the estimate of local gravity and amounts to

$$g = 9812640796, 2 \text{ nm s}^{-2}. \quad (4.3)$$

A closer look at the data points after subtracting these environmental influences reveals a pronounced modulation of the residuals where the sign depends on the direction of the effective wave-vector (up or down) when the data was taken. This is a systematic effect not yet fully understood, which needs further investigation. However, as the perturbation is eminently symmetric, high precision in the measurement of g can be recovered by averaging measurements with anti-parallel wave-vector. To this end, each pair of consecutive sections with flipping of the wave-vector \mathbf{k}_{eff} in between were shifted to their common mean by applying

$$\tilde{y}_i^\pm = y_i^\pm - (\langle y^\pm \rangle - \langle y^+ \cup y^- \rangle). \quad (4.4)$$

Here y_i denotes the i th data-point in each section, with the direction of the wave-vector indicated by $+$ and $-$.

After removing the symmetric part of the modulation, the data-points still show a small residual drift of $\approx 40 \text{ nm s}^{-2}$ over the course of the measurement as depicted in the bottom section of figure 4.6. Possible causes for this perturbation are creep in the tilt-pad in the vibration isolation⁴, drifts in Raman laser intensity or the frequency reference. The latter is possible as the GPS-receiver used to stabilize the quartz oscillators on long time-scales was found to fall clearly behind the specifications given by the vendor. Evaluation of each of these potential sources showed typical drifts which would result in deviations in measured gravity consistent with the observed modulation.

Statistical Analysis

The basic approach to retrieve local gravity from the experimental data is simple. In principle the steps described in sub-section 3.8.3 are repeated, that is a cosine is fitted to the scanned fringe according to (3.27) and the following hops are evaluated point-wise using (3.30). An estimate for g is then obtained from evaluating the obtained phase-shifts combined with

⁴Unfortunately just in the last days of the measurement campaign one of the axes of the tilt sensor faulted, thus inhibiting the possibility to correct for small tipping in the retro-reflector.

4. Results

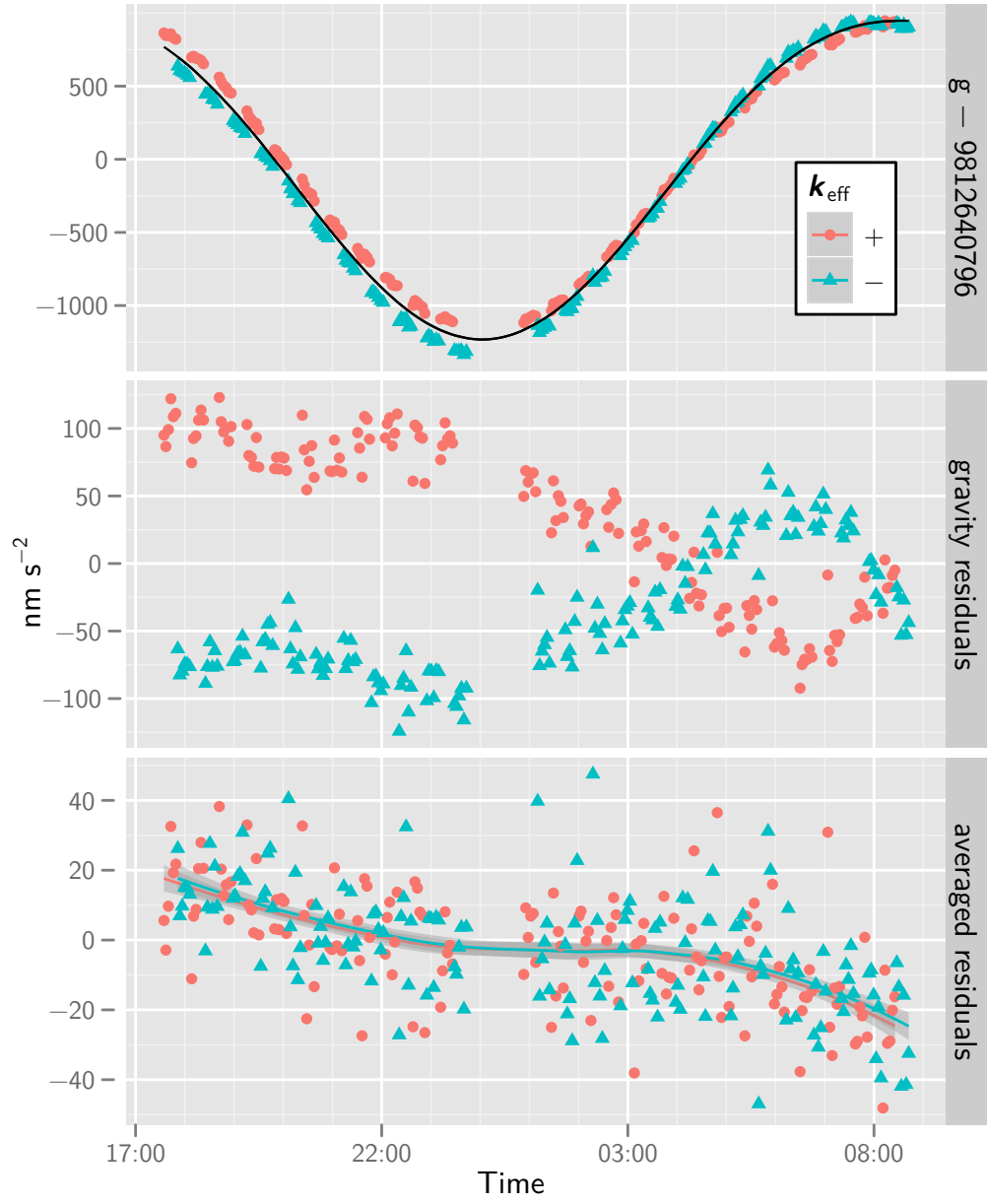


Figure 4.6.: Data from first long-term gravity measurement. **(top)** Variation in measured g by tidal effects. **(middle)** Residuals after subtracting predicted effects. **(bottom)** Residuals after averaging over measurements with flipped wave-vector. LOESS smoother added for clarity.

the result from (3.29) with (2.20).

While this procedure is trivial enough, a range of purely technical subtleties need to be addressed (e.g. finite frequency resolution of the DDS or robust extraction of atomic ratio from noisy PMT-signal) when processing the data. Given the high precision of the experiment, even small mistakes would lead to noticeable changes in the obtained value for g . Therefore, the implementation of the analysis was done independently by four persons exploiting two different statistical frameworks (Mathematica and R) and using different approaches (global non-linear fit vs. point-wise evaluation). Repeated comparison and improvement of the procedure led to an agreement in the results and associated confidence intervals within 1 nm s^{-2} , well within the accuracy limits aimed at with future iterations of the experiment.

It therefore seems safe to specify the statistical uncertainty down to this limit. When evaluating the variance of the averaged residuals including the observed drift, a standard error of 3.7 nm s^{-2} is obtained. However, treating the drift as a systematic effect and removing most of the slow modulation by applying and deducting a linear model, the statistical uncertainty reduces to

$$\sigma_g = 0.8 \text{ nm s}^{-2}. \quad (4.5)$$

If indeed technical sources can be identified as the cause for this perturbation, careful re-evaluation of the analysis procedure is advisable to make full use of the attainable precision.

Some care has been put into the treatment of outliers in the measurement. Occasional glitches in the interferometer lead to $< 1 \%$ of shots which clearly stand out from the rest of the data.⁵ To identify such points, a multi-step scheme was adopted. For each 15 min-section of data, a cosine was fitted to the scanned fringe, and from the residuals those points were removed which are farther away than 1.5 times the span between the first and third quartile from said quartiles. This is similar to a 2σ -criterion assuming a Gaussian distribution, but less sensitive to distortions caused by extreme outliers [106]. From the remaining points, the standard deviation is calculated, assuming that the variation in the data left is now sufficiently close to white noise. Those points in the complete data set (including the points initially removed) are then rejected for which the probability to be measured given the specified standard deviation is less than a pre-defined

⁵This figure compares favourably with the performance of classical gravimeters. In the absolute measurement done with a FG5 discussed in the following sub-section, 1.5 % of the drops needed to be rejected.

4. Results

value, typically 0.5 %. The data-set from "hopping" is processed similarly, the only difference being that a simple linear fit is deducted to gather the initial set of residuals.

When comparing the values of g produced from the long data-set from above with and without cleaning, a deviation of $\approx 0.5 \text{ nm s}^{-2}$ is obtained, which does not grow significantly for stricter thresholds than the 0.5 % noted above. This result demonstrates that careful consideration of outliers is necessary if the high resolution indicated by the variance of data points without drift is to be exploited.

Systematic Influences

While not yet being the subject of a detailed evaluation, some systematic influences need to be considered. The two estimated to be the most important at the moment are the AC Stark and the Coriolis effect.

As discussed in section 2.1.1, the shift in ground level energy caused by a (largely suppressed) coupling to the intermediate level during Raman pulses can be made equal for both transitions and thus effectively cancelled by choosing an appropriate ratio $I_{23}/I_{13} \approx 2$ of the intensities of the Raman beams. However, for some technical reasons the ratio was set to unity, which unfortunately causes a substantial shift in the interferometer phase. As detailed in [70] the erroneous shift can be estimated to cause a deviation in g of $-800 \pm 100 \text{ nm s}^{-2}$.

Presumably, the most important systematic is connected to the sensitivity to Coriolis forces of the interferometer. In analogy to light interferometer enclosing a finite area between the two arms (Sagnac effect) an atom gravimeter becomes susceptible to rotations if the trajectories of the two wave-packets do not follow the same space-curve. The resulting phase shift can be expressed as [107]

$$\Delta\phi_{\text{sag}} = \frac{2m}{\hbar} \boldsymbol{\Omega} \cdot \mathbf{A} \quad (4.6)$$

where \mathbf{A} denotes the oriented area enclosed by the interferometer and $\boldsymbol{\Omega}$ the angular velocity. In a fountain set-up, the area is due to the recoil splitting along with small lateral velocity components unavoidable with atomic samples of finite temperature. As there is a broad range of possible velocities, the effective area depends on the lateral position difference of the cloud during launch and detection and thus can be reduced by appropriate alignment.

For the actual implementation a maximal horizontal deviation of 4 mm

is derived from centring the cloud during up- and downward propagation through the detection area, leading to $v_{\text{lat}} = 5.2 \times 10^3 \text{ m/s}$ for typical interferometer timings. With $\mathbf{A} = (\mathbf{v}_{\text{lat}} \times \frac{\hbar}{m} \mathbf{k}_{\text{eff}}) T^2$ the maximal possible deviation in g can be written as

$$\Delta g_{\text{sag}} = 2\Omega v_{\text{lat}} \quad (4.7)$$

for a given angular velocity. Here Earth's rotation is of biggest concern, leading to a latitude-dependent rotation rate of $\Omega_{\oplus} \cos \alpha$, which for Berlin amounts to $4.4 \times 10^{-5} \text{ rad/s}$. Correspondingly, a maximal error in g of 460 nm s^{-2} is to be expected.

In future measurements this can be rectified either by better vertically aligning launch and detection, averaging over different orientations of the experiment or actively compensating for Earth's rotation. The second method is connected to moving the whole apparatus which would introduce unwanted tilts. The first method is best implemented by zeroing the effect of controlled rotations [48]. This necessitates either the ability to rotate the fountain set-up—which is impractical—or only the set of Raman beams, best done by accurately tilting the corresponding optics. Given the capability to do the latter, it is also possible to actively compensate for the precisely known angular motion of Earth during each shot; a method proposed by the group of Mark Kasevich in Stanford (USA). As this approach seems to be the most reliable and also the most convenient in field applications, the development of an adequate sub-system is currently under-way. Furthermore fine-tuning of beam verticality becomes straight-forward once this functionality is available.

4.2.1. Comparison With FG5

Made possible by the kind support of the Bundesamt für Kartographie und Geodäsie, the laboratory in Adlershof could be connected to the gravity reference net in Germany⁶ in September 2010 [109]. An absolute measurement with the FG5 #101 from Micro-g LaCoste Inc. was done in a laboratory on ground floor (room 0'701) in the physics department. Several other rooms—including 0'703, where the measurement with the atom gravimeter took place—were related to this point with the help of relative gravimeters CG5 from Scintrex Ltd. Furthermore, gravity gradients in all these places were determined.

⁶Deutsches Schweregrundnetz 1994 (DSGN 94) [108]

4. Results



Figure 4.7.: Pictures taken during absolute gravimetric measurements in late 2010 at the physics department of the Humboldt Universität zu Berlin with the atom gravimeter (**left**) and the FG5 (**right**).

This enabled the direct comparison of the performance of both gravimeters. In figure 4.8 the residuals of both measurements after correction for tides are plotted, from which it is apparent that the atom interferometer features a substantially better resolution. Due to the much lower noise floor, the precision attainable in a given time exceeds that of the FG5 by a factor ≈ 8 . This is partly due to the fact, that the corner cube gravimeter performs a drop every 6 s, and does so for only 15 min every hour in order to preserve the instrument. In contrast, the atom gravimeter takes a data point every 1.4 s, which gives a ratio of ≈ 17 in the effective repetition rate, explaining a factor of 4 in the measured noise. Still, the resolution obtained per drop is almost doubled for the atom interferometer.

As a related note a remark concerning the observed noise level is cited from [109], which states that due to the vicinity to Berlin a relatively high level of microseisms—presumably caused by traffic—is present. This leads to a standard deviation in measured g values which is 50 % higher than what can be achieved in quieter locations. A similar improvement might

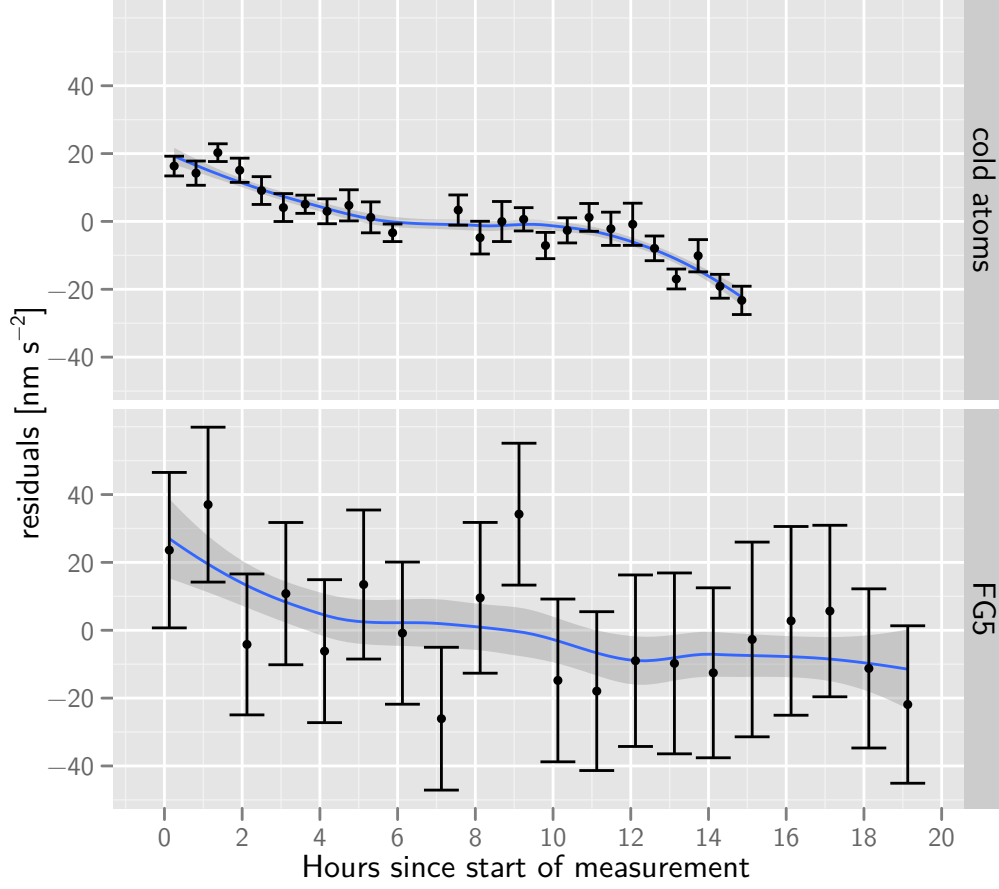


Figure 4.8.: Comparison of the residuals from long-term measurements from atom gravimeter (**top**) and a state-of-the-art classical instrument (FG5 #101, **bottom**). Lines are fitted LOESS smoother.

be expected for the atom gravimeter as the observed noise is connected mostly to residual vibrations.

It is also visible from the data that both instruments suffer from similar drifts, with the difference that this effect can much more easily be assessed for the atom interferometer. Indeed, the observed drift has not been treated separately in the analysis of the data collected with the FG5 by the authors of [109]. Thus the increased resolution will allow for easier characterization of systematic influences, hopefully leading to sizeable gains in performance.

To complete the analysis, a comparison of the obtained values for local gravity is presented in table 4.1. For convenience, the systematic

4. Results

effect	mag. [nm s^{-2}]	uncertainty		remarks
		stat.	syst.	
g (cold atoms)	9812640796	4	7	syst. uncert. mostly from barometric data
grav. of set-up	-19		1	
MOT switching	-10		20	
AC Stark	800		100	
verticality	0		220	
Sagnac	0		460	
sum	9812641567	4	520	
g (FG5) @ 1.25 m	-9812641390	18	15	
height	403	3	31	
other room	-320	30	94	± 3 cm in floor level
seasons	0		200	estimate from [109]
total	260	36	566	

Table 4.1.: Measured values and applied corrections from the comparison of the atom gravimeter with a FG5. The bottom line is the difference with corresponding uncertainties.

effects treated in this thesis for which a value can be assigned are included, despite the lack of importance of some at the current level of accuracy.

Again, the lower statistical uncertainty for the atom gravimeter is apparent. In contrast, the uncertainty of systematic influences is higher by a factor of 35, underlining the relevance of ongoing efforts to evaluate and suppress their effects.

The value for local gravity obtained with the atom gravimeter agrees with the one given in the framework of the official German gravity reference net within 260 nm s^{-2} , equivalent to a fraction of 2.3×10^{-8} in g . The difference is well covered by the combined uncertainty of 570 nm s^{-2} of the estimated systematics. It can be hoped for that by suppressing the three most prominent of these effects—AC Stark, verticality and Sagnac, accounting for 92 % of the total uncertainty—a substantial better performance can be achieved. As a remedy is clearly foreseeable for each of them, fast progress is to be expected.

5. Conclusion and Outlook

The atom interferometer described in this thesis is an ongoing effort to implement the functionality of an absolute gravimeter in a moveable set-up rugged enough for regular deployment in the field, thus pushing matterwave optics into the realm of "real world" applications. Albeit development was started from scratch, the performance demonstrated so far exceeds that of classical instruments by almost an order of magnitude and compares favourably with less mobile atom interferometers [48, 59] in respect to the obtainable resolution. This, together with the ability to measure side-by-side with the best available gravimeters at quiet sites, will help greatly in the oncoming task of identifying and suppressing the influence of systematic effects.

Several steps are scheduled for the near future to address the most important of the issues encountered recently. These will include in-depth characterization of the Raman optics, a magnetic shield encapsulating the complete fountain set-up, the ability to remotely control the tilt of the Raman beams with micro-rad resolution, and various improvements to the laser system (intensity stabilization, lock reliability, thermal regulation, better characterization of the master laser). It is anticipated that the atom interferometer will then show significantly reduced susceptibility to external influences and a better control of systematic effects, enabling absolute gravity measurements competitive with other state-of-the-art instruments.

Future generations of atom gravimeters will certainly aim at vastly reduced package sizes. Recent developments in compact interferometer designs [110] as well as miniaturized laser systems [111] offer the prospect of a new class of instruments which deliver the performance of today's devices in one hundredth of the volume and smaller, with greatly lowered power demands. This will open new fields of applications, where similar systems are installed as permanent sensors close to geologically active areas, or are part of large-scale precision mapping of gravity in airborne missions. The latter was mentioned being particularly urgent in dialogues with the geodetic community, as conventional instruments based on spring systems suffer from lengthy settling times following disturbances frequently found

5. Conclusion and Outlook

on low-altitude trajectories. Here, the ability to rapidly prepare and deploy a new sample of cold atoms will aid greatly in achieving superior availability, thereby enabling far better coverage of the area to be investigated.

A field which will benefit far more than others from miniaturization are satellite missions aimed at improving geoid reference systems and global surveillance. Two projects of the recent past—GRACE and GOCE—have demonstrated the enormous potential of gravitational mapping from low orbits and have triggered interest in follow-up missions. Atom interferometers have been proposed as the core sensing technology in such missions, as they promise better performance in a leaner package. Accordingly, first steps are under-way to investigate suitable designs [112, 113].

The greatly extended times of free evolution possible in micro-gravity will also serve fundamental research. Tests of the weak equivalence principle could be carried out with an interferometer very similar to that described in this thesis, but with two atomic species interrogated at the same time. Differential measurements together with pulse spacings T in the order of several seconds would lead to a strongly enhanced sensitivity to minuscule deviations from the universality of free fall, and could provide for tests orders of magnitude more stringent than the best alternatives available today [114].

Another important improvement would be to implement continuous measurements, that is without temporal gaps during shots. This could be achieved by preparing a cloud of atoms while measuring with another, either in a juggling scheme or by parallel operation of multiple instruments. The benefit would be in avoiding aliasing effects and an extension of the dynamic range of the sensor. With high enough repetition rates to cover all vibrational frequencies of concern, the requirements for vibration isolation could be relaxed considerably or avoided all together, allowing for significantly reduced complexity of the instrument.

The ultimate goal is to combine these aspects in a device capable of vector measurements of g , that is determination of all three spatial components of the experienced acceleration in a continuous and robust fashion. As many test masses are available in a cloud of laser cooled atoms, such measurements could happen simultaneously on distinct sets. The components would need to be separated either spatially through large coherently transferred momenta, or in the frequency domain by addressing different species, isotopes or resonances, in order to distinguish between the three directions. Instruments able to perform such measurements would allow for accurate mapping of gravity independent of orientation on air-

borne or seaboard platforms, thus greatly extending the possibilities of today.

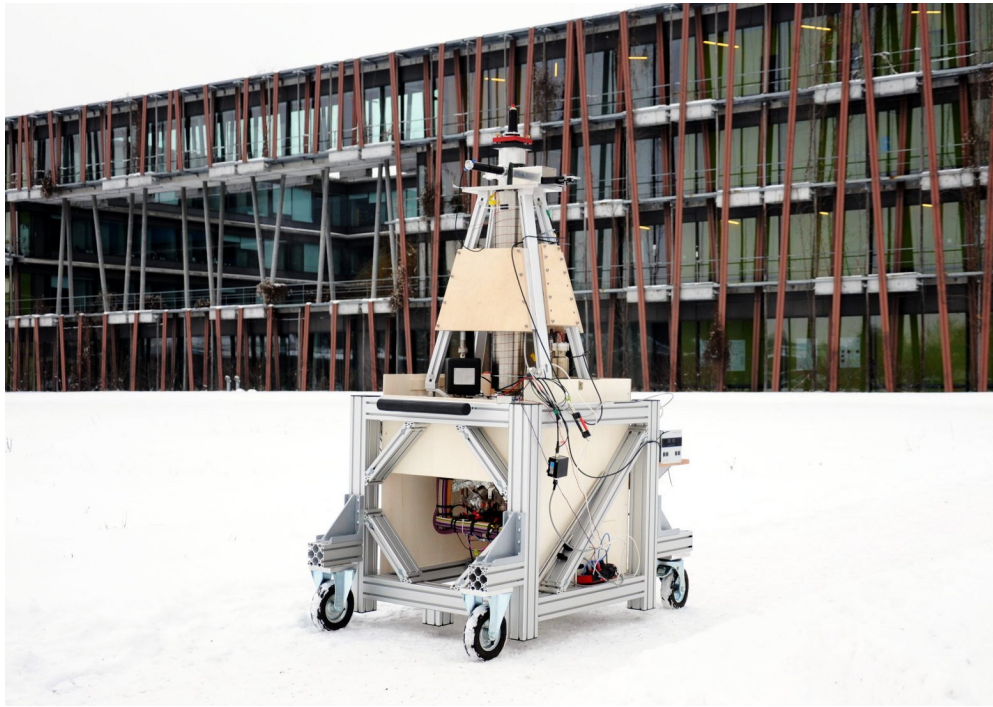


Figure 5.1.: Today, atom interferometers are still a rare species, seldomly spotted in the wild.

A. Details of Long-Term Gravity Measurement

Below the coordinates of the location as well as the parameters for the applied corrections to measured gravity are given.

Room 0'703, HU Berlin, Newtonstr. 15, 12489 Berlin
 Lat.: 52.43337° N, Long.: 13.53062° E, Alt.: 35.3 m
 Gradient: $-3130(30) \text{ nm s}^{-2}/\text{m}$ [109].

date	x ["]	y ["]	UT1-UTC [s]	LOD [s]
2010-12-05	0.188286	0.234123	-0.1249488	0.0004559
2010-12-06	0.186375	0.232474	-0.1253616	0.0004147

Table A.1.: Corrections for location of the pole and changes to daytime, given by the IERS [81]

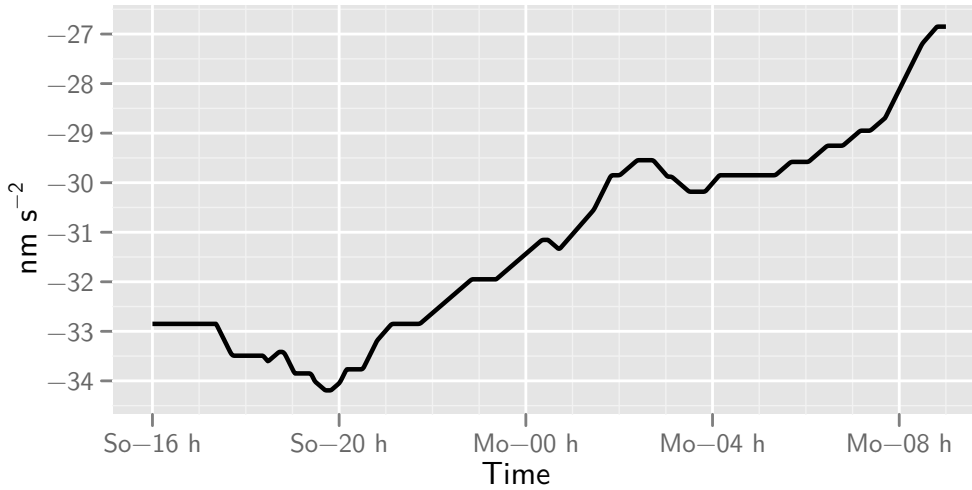


Figure A.1.: Applied correction due to deviations from nominal air pressure of 1008.85 hPa; admittance factor: $3 \text{ nm s}^{-2}/\text{hPa}$.

A. Details of Long-Term Gravity Measurement

tide symbol	period	rel. amplitude	phase [rad]
long-period			
mean	> 400 d	1.15800	0
Mf	13.66 d	1.15790	0
diurnal			
Q1	26.87 h	1.15430	0
O1	25.82 h	1.15431	0
P1	24.07 h	1.14906	0
K1	23.93 h	1.13440	0
ψ 1	23.87 h	1.27309	0
φ 1	23.8 h	1.17080	0
OO1	22.25 h	1.15638	0
semidiurnal			
mean	13.93to10.96 h	1.16201	0
thirddiurnal			
M3	8.26 h	1.07361	0
quarterdiurnal			
M4	6.19 h	1.03900	0

Table A.2.: Response factors of solid Earth to the most important celestial tides as predicted by [83] using the model of [75].

tide symbol	period	ampl. [nm s^{-2}]	phase [rad]
long-period			
Ssa	182.6 d	0.6	-0.059
Mm	27.55 d	-0.6	-0.358
Mf	13.66 d	-0.93	-0.482
diurnal			
Q1	26.87 h	-0.46	-2.78
O1	25.82 h	-1.51	2.81
P1	24.07 h	-0.59	0.94
K1	23.93 h	-1.83	0.94
semidiurnal			
N2	12.63 h	-2.22	1.79
M2	12.39 h	-9.47	1.34
S2	11.97 h	-3.49	0.76
K2	11.93 h	-0.86	0.94

Table A.3.: Effect of ocean loading at the measurement site, provided by [84]

B. Aluminium Knife-Edge Seal

Industrial standards to achieve UHV-compatible bonding of optical flats to metal view-ports are brazing and welding, techniques not readily accessible in most laboratories. Custom approaches are mostly based on glueing or "soft" metal seals. The former utilizes chemically hardening resins, which are conveniently handled, do not introduce any stress onto the window and can achieve high bake-out-temperatures ($> 300\text{ }^{\circ}\text{C}$ in [115]) for suitable materials. However, they are not in wide-spread use which seems mostly connected to issues of ageing and cracking under dynamic loads.

In contrast, the latter technique benefits from the very forgiving mechanical properties many metals exhibit. When put under large enough compressive stress, the material starts to become ductile and flows in a form given by the distribution of the load and constraints formed by the general geometry of the surrounding. This way the metal can form an exact counterpart of adjacent surfaces and thus a leak-tight seal. When the stress drops under a certain level—which may happen because the metal deformed to such extent, that the stress-exerting process ran out of energy—a stable situation is regained, where the deformed metal part does not alter significantly, if not being objected to stresses similar to those experienced in the first place.¹ As metals accept rather large stress before plastic deformation happens and as even in such cases they are less susceptible to cracking than e. g. hardened resins, more reliable seals are the result.

The most commonly used metal is indium, due to the peculiar combination of very low compressive strength of only 2 MPa and low vapour pressure at room temperatures. Indeed, highly reliable UHV-seals of glass to metal are formed with only little pressure needed [96], allowing for thin and brittle windows. Additional benefits are the easy handling² as well as

¹The exact magnitude of stress necessary to induce further deforming is not easily predictable. This comes as the process is highly non-linear and depends on many parameters, not the least the kind of metal put under load. Both higher and lower limits than before are possible, depending on the alterations to the crystal structure of the deformed part.

²In the cited reference a rather involved procedure is described to obtain the bonding.

B. Aluminium Knife-Edge Seal

the glass-wetting property of indium, which leads to strong adhesion and thus further increases the reliability of the seal.

Main drawback is the low melting point of 157 °C, which puts an inconvenient limit on bake-out-temperatures. Further points are the comparatively high price, which might rise significantly in the near future, and the difficult process of disassembling the window from the viewport, due to mentioned adhesion. The latter often leads to the loss of the window, further increasing the economic load.

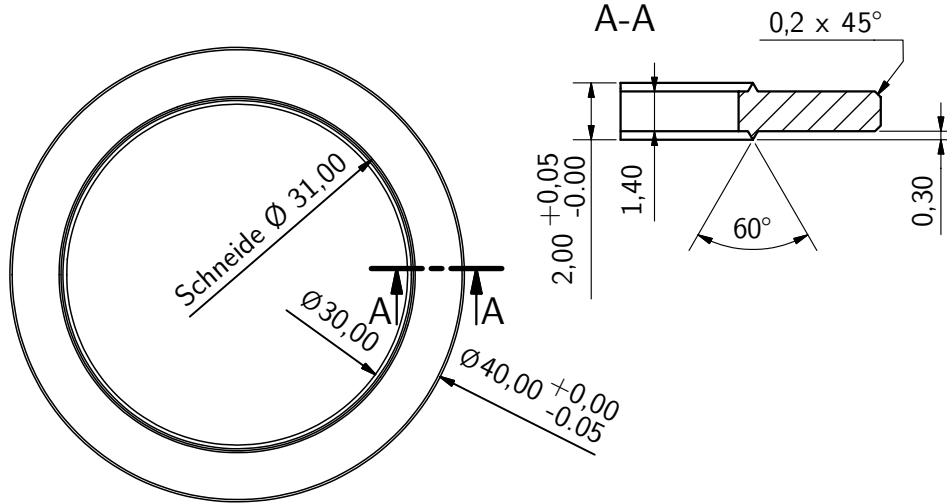


Figure B.1.: Outer dimensions of and cut through an UHV compatible window-seal made from aluminium. A knife-edge is milled symmetrically to both sides of an aluminium ring, which is placed between vacuum chamber and window. By applying a large enough load to the window, the edge is crushed and forms a tight closure with adjacent surfaces.

Several methods have been developed to address these problems. The most common are to use lead or indium alloys [116] to increase the melting point, or to use a slightly different approach based on knife-edges milled to a ring of copper [117]. Both approaches yield the desired result of raising achievable bake-out temperatures, but at the price of significantly higher loads to be applied to the seal and consequently to the window. This makes these techniques error-prone, either by increasing the danger of possible leaks when being too gentle, or by breaking windows in the attempt to form a reliable connection. However, successful sealing with either method

In practice, very simple methods as pressing the window into a bed of indium are generally sufficient.

has been demonstrated, albeit accompanied by a pronounced increase in labour needed in the process.

Another potential candidate for the metallic sealant is pure aluminium. It combines a low price per volume with a sufficiently high melting point of 660 °C and a yield strength³ of 10 – 20 MPa. Copper has a yield strength of ≈ 80 MPa in cast form, which drops to ≈ 40 MPa when annealed. Furthermore the shear modulus compares as 25.5 GPa for aluminium to 44.7 GPa for copper, and the ultimate strength as ≈ 55 MPa to 220 MPa (annealed copper). The last quantity gives the highest possible stress on the stress-strain-curve in tension and could be described as the ultimate resistance of the material to deformation.⁴

While a reliable prediction of the ductile behaviour of the sealant is impossible from these numbers alone, it becomes apparent, that far lesser stresses will be needed to reach a certain deformation with aluminium than with copper. When exploiting the same trick as Noble et al. in [117], that is to restrain the volume to be deformed to a fine knife-edge as depicted in figure B.1, very low clamping forces are needed.

In a test with a window of 40 mm outer diameter and a clear aperture of $\varnothing 30$ mm, the torque needed on four M6 screws fixating the window cap (compare figure 3.3) to achieve a nominal reduction in height of 0.6 mm was < 5 Nm. In comparison, the same torque is needed to compress an indium wire of $\varnothing 1$ mm to a width of 4 mm in order to form a good seal. For copper a torque three to four times as high was needed. The obtained seal was helium leak-tested to give an upper bound on the leakage-rate of 10^{-11} hPaL/s, which is sufficient to reach UHV, even if some ten windows are attached to the vacuum chamber.

A problem arises from the pronounced dependency of the mechanical properties of aluminium on temperature as depicted in figure B.2. If a simple symmetric constellation is chosen as suggested in [117], that is the aluminium ring is paired with a similar one on the opposing side of the window covered by the window cap, the increased yielding of the sealant at high bake-out temperatures results in leaks after cool-down. This comes as the energy stored in slight elastic deformations of the window cap is almost completely used for plastic deformation of the softened aluminium

³Defined as the stress at which plastic deformation begins to occur. As this is not very precise for real materials, often (and here) the definition of the stress which leads to a permanent elongation of 0.2 % after removing the load, is adopted.

⁴The failure mode for tension stress is not necessarily the same as for compression. However, a similar definition for compression loads is not available. To compare both materials, a regress to this characteristic is necessary.

B. Aluminium Knife-Edge Seal

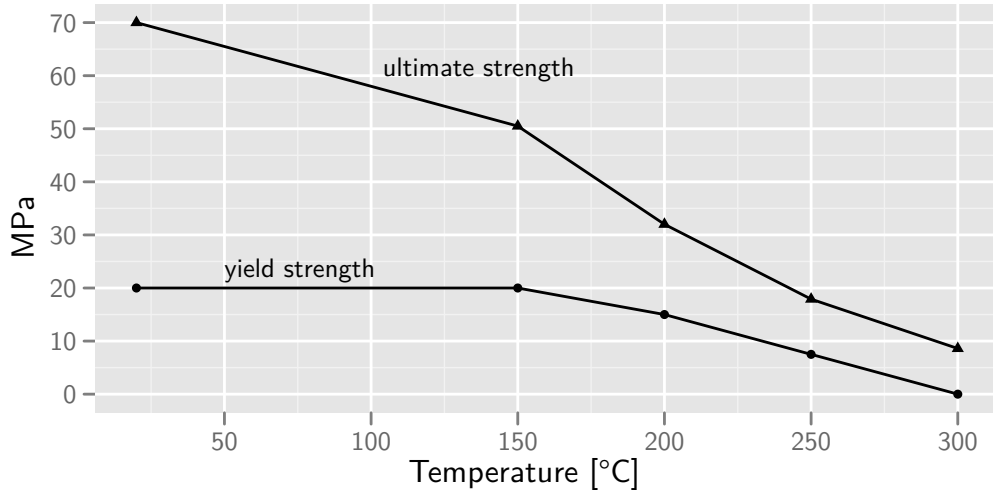


Figure B.2.: Mechanical properties of aluminium at elevated temperatures (from [118]). Please note that the value of 70 MPa for the ultimate strength at 20 °C is consistent with the values stated in the text. This quantity varies strongly with the purity of the material. The cited value is typical for 99.6 % purity, which is at the lower end of commercially available qualities. In contrast, highly pure samples ($> 99.9\%$) feature ultimate strengths of ≈ 45 MPa.

knife-edges during baking. When the aluminium shrinks in the cool-down process, the remaining pressure exerted by the window cap is insufficient to maintain good vacuum conditions.

This can be rectified by pairing the aluminium sealant with a ring featuring large elastic excursion on the outside of the window. The task is somewhat tricky, as purely elastic deformation of > 0.5 mm is needed, when taking machining tolerances into account. The ring should furthermore keep its elastic properties even for temperatures considerably higher than maximal bake-out temperature of ≈ 200 °C. The counterpart should lastly not be overly large, in order to keep overall dimensions reasonable.

A suitable approach is drawn in figure B.3. The material of choice is titanium alloy TiAl6V4 (also known as titanium grade 5). This alloy is common e.g. in aeronautics, as it does not show significant changes in properties for temperatures up to 500 °C and features high yield strengths of ≈ 1100 MPa. The geometry is optimized for both: relatively easy machining and large elastic deflections. The latter quality is illustrated in figure B.4 for an axial load of 270 N per centimetre of the inner diameter.

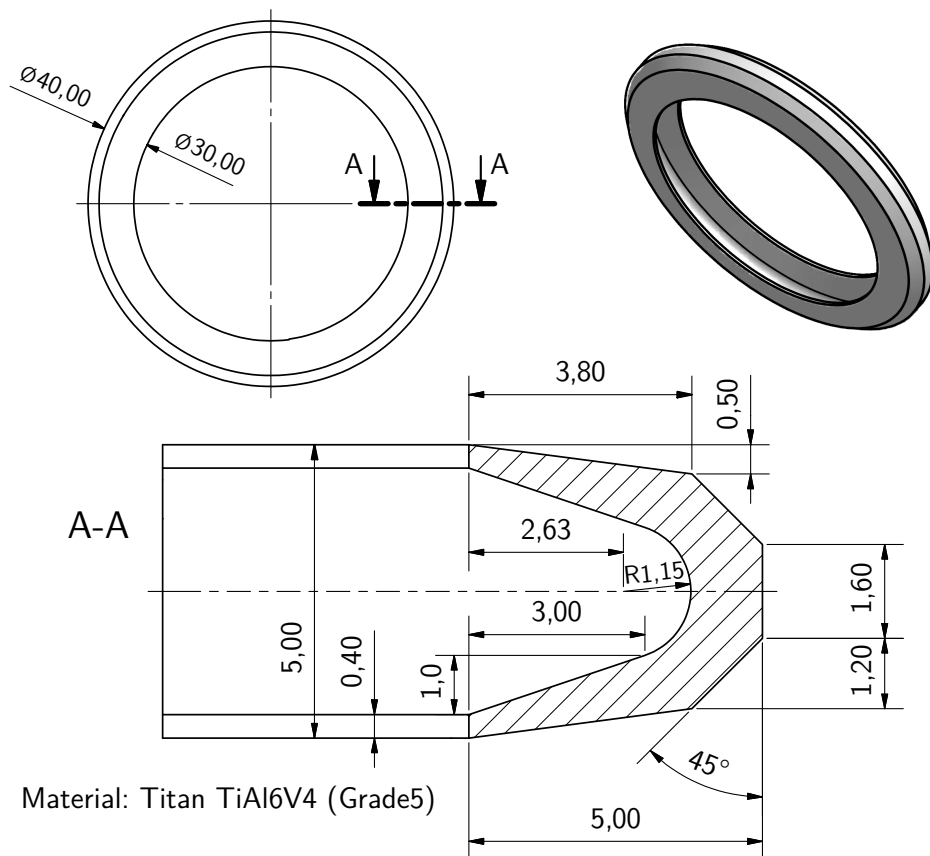


Figure B.3.: Spring designed to give high purely elastic deflection at high loads, and to withstand elevated temperatures.

B. Aluminium Knife-Edge Seal

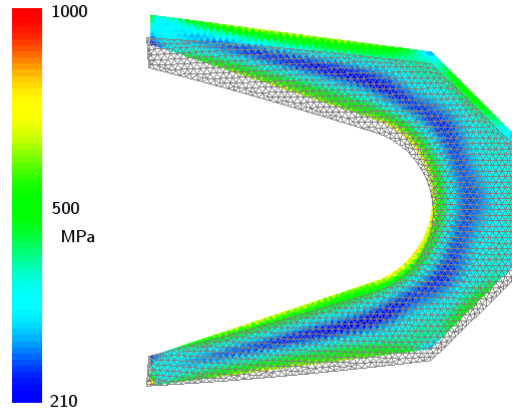


Figure B.4.: Deflection and von-Mises-stress for axial loading (2.5 kN), as obtained from FEM calculations. The uniform colouring of the rims suggests, that the design is fairly optimal. No points with excessive stress are found, which would fail early. Neither are large areas left with significantly lower stress (except for the inner part, close to the "neutral fibre"), which could contribute to further bending if suitably loaded. As the calculated stress is well below the yield strength, fully elastic behaviour can be expected. The grey mesh shows the real (not scaled) deflection.

The height of the window cap is to be chosen so, that when the stack knife-edge-ring-window-elastic ring-window cap is put in its appropriate place onto the vacuum chamber, an air gap of 1 mm between cap and body of the vacuum chamber is left. By simply bolting down the cap to the chamber, the knife edge is crushed and the elastic ring is loaded to their nominal degrees. This procedure does not need to be applied with great care (only a roughly uniform tightening of the screws to avoid that the window gets jammed inside the cap), as the elastic ring will even out point loads, which might otherwise impair the window. After good contact between cap and chamber is established, all screws can be firmly tightened. This way, the window cap is a suitable base for further attachments, without the need to worry about undue loads applied to the window.

Following this simple recipe, helium leak-tight seals are obtained, which were tested to rates below 10^{-11} hPaL/s before and after rapid baking cycles (max 200 °C, heating and cooling rates of > 40 °C/h). No window broke during numerous assemblies, and sealing was reliable, if large enough initial air gaps were chosen. Still more testing is needed, as only a few full baking cycles have been done due to tight schedules.

It was learned only during the last tests, that the very low torques needed with indium wires are sufficient to obtain good seals with the aluminium knife-edges. However, the elastic ring is designed with higher reserves in mind, exceeding the needed stress by approximately a factor of 3. Adjusting the air gap so, that only torques of 5 Nm were needed to achieve full contact between cap and supporting flange, indeed resulted in leak-tight closures. However, the deflection of the elastic ring was too small to guarantee adequate loading even after the baking cycle. Instead, leak rates in the order of 10^{-8} hPaL/s were observed, which are not acceptable. Future design efforts will aim at lowering the load needed to achieve a deflection in the elastic ring comparable to the one depicted in figure B.4. This is only a question of suitable reduction of wall thickness and some minor adjustments to the geometry, and should not pose any larger problem.

Bibliography

- [1] T. Hänsch and A. Schalow. Cooling of gases by laser radiation. *Optics Communications*, 13(1):68–69, January 1975.
- [2] S. Chu, L. Hollberg, J. Bjorkholm, A. Cable, and A. Ashkin. Three-dimensional viscous confinement and cooling of atoms by resonance radiation pressure. *Physical Review Letters*, 55(1):48–51, July 1985.
- [3] E. Raab, M. Prentiss, A. Cable, S. Chu, and D. Pritchard. Trapping of Neutral Sodium Atoms with Radiation Pressure. *Physical Review Letters*, 59(23):2631–2634, December 1987.
- [4] L. de Broglie. *Recherches sur la théorie des quanta*. Thesis, 1924.
- [5] C. Davisson and L. Germer. Diffraction of Electrons by a Crystal of Nickel. *Physical Review*, 30(6):705–740, December 1927.
- [6] E. Rupp. Versuche über Elektronenbeugung am optischen Gitter. *Die Naturwissenschaften*, 16(33):656–656, August 1928.
- [7] W. Zinn. Diffraction of Neutrons by a Single Crystal. *Physical Review*, 71(11):752–757, June 1947.
- [8] I. Estermann and O. Stern. Beugung von Molekularstrahlen. *Zeitschrift für Physik*, 61(1-2):95–125, January 1930.
- [9] I. Estermann and O. Stern. Beugung von Molekularstrahlen. *Zeitschrift für Physik*, 61(1-2):95–125, January 1930.
- [10] M. Chapman, C. Ekstrom, T. Hammond, R. Rubenstein, J. Schmiedmayer, S. Wehinger, and D. Pritchard. Optics and Interferometry with Na₂ Molecules. *Physical Review Letters*, 74(24):4783–4786, June 1995.
- [11] M. Arndt, O. Nairz, J. Vos-Andreae, C. Keller, G. van der Zouw, and A. Zeilinger. Wave-particle duality of C₆₀ molecules. *Nature*, 401(6754):680–682, October 1999.

Bibliography

- [12] S. Gerlich, S. Eibenberger, M. Tomandl, S. Nimmrichter, K. Hornberger, P. Fagan, J. Tüxen, M. Mayor, and M. Arndt. Quantum interference of large organic molecules. *Nature Communications*, 2: 263, March 2011.
- [13] L. Marton. Electron Interferometer. *Physical Review*, 85(6):1057–1058, March 1952.
- [14] H. Rauch, W. Treimer, and U. Bonse. Test of a single crystal neutron interferometer. *Physics Letters A*, 47(5):369–371, 1974.
- [15] M. Kasevich and S. Chu. Atomic interferometry using stimulated Raman transitions. *Physical Review Letters*, 67(2):181–184, July 1991.
- [16] F. Riehle, T. Kisters, A. Witte, and J. Helmcke. Optical Ramsey spectroscopy in a rotating frame: Sagnac effect in a matter-wave interferometer. *Physical Review Letters*, 67(2):177–180, July 1991.
- [17] O. Carnal and J. Mlynek. Young’s double-slit experiment with atoms: A simple atom interferometer. *Physical Review Letters*, 66(21):2689–2692, May 1991.
- [18] D. Keith, C. Ekstrom, Q. Turchette, and D. Pritchard. An interferometer for atoms. *Physical Review Letters*, 66(21):2693–2696, May 1991.
- [19] A. Cronin, J. Schmiedmayer, and D. Pritchard. Optics and interferometry with atoms and molecules. *Reviews of Modern Physics*, 81(3):1051–1129, July 2009.
- [20] C. Bordé. Atomic interferometry with internal state labelling. *Physics Letters A*, 140(1-2):10–12, September 1989.
- [21] M. Chapman, T. Hammond, A. Lenef, J. Schmiedmayer, R. Rubenstein, E. Smith, and D. Pritchard. Photon Scattering from Atoms in an Atom Interferometer: Coherence Lost and Regained. *Physical Review Letters*, 75(21):3783–3787, November 1995.
- [22] L. Hackermüller, K. Hornberger, B. Brezger, A. Zeilinger, and M. Arndt. Decoherence of matter waves by thermal emission of radiation. *Nature*, 427(6976):711–4, February 2004.

- [23] K. Zeiske, G. Zinner, F. Riehle, and J. Helmcke. Atom interferometry in a static electric field: Measurement of the Aharonov-Casher phase. *Applied Physics B Laser and Optics*, 60(2-3):205–209, 1995.
- [24] C. Webb, R. Godun, G. Summy, M. Oberthaler, P. Featonby, C. Foot, and K. Burnett. Measurement of Berry’s phase using an atom interferometer. *Physical Review A*, 60(3):R1783–R1786, September 1999.
- [25] C. Ekstrom, J. Schmiedmayer, M. Chapman, T. Hammond, and D. Pritchard. Measurement of the electric polarizability of sodium with an atom interferometer. *Physical Review A*, 51(5):3883–3888, May 1995.
- [26] A. Morinaga, T. Tako, and N. Ito. Sensitive measurement of phase shifts due to the ac Stark effect in a Ca optical Ramsey interferometer. *Physical Review A*, 48(2):1364–1368, August 1993.
- [27] C. Degenhardt, H. Stoeck, U. Sterr, F. Riehle, and C. Lisdat. Wavelength-dependent ac Stark shift of the $^1S_0 - ^3P_1$ transition at 657nm in Ca. *Physical Review A*, 70(2), August 2004.
- [28] V. Druzhinina and M. DeKieviet. Experimental Observation of Quantum Reflection far from Threshold. *Physical Review Letters*, 91(19), November 2003.
- [29] J. Perreault and A. Cronin. Observation of Atom Wave Phase Shifts Induced by Van Der Waals Atom-Surface Interactions. *Physical Review Letters*, 95(13), September 2005.
- [30] A. Wicht, J. Hensley, E. Sarajlic, and S. Chu. A Preliminary Measurement of the Fine Structure Constant Based on Atom Interferometry. *Physica Scripta*, T102(1):82, 2002.
- [31] P. Cladé, E. de Mirandes, M. Cadoret, S. Guellati-Khélifa, C. Schwob, F. Nez, L. Julien, and F. Biraben. Precise measurement of h/m_{Rb} using Bloch oscillations in a vertical optical lattice: Determination of the fine-structure constant. *Physical Review A*, 74(5), November 2006.
- [32] S. Fray, C. Diez, T. Hänsch, and M. Weitz. Atomic Interferometer with Amplitude Gratings of Light and Its Applications to Atom Based Tests of the Equivalence Principle. *Physical Review Letters*, 93(24), December 2004.

Bibliography

- [33] A. Kellerbauer, M. Amoretti, A. Belov, G. Bonomi, I. Boscolo, R. Brusa, M. Buchner, V. Byakov, L. Cabaret, and C. Canali. Proposed antimatter gravity measurement with an antihydrogen beam. *Nuclear Instruments and Methods in Physics Research Section B: Beam Interactions with Materials and Atoms*, 266(3):351–356, February 2008.
- [34] T. Heupel, M. Mei, M. Niering, B. Gross, M. Weitz, T. Hänsch, and C. Bordé. Hydrogen atom interferometer with short light pulses. *European Physics Letters (EPL)*, 57(2):158–163, January 2002.
- [35] S. Dimopoulos, P. Graham, J. Hogan, and M. Kasevich. General relativistic effects in atom interferometry. *Physical Review D*, 78(4), August 2008.
- [36] C. Jentsch, T. Müller, E. M. Rasel, and W. Ertmer. HYPER: A Satellite Mission in Fundamental Physics Based on High Precision Atom Interferometry, 2004.
- [37] S. Dimopoulos, P. Graham, J. Hogan, M. Kasevich, and S. Rajendran. Gravitational wave detection with atom interferometry. *Physics Letters B*, 678(1):37–40, July 2009.
- [38] A. Peters, K.-Y. Chung, and S. Chu. Measurement of gravitational acceleration by dropping atoms. *Nature*, 400(6747):849–852, August 1999.
- [39] H. Müller, A. Peters, and S. Chu. A precision measurement of the gravitational redshift by the interference of matter waves. *Nature*, 463(7283):926–9, February 2010.
- [40] J. Hammond and J. Faller. Results of Absolute Gravity Determinations at a Number of Different Sites. *Journal of Geophysical Research*, 76(32):7850–7854, 1971.
- [41] M. Zumberge, R. Rinker, and J. Faller. A Portable Apparatus for Absolute Measurements of the Earth’s Gravity. *Metrologia*, 18(3):145–152, July 1982.
- [42] R. Colella, A. Overhauser, and S. Werner. Observation of Gravitationally Induced Quantum Interference. *Physical Review Letters*, 34(23):1472–1474, June 1975.

- [43] T. Gustavson, A. Landragin, and M. Kasevich. Rotation sensing with a dual atom-interferometer Sagnac gyroscope. *CLASSICAL AND QUANTUM GRAVITY*, 17(12):2385–2398, 2000.
- [44] J. McGuirk, G. Foster, J. Fixler, M. Snadden, and M. Kasevich. Sensitive absolute-gravity gradiometry using atom interferometry. *Physical Review A*, 65(3), February 2002.
- [45] C. Jekeli. Precision Free-Inertial Navigation with Gravity Compensation by an Onboard Gradiometer. *Journal of Guidance, Control, and Dynamics*, 29(3):704–713, May 2006.
- [46] J. Fixler, G. Foster, J. McGuirk, and M. Kasevich. Atom interferometer measurement of the newtonian constant of gravity. *Science (New York, N.Y.)*, 315(5808):74–7, January 2007.
- [47] G. Lamporesi, A. Bertoldi, L. Cacciapuoti, M. Prevedelli, and G. Tino. Determination of the Newtonian Gravitational Constant Using Atom Interferometry. *Physical Review Letters*, 100(5), February 2008.
- [48] A. Peters, K.-Y. Chung, and S. Chu. High-precision gravity measurements using atom interferometry. *Metrologia*, 38(1):25–61, February 2001.
- [49] I. Marson and J. Faller. g -the acceleration of gravity: its measurement and its importance. *Journal of Physics E: Scientific Instruments*, 19(1):23–32, January 1986.
- [50] G. Geneves, P. Gournay, A. Gosset, M. Lecollinet, F. Villar, P. Pinot, P. Juncar, A. Clairon, A. Landragin, D. Holleville, F. Pereira Dos Santos, J. David, M. Besbes, F. Alves, L. Chassagne, and S. Topcu. The BNM Watt Balance Project. *IEEE Transactions on Instrumentation and Measurement*, 54(2):850–853, April 2005.
- [51] J. Goodkind. The superconducting gravimeter. *Review of Scientific Instruments*, 70(11):4131, 1999.
- [52] R. Rummel. Dedicated gravity field missions—principles and aims. *Journal of Geodynamics*, 33(1-2):3–20, March 2002.
- [53] M. Ekman and J. Mäkinen. Recent postglacial rebound, gravity change and mantle flow in Fennoscandia. *Geophysical Journal International*, 126(1):229–234, July 1996.

Bibliography

- [54] G Berrino. Combined gravimetry in the observation of volcanic processes in Southern Italy. *Journal of Geodynamics*, 30(3):371–388, February 2000.
- [55] G. Budetta and D. Carbone. Potential application of the Scintrex CG-3M gravimeter for monitoring volcanic activity: results of field trials on Mt. Etna, Sicily. *Journal of Volcanology and Geothermal Research*, 76(3-4):199–214, April 1997.
- [56] J. Faller. Results of an Absolute Determination of the Acceleration of Gravity. *Journal of Geophysical Research*, 70(16):4035–4038, 1965.
- [57] T. Niebauer, D. Sasagawa, J. Faller, R. Hilt, and F. Klopping. A new generation of absolute gravimeters. *METROLOGIA*, 32(3):159–180, 1995.
- [58] L. Vitushkin, M. Becker, Z. Jiang, O. Francis, T. van Dam, J. Faller, J.-M. Chartier, M. Amalvict, S. Bonvalot, N. Debeglia, S. Desogus, M. Diamant, F. Dupont, R. Falk, G. Gabalda, C. Gagnon, T. Gattacceca, A. Germak, J. Hinderer, O. Jamet, G. Jeffries, R. Kärer, A. Kopaev, J. Liard, A. Lindau, L. Longuevergne, B. Luck, E. Maderal, J. M Kinen, B. Meurers, S. Mizushima, J. Mrlina, D. Newell, C. Origlia, E. Pujol, A. Reinhold, P. Richard, I. Robinson, D. Ruess, S. Thies, M. van Camp, M. van Ruymbeke, M. de Villalta Compagni, and S. Williams. Results of the Sixth International Comparison of Absolute Gravimeters, ICAG-2001. *Metrologia*, 39(5):407–424, October 2002.
- [59] S. Merlet, Q. Bodart, N. Malossi, A. Landragin, F. Pereira Dos Santos, O. Gitlein, and L. Timmen. Comparison between two mobile absolute gravimeters: optical versus atomic interferometers. *Metrologia*, 47(4):L9–L11, August 2010.
- [60] K. Moler, D. Weiss, M. Kasevich, and S. Chu. Theoretical analysis of velocity-selective Raman transitions. *Physical Review A*, 45(1):342–348, January 1992.
- [61] D. Weiss, B. Young, and S. Chu. Precision measurement of h/m_{Cs} based on photon recoil using laser-cooled atoms and atomic interferometry. *Applied Physics B Lasers and Optics*, 59(3):217–256, September 1994.

- [62] C. Bordé and C. Lämmerzahl. Atomic interferometry as two-level particle scattering by a periodic potential. *Annalen der Physik*, 8(1): 83–110, January 1999.
- [63] C. Bordé. Quantum Theory of Atom-Wave Beam Splitters and Application to Multidimensional Atomic Gravito-Inertial Sensors. *General Relativity and Gravitation*, 36(3):475–502, March 2004.
- [64] P. Berman, editor. *Atom interferometry*. Academic Press, 1997. ISBN 978-0-12-092460-8.
- [65] C. Bordé. Outils théoriques pour l’optique et l’interférométrie atomiques. *Comptes Rendus de l’Académie des Sciences - Series IV - Physics*, 2(3):509–530, April 2001.
- [66] C. Antoine. Exact phase shifts for atom interferometry. *Physics Letters A*, 306(5-6):277–284, January 2003.
- [67] B. Dubetsky and M. Kasevich. Atom interferometer as a selective sensor of rotation or gravity. *Physical Review A*, 74(2), August 2006.
- [68] M. Kasevich and S. Chu. Measurement of the gravitational acceleration of an atom with a light-pulse atom interferometer. *Applied Physics B Photophysics and Laser Chemistry*, 54(5):321–332, May 1992.
- [69] J. McGuirk, M. Snadden, and M. Kasevich. Large Area Light-Pulse Atom Interferometry. *Physical Review Letters*, 85(21):4498–4501, November 2000.
- [70] M. Schmidt. *Design, characterization and operation of a mobile high-precision atom interferometer for the measurement of local gravity acceleration*. Dissertation, Humboldt-Universität zu Berlin, 2011.
- [71] C. Lämmerzahl and C. Bordé. Rabi oscillations in gravitational fields: Exact solution. *Physics Letters A*, 203(2-3):59–67, July 1995.
- [72] C. Antoine. Matter wave beam splitters in gravito-inertial and trapping potentials: generalized ttt scheme for atom interferometry. *Applied Physics B*, 84(4):585–597, July 2006.
- [73] P. Storey and C. Cohen-Tannoudji. The Feynman path integral approach to atomic interferometry. A tutorial. *Journal de Physique II*, 4(11):1999–2027, November 1994.

Bibliography

- [74] P. Cheinet, B. Canuel, F. Pereira Dos Santos, A. Gauguier, F. Yver-Leduc, and A. Landragin. Measurement of the Sensitivity Function in a Time-Domain Atomic Interferometer. *IEEE Transactions on Instrumentation and Measurement*, 57(6):1141–1148, 2008.
- [75] V. Dehant, P. Defraigne, and J. Wahr. Tides for a convective Earth. *Journal of Geophysical Research*, 104(B1):1035–1058, 1999.
- [76] F. Lyard, F. Lefevre, T. Letellier, and O. Francis. Modelling the global ocean tides: modern insights from FES2004. *Ocean Dynamics*, 56(5-6):394–415, September 2006.
- [77] J. Merriam. An ephemeris for gravity tide predictions at the nanogal level. *Geophysical Journal International*, 108(2):415–422, February 1992.
- [78] W. Torge. *Geodäsie*. Walter de Gruyter GmbH & Co. KG, 10785 Berlin, 2 edition, 2003. ISBN 3-11-017545-2.
- [79] A. Albertella, F. Migliaccio, and F. Sansó. GOCE: The Earth Gravity Field by Space Gradiometry. *Celestial Mechanics and Dynamical Astronomy*, 83(1):1–15–15, 2002.
- [80] T. Hartmann and H.-G. Wenzel. The HW95 tidal potential catalogue. *Geophysical Research Letters*, 22(24):3553, 1995.
- [81] J. Vondrák and B. Richter. International Earth Rotation and Reference Systems Service (IERS) web: www.iers.org. *Journal of Geodesy*, 77(10-11):585–678, April 2004.
- [82] J. Merriam. Atmospheric pressure and gravity. *Geophysical Journal International*, 109(3):488–500, June 1992.
- [83] M. Vancamp and P. Vauterin. Tsoft: graphical and interactive software for the analysis of time series and Earth tides. *Computers & Geosciences*, 31(5):631–640, June 2005.
- [84] M. Bos and H.-G. Scherneck. Ocean tide loading provider. <http://froste.oso.chalmers.se/loading//index.html>. last visited 2011-05-29.
- [85] A. Peters. *High Precision Gravity Measurements Using Atom Interferometry*. Phd thesis, Stanford University, 1998.

- [86] J. Fils, F. Leduc, P. Bouyer, D. Holleville, N. Dimarcq, A. Clairon, and A. Landragin. Influence of optical aberrations in an atomic gyroscope. *The European Physical Journal D*, 36(3):257–260, September 2005.
- [87] A. Gauguier, B. Canuel, T. Lévêque, W. Chaibi, and A. Landragin. Characterization and limits of a cold-atom Sagnac interferometer. *Physical Review A*, 80(6), December 2009.
- [88] H. Metcalf and P. van Der Straten. *Laser Cooling and Trapping*. Springer, corrected edition, 1999. ISBN 978-0387987286.
- [89] M. Kasevich, D. Weiss, E. Riis, K. Moler, S. Kasapi, and S. Chu. Atomic velocity selection using stimulated Raman transitions. *Physical Review Letters*, 66(18):2297–2300, May 1991.
- [90] D. Steck. Rubidium 87 D Line Data. <http://steck.us/alkalidata>. revision 2.1.2, 12 August 2009.
- [91] A. Kerman, V. Vuletic, C. Chin, and S. Chu. Beyond optical molasses: 3D raman sideband cooling of atomic cesium to high phase-space density. *Physical review letters*, 84(3):439–442, January 2000.
- [92] C. Freier. *Measurement of Local Gravity using Atom Interferometry*. Diplomarbeit, Technische Universität Berlin, 2010.
- [93] J. Le Gouët, T. Mehlstäubler, J. Kim, S. Merlet, A. Clairon, A. Landragin, and F. Pereira Dos Santos. Limits to the sensitivity of a low noise compact atomic gravimeter. *Applied Physics B*, 92(2):133–144, June 2008.
- [94] S. Merlet, J. Le Gouët, Q. Bodart, A. Clairon, A. Landragin, F. Pereira Dos Santos, and P. Rouchon. Operating an atom interferometer beyond its linear range. *Metrologia*, 46(1):87–94, February 2009.
- [95] J. Hensley, A. Peters, and S. Chu. Active low frequency vertical vibration isolation. *Review of Scientific Instruments*, 70(6):2735, 1999.
- [96] H. Saeki. Optical window sealed with indium for ultrahigh vacuum. *Vacuum*, 39(6):563–564, 1989.

Bibliography

- [97] C. Geuzaine and J.-F. Remacle. Gmsh: A 3-D finite element mesh generator with built-in pre- and post-processing facilities. *International Journal for Numerical Methods in Engineering*, 79(11):1309–1331, September 2009.
- [98] X. Baillard, A. Gauguier, S. Bize, P. Lemonde, P. Laurent, A. Clarion, and P. Rosenbusch. Interference-filter-stabilized external-cavity diode lasers. *Optics Communications*, 266(2):609–613, October 2006.
- [99] J. Shirley. Modulation transfer processes in optical heterodyne saturation spectroscopy. *Optics Letters*, 7(11):537, November 1982.
- [100] T. van Zoest, N. Gaaloul, Y. Singh, H. Ahlers, W. Herr, S. Seidel, W. Ertmer, E. Rasel, M. Eckart, E. Kajari, S. Arnold, G. Nandi, W. Schleich, R. Walser, A. Vogel, K. Sengstock, K. Bongs, W. Lewoczko-Adamczyk, M. Schiemangk, T. Schuldt, A. Peters, T. Könnemann, H. Müntinga, C. Lämmerzahl, H. Dittus, T. Steinmetz, T. Hänsch, and J. Reichel. Bose-Einstein condensation in microgravity. *Science (New York, N.Y.)*, 328(5985):1540–3, June 2010.
- [101] M. Schmidt, M. Prevedelli, A. Giorgini, G. Tino, and A. Peters. A portable laser system for high-precision atom interferometry experiments. *Applied Physics B*, 102(1):11–18, October 2010.
- [102] M. Thumm, W. Wiesbeck, and S. Kern. *Hochfrequenzmesstechnik Verfahren und Messsysteme*. Vieweg+Teubner Verlag, Wiesbaden, 2. durchges. edition, 1998. ISBN 978-3-519-16360-2.
- [103] W. Itano, J. Bergquist, J. Bollinger, J. Gilligan, D. Heinzen, F. Moore, M. Raizen, and D. Wineland. Quantum projection noise: Population fluctuations in two-level systems. *Physical Review A*, 47(5):3554–3570, May 1993.
- [104] P. Hobbs. Ultra-quiet high voltage source. *IEEE Transactions on Instrumentation and Measurement*, 38(5):1004–1005, 1989.
- [105] "R Development Core Team". *R: A Language and Environment for Statistical Computing*. R Foundation for Statistical Computing, Vienna, Austria, 2009. ISBN 3-900051-07-0.
- [106] R. McGill, J. Tukey, and W. Larsen. Variations of Box Plots. *The American Statistician*, 32(1):12–16, 1978.

- [107] C. Antoine and C. Bordé. Quantum theory of atomic clocks and gravito-inertial sensors: an update. *Journal of Optics B: Quantum and Semiclassical Optics*, 5(2):S199–S207, April 2003.
- [108] W. Torge, R. Falk, A. Franke, E. Reinhart, B. Richter, M. Sommer, and H. Wilmes. *Das Deutsche Schweregrundnetz 1994 (DSGN94) Band I*. Deutsche Geodätische Kommission, München, b edition, 1999. ISBN 3 7696 8589 X.
- [109] A. Reinhold and R. Falk. Absolute und relative Schweremessungen in der Humboldt-Universität zu Berlin (Campus Adlershof) vom 10.-12.09.2010. Technical report, Bundesamt für Kartographie und Geodäsie, 2011.
- [110] Q. Bodart, S. Merlet, N. Malossi, F. Pereira Dos Santos, P. Bouyer, and A. Landragin. A cold atom pyramidal gravimeter with a single laser beam. *Applied Physics Letters*, 96(13):134101, 2010.
- [111] S. Spießberger, M. Schiemangk, A. Sahm, A. Wicht, H. Wenzel, A. Peters, G. Erbert, and G. Tränkle. Micro-integrated 1 Watt semiconductor laser system with a linewidth of 36 kHz. *Optics Express*, 19(8):7077, March 2011.
- [112] N. Yu, J. Kohel, J. Kellogg, and L. Maleki. Development of an atom-interferometer gravity gradiometer for gravity measurement from space. *Applied Physics B*, 84(4):647–652, July 2006.
- [113] F. Sorrentino, K. Bongs, P. Bouyer, L. Cacciapuoti, M. Angelis, H. Dittus, W. Ertmer, A. Giorgini, J. Hartwig, M. Hauth, S. Herrmann, M. Inguscio, E. Kajari, T. Könemann, C. Lämmerzahl, A. Landragin, G. Modugno, F. Pereira dos Santos, A. Peters, M. Prevedelli, E. Rasel, W. Schleich, M. Schmidt, A. Senger, K. Sengstock, G. Stern, G. Tino, and R. Walser. A Compact Atom Interferometer for Future Space Missions. *Microgravity Science and Technology*, 22(4):551–561, September 2010.
- [114] S. Dimopoulos, P. Graham, J. Hogan, and M. Kasevich. Testing General Relativity with Atom Interferometry. *Physical Review Letters*, 98(11), March 2007.
- [115] C. Muller, M. Barrett, and D. Lowenthal. High-temperature window seals for VUV experiments. *Review of Scientific Instruments*, 59(8):1425, 1988.

Bibliography

- [116] S. Cox, P. Griffin, C. Adams, D. DeMille, and E. Riis. Reusable ultrahigh vacuum viewport bakeable to 240 °C. *Review of Scientific Instruments*, 74(6):3185, 2003.
- [117] A. Noble and M. Kasevich. UHV optical window seal to conflat knife edge. *Review of Scientific Instruments*, 65(9):3042, 1994.
- [118] G. Totten and D. MacKenzie, editors. *Handbook of Aluminum, Vol. 1: Physical Metallurgy and Processes*. CRC Press, 1. edition, 2003. ISBN 978-0824704940.

List of Figures

1.1. Mach-Zehnder Type Interferometer with Three Light Pulses	4
1.2. Development of Precision of Absolute Gravimeters	7
1.3. Gravity Effects and Resolution of Modern Gravimeters . .	12
2.1. Interferometer Sequence Under Influence of Gravity	15
2.2. Stimulated Raman Transition	16
2.3. Interferometer Sequence With Thick Beamsplitters	22
2.4. Interferometer Transferfunctions	29
2.5. Synthetic Tides	32
3.1. Scheme of Fountain	34
3.2. MOT-Chamber	36
3.3. Cut Through MOT-Chamber	37
3.4. Magnetic Sub-Levels Resolved by Raman Pulse	38
3.5. Vacuum Pivot	39
3.6. Flux of Quantization Coil	43
3.7. Residual Flux in Magnetic Shield	45
3.8. Estimation of Wavefront Error	49
3.9. Phase Shift Due to Wavefront Curvature	50
3.10. Estimation of Error Due to Scatterer	51
3.11. Phase Shift Caused by a Diffusive Scatterer	52
3.12. Influence of Gouy Phase	53
3.13. Alignment of Raman Beams	54
3.14. Commercial Vibration Isolation	59
3.15. Hysteresis of Vibration Isolation	60
3.16. Bode Plots of Vibration Isolation	64
3.17. Vibration Spectra With and Without Active Isolation . . .	65
3.18. Physics Package	67
3.19. CAD-Drawing of the Moveable Fountain Set-up.	69
3.20. Tree Representation of Fountain Apparatus	71
3.21. Meshing of Interferometer Parts	72
3.22. Convergence of Gravity Estimation	73
3.23. Gravitation of Fountain-Apparatus in the Interferometer Zone	74

List of Figures

3.24. Most Important Sources of Gravity in the Apparatus . . .	75
3.25. Effect of Fountain Gravity on Atomic Trajectory	76
3.26. Laser Frequencies	79
3.27. Optical Systems	81
3.28. Phase Noise Spectral Densities in the Raman Phase-lock .	83
3.29. Hierarchy of the Control System	87
3.30. Fringe Spacing vs. Chirp Rate	89
4.1. Detection Signal	92
4.2. Interferometer Fringes	93
4.3. Noise in Gravity Measurement	95
4.4. Power Spectral Density of Gravimeter Noise	96
4.5. Average Accelerometer Signal During Measurements	97
4.6. First Long-Term Gravity Measurement	100
4.7. Pictures of FG5 and Atom Gravimeter	104
4.8. Sensitivity of Cold Atoms Gravimeter vs. FG5	105
5.1. Fountain During Transport	109
A.1. Pressure Correction	111
B.1. Drawing of Knife-Edge Window Seal	116
B.2. Aluminium at Elevated Temperatures	118
B.3. Elastic Counterpart in Window Seal	119
B.4. Elastic Behaviour of Window Spring	120

List of Tables

3.1. Gravity of the Apparatus 77

4.1. Gravimeter Comparison 106

A.1. Earth Rotational Parameters 111

A.2. Solid Earth Tides 112

A.3. Ocean Loading 113

Danksagung

Zu guter Letzt bleibt die angenehme Aufgabe, all jenen zu danken, die direkt oder indirekt an der Entstehung dieser Dissertation mitgewirkt haben.

Der erste Dank gebührt Achim Peters, der diese Arbeit in vielerlei Hinsicht ermöglicht und auch betreut hat. Es war zu einem guten Teil seine PhD-These, die dazu geführt hat, dass Materiewellengravimeter heute kurz davor stehen, klassische Absolutmessinstrumente zu übertreffen. Ohne seinen enormen Schatz an Erfahrungen und sein Wissen um kleinste Details wäre sie in dieser Form sicherlich nicht machbar gewesen. Außerdem möchte ich ihm an dieser Stelle herzlich dafür danken, dass er es mir ermöglichte, einige Zeit in Stanford in der Gruppe von Steven Chu zu arbeiten, einer der Geburtsstätten der Interferometrie mit kalten Atomen.

Malte Schmidt hat mit mir zusammen das Projekt begonnen und zum jetzigen Stand gebracht. Wir haben uns Photonen und Atome redlich geteilt, wobei er als Herr über Licht und Schatten die Nase nach gelieferten Stückzahlen deutlich vorne hat: während bisher grob geschätzt 10^{17} Rubidiumatome in die MOT geladen und teilweise im Interferometer verwendet wurden, mussten dazu etwa 10^{23} Photonen gestreut werden.

Unsere Nachfolger Matthias Hauth und Vladimir Schkolnik sind in den letzten zwei Jahren dazu gestoßen und haben einen gehörigen Anteil an den erzielten Leistungen. Das Projekt wäre noch nicht so weit, ohne ihre Mithilfe. Ein besonderes Dankeschön geht an Christian Freier. Seine Diplomarbeit war ein großer Gewinn, und dass er jetzt als Doktorand weitermacht, lässt auf schnelle weitere Erfolge hoffen. Allen drei gebührt Dank für Korrekturlesen und Verbesserungsvorschläge. Sebastian Grede muß auch erwähnt werden, er hat in seiner Diplomarbeit die ersten Fundamente der Kontrollsoftware gelegt.

Allen fünf danke ich für die kollegiale Zusammenarbeit und die gemeinsamen Anstrengungen. Ein gutes Team ist immer mehr als die Summe der Einzelteile.

Trista Freier war so freundlich, dem Englisch allzu deutsche Eigenheiten

auszutreiben. Falls der Leser bis zu diesen Seiten gekommen ist, ohne das Gefühl zu entwickeln, dass es hier um „sä atom interferometa“ geht, so ist das ihr Verdienst.

Die mechanische Werkstatt und besonders Herr Rausche und Herr Fahnauer hatten immer ein offenes Ohr für meine vielen – häufig ungewöhnlichen – Wünsche und mussten oft Außerordentliches leisten, um ihnen gerecht zu werden. Die exzellenten Ergebnisse sind ein wesentlicher Grund für den Erfolg dieses Gravimeters, die ohne die außergewöhnlich gute Zusammenarbeit nicht möglich gewesen wären. Außerdem hat Herr Rausche den Kontakt zur Werkstatt des DESY in Zeuthen und hier besonders zu Herrn Bandke vermittelt, die hervorragende Arbeit bei den aus dem Vollen gefrästen Vakuumkammern geleistet haben.

Die Mitarbeiter des Geophysikalischen Forschungsinstituts in Potsdam und des Bundesamts für Kartographie und Geodäsie haben sich sehr bemüht, uns die ersten Schritten in die Welt der Präzisionsgravimetrie so einfach wie möglich zu machen. Ein herzlicher Dank geht an Herrn Dr. Wziontek, Herrn Dr. Petrovic, Herrn Dr. Schäfer, Herrn Dr. Falk und Herrn Reinhold.

Ganz besonders muss und will ich meiner Partnerin Sara danken. Sie hat in den letzten beiden Jahren der Doktorarbeit und insbesondere während der Monate, in denen ich die Dissertation schrieb, mir den Rücken frei und zwei kleine Jungs im Zaum gehalten; wahrlich keine leichte Aufgabe. Wenn es eine Person gibt, ohne die es ganz und gar nicht gegangen wäre, dann ist sie es.

Für Ferdinand und Felix gibt es zum Schluss ein dickes Papa-Bussi. Ihr habt zwar nicht wirklich geholfen, aber ohne Euch hätte es viel weniger Spaß gemacht.

Selbstständigkeitserklärung

Ich erkläre, dass ich die vorliegende Arbeit selbstständig und nur unter Verwendung der angegebenen Literatur und Hilfsmittel angefertigt habe.

Berlin, den

Alexander Senger